Observations of Failure Phenomena in Periodic Media

Thesis by
Louisa Taylor Avellar

In Partial Fulfillment of the Requirements for the
Degree of
Doctor of Philosophy

CALIFORNIA INSTITUTE OF TECHNOLOGY
Pasadena, California

2018
Defended May 9, 2018

Louisa Taylor Avellar
ORCID: 0000-0003-1299-5343

ACKNOWLEDGEMENTS

First and foremost, I would like to thank my advisor, Prof. Ravichandran, for his mentorship and support. I would like to thank Prof. Bhattacharya and Prof. Faber for their guidance and insight throughout my studies. I would like to thank Prof. Daraio for serving on my committee and providing valuable feedback.

I would like to thank Jenni, Jamie, Cheryl, Donna, and Petros for all of their assistance.

I would like to thank my friends and colleagues in the Ravi-Kaushik group: Kim, Neal, Chun-Jen, Stella, Nha, Christian, Owen, Daniel, Zev, Vinamra, Lincoln, Dingyi, Paul, Jin, Tori, Ying Shi, Kevin, and many others.

I would like to thank my Caltech friends who tolerated my insatiable desire for brunch: Melissa, Camille, Victoria, Kirsti, Serena, Cecelia, Ellen, Nelson, Greg, Christophe, and Jay.

I would also like to thank everyone who helped me have a life outside of Caltech: Shelby, Meghan, Yesenia, Frida, Susie, Mike, and David.

I would like to thank all of my previous mentors who helped me become the engineer I am today: Moogega, Vania, Mircea, Yosi, Stewart, and Terry.

I would like to thank my parents for always pushing me to be my best. Without them, none of this would have been possible.

I gratefully acknowledge the support of the National Science Foundation Award No. DMS-1535083 under the Designing Materials to Revolutionize and Engineer our Future (DMREF) program. This material is based upon work supported by the National Science Foundation Graduate Research Fellowship under Grant No. DGE-1144469. Any opinions, findings, and conclusions or recommendations expressed in this material are those of the author(s) and do not necessarily reflect the views of the National Science Foundation.

ABSTRACT

New manufacturing techniques, such as 3D printing, allow for greater control over material properties and can be used to create custom heterogeneous materials. Heterogeneities can be leveraged to increase fracture toughness by redistributing the stresses, such as due to an elastic heterogeneity, or by impeding crack propagation, such as the renucleation at a material interface or edge of a void. The goal of this research is to study the mechanisms by which heterogeneities work to make composite materials more resistant to fracture than either of the individual base materials.

The influence of heterogeneities on the deformation and fracture of 3D printed fracture specimens is investigated. Brick-like heterogeneities are studied in compact tension and plate specimens with soft, stiff, and void heterogeneities. Horizontally layered heterogeneities are studied in compact tension specimens. The specimens are manufactured using a printer capable of printing multiple materials. The specimens are loaded until failure, and full-field displacement and strain data are collected using digital image correlation. The evolution of resistance to fracture is quantified by the energy release rate and fracture toughness values calculated using load, load-point displacement measurements, and crack extension data determined from images of the specimen. Both in soft specimens with stiff heterogeneities and in stiff specimens with soft heterogeneities, stresses are observed to be higher in the stiffer material. Fracture toughness is observed to increase in the presence of stiff inclusions and voids, although in the case of voids this is due to the crack terminating at the edge of the void and renucleating at the other edge.

The effects of interfaces on crack propagation in periodic media are experimentally studied. Comparative experiments on two proposed heterogeneity architectures aim to separate the effects of elastic deformation caused by heterogeneous inclusions in a composite from the effects of passing through an interface during crack propagation. The first, 'stripe' specimens, alternate equal width stripes perpendicular to the plane of the crack. The second, 'cross' specimens, have the same stripe pattern but with a narrow strip of one of the constituent materials in the plane of crack propagation. The 'cross' is wide enough to contain the crack to an area without material interfaces but thin enough that its overall effect on elastic deformation is minimal. Specimens are manufactured from two polymers using polyjet 3D printing. Energy release rate for fracture is calculated from load and displacement measurements. Digital image

correlation is used to study strain and stress fields during crack propagation. While the stress fields during crack propagation appear similar, the fracture toughness in the 'stripe' specimens was found to be higher than that of the 'cross' specimens, indicating that fracture toughness is enhanced by renucleation at the interfaces. Additionally, the amount of enhancement was observed to depend on the width of the heterogeneous layers.

The interaction between the cohesive zone and elastic stiffness heterogeneity in the peeling of an adhesive tape from a rigid substrate is examined experimentally and with finite element simulations. It is understood that elastic stiffness heterogeneities can greatly enhance the adhesion of a tape without changing the properties of the interface. However, in peeling experiments performed on pressure sensitive adhesive tapes with both an elastic stiffness heterogeneity and a substantial cohesive zone, muted adhesion enhancement was observed. It is proposed that the cohesive zone acts to smooth out the effect of the discontinuity at the edge of the elastic stiffness heterogeneities, suppressing their effect on peel force enhancement. The results of numerical simulations show that the peel force enhancement depends on the strength of the adhesive and the size of the cohesive zone.

PUBLISHED CONTENT AND CONTRIBUTIONS

[1] C.-J. Hsueh, L. Avellar, B. Bourdin, G. Ravichandran, and K. Bhattacharya. "Stress Fluctuation, Crack Renucleation and Toughening in Layered Materials". *Journal of the Mechanics and Physics of Solids* (2018). DOI: 10.1016/j.jmps.2018.04.011.
L. Avellar proposed the configuration, performed the experiments and analyzed the data.

TABLE OF CONTENTS

LIST OF ILLUSTRATIONS

LIST OF TABLES

Chapter 1

INTRODUCTION

Heterogeneities and complex architectures are pervasive in manufactured and natural materials. As a result, many studies have been completed examining how heterogeneities and complex geometries result in increased susceptibility to fracture. Complex geometries suggest corners, edges, and holes: features that lead to stress concentrations that ultimately cause material failure. Heterogeneities imply stress or strain concentrations: inclusions or voids in a material that weaken it. However, in some cases heterogeneities can contribute to toughening the material as in the case of fiber reinforced composites. Toughening mechanisms fall into two categories: intrinsic (ahead of the crack) and extrinsic (behind the crack) toughening. Intrinsic mechanisms are dominant in polymeric materials. One type of mechanism, microvoid coalescence, blunts the crack, reducing the stress concentration at its tip and possibly arresting crack growth [1]. Crack deflection toughening, an intrinsic mechanism common in polycrystalline ceramics, increases the toughness by inducing residual stresses where the crack has been deflected from propagating in a straight line (usually by propagating along grain boundaries) [2]. Polymers do not have a crystal structure, but it is possible to harness these concepts by designing micro- and macro-scale material architectures resulting in a "material by design" toughness tailored to the application of the material.

Additive manufacturing, commonly known as 3D printing, is emerging as a fabrication technique useful for manufacturing complex components, prototypes and one-off designs. The American Society for Testing and Materials (ASTM) recognizes seven types of additive manufacturing processes that encompass techniques for printing in many types of materials from polymers to metals and even ceramics [3, 4]. One of the more recent developments in additive manufacturing is the ability to print in multiple materials simultaneously. As a result, highly heterogeneous parts can be easily manufactured. Harnessing this new capability to control material architectures motivates this study of individual mechanisms and their contribution to fracture resistance.

Fracture mechanics quantifies fracture toughness using the quantities K, G, and J: the stress intensity factor, Griffith energy release rate for brittle materials, and the

J-integral, which is the generalized measure of the energy release rate for nonlinear materials, respectively. K uses crack size, orientation, and applied load to determine whether crack extension will occur. If K is greater than a critical value (a material property) the material can withstand, the crack will extend; otherwise, it does not. G and J both measure the energy required to extend a crack, although in different ways and are equivalent if linear elasticity is assumed. In linear elastic fracture mechanics, $G = J = E^* K_I^2$, where E* takes different values depending on whether plane stress or plane strain conditions are assumed [5]. The subscript I's refer to mode I, or opening mode fracture where the load is being applied normal to the crack causing it to open. Modes II and III refer to in- and out-of-plane shear fractures. In isotropic materials, cracks tend to propagate in a direction where mode I is maximized and the other modes minimized, kinking as necessary to achieve this [6].

Peeling an adhesive tape from an adherend (substrate) can be viewed as a one-dimensional crack. Early work suggested that the stiffness of the adhesive seemed to affect the work required to propagate a crack between the adhesive and adherend [7]. Further work found that varying the stiffness of the adhesive in the direction of peeling had the effect of either retarding or accelerating crack growth near interfaces between sections of different elastic moduli. It is possible to design a composite material using varying elastic moduli that is more resistant to fracture than the individual components[8, 9].

These findings relating variation in mechanical properties and fracture toughness are mirrored in experiments and theory in higher dimensions. Hossain et al. modeled cracks propagating through heterogeneous materials and found that heterogeneities can behave as toughening mechanisms by redistributing stress and inducing tortuosity [10]. In experiments performed on bio-inspired heterogeneous specimens, Dimas et al. observed that heterogeneities embedded in a matrix redistribute strains from the crack tip throughout the matrix leading to flaw tolerant behavior [11, 12]. Furthermore, in their theoretical work, Dimas et al. observed that increasing the variance of material strengths within a composite led to crack-arrest behavior and higher ultimate strengths [13].

ASTM has developed widely used standards for measuring fracture toughness and quantifying toughening behavior in homogeneous materials [14, 15]. Additionally, fracture properties of a material can be determined from studying the fracture surface post-fracture using quantitative fractography techniques [16, 17, 18]. However, the characterization of fracture properties in heterogeneous media is less well defined.

The difficulty with applying ASTM standard tests to heterogeneous media is that ASTM methods are designed to assign a single (unique) value or curve to a material's properties, whereas the properties of a heterogeneous media are variable and could vary across the material. Dimas et al. use a quantity called the toughness modulus (the area under the stress-strain curve) to quantify fracture toughness [11, 12]. However, this value is dependent upon specimen geometry and is difficult to compare between different geometries. Rice's J-integral is a popular measure of fracture toughness due to its path independence and can be calculated from full-field and/or boundary data collected during an experiment. However, one of the assumptions of the J-integral is that the material is homogeneous; when this assumption is violated it loses its path independence. As a result, J-integral methods are very accurate for homogeneous specimens but could be inaccurate for heterogeneous specimens [19, 20].

1.1 Fracture Mechanics

Griffith proposed the energy based criterion for fracture [21]:

$$G_C = 2\gamma\,, \tag{1.1}$$

where G_C is the energy required to propagate a crack by unit distance and γ is the fracture surface energy. That is, the energy required to extend a crack is equal to the amount of energy created in the formation of the new fracture surfaces. While an intuitive and elegant argument, the criterion only works for extremely brittle materials but is inadequate for many engineering materials [22]. In materials that are not perfectly brittle, many other factors contribute to the energy required to propagate a crack such as crack blunting and crack-tip plasticity. Building on the idea of defining fracture resistance as the rate of energy release, consider the definition [21]:

$$G = -\frac{\partial V}{\partial a}\,, \tag{1.2}$$

where V is potential energy per unit thickness and a is the crack length. Figure 1.1a shows a general configuration for a loaded cracked plate. To determine the energy release rate from Eq. 1.2, calculate the potential energy:

$$V = SE - W_{ext} = \frac{1}{2}Pv - Pv = -\frac{1}{2}Pv\,, \tag{1.3}$$

with SE the strain energy and W_{ext} the work done by the external force. For a prescribed load:

$$G = -\frac{\partial V}{\partial a} = -\frac{1}{2}\frac{\partial}{\partial a}(-Pv) = \frac{1}{2}P\frac{\partial v}{\partial a}\,. \tag{1.4}$$

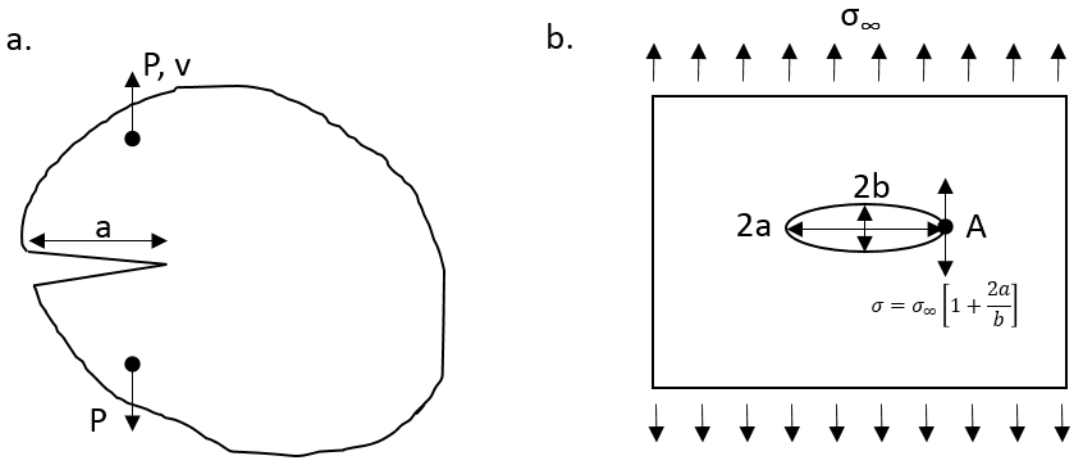

Figure 1.1: a. Edge-cracked plate with applied load P (per unit thickness), displacement v, and initial crack length a; b. Center-cracked plate with applied stress σ_∞ and initial elliptical crack with major axis, 2a and minor axis, 2b.

Define compliance as the slope of the displacement-load curve:

$$C = v/P\,. \tag{1.5}$$

Rearranging and taking the derivative with respect to crack length (for prescribed P):

$$\frac{\partial v}{\partial a} = P\frac{\partial C}{\partial a}\,. \tag{1.6}$$

Substituting this equation into Eq. (1.4) gives the energy release rate, G, in terms of compliance:

$$G_C = \frac{1}{2}P^2\frac{\partial C}{\partial a}\,. \tag{1.7}$$

The energy release rate can be determined using Eq. (1.7) if the load and the compliance can be measured.

Rice proposed calculating the energy driving the crack forward by integrating the energy flux passing through a contour around a crack tip (see Fig. 1.2) [23, 24]. Assuming the loading is quasi-static and the material is homogeneous and elastic, the 2D J-integral is given by:

$$J = \int_\Gamma (W\delta_{j1} - \sigma_{ij}\frac{\partial u_i}{\partial x_1})n_j ds\,, \tag{1.8}$$

where W is strain energy density, δ_{j1} the Kronecker delta, σ_{ij} the stress field in the solid, $\frac{\partial u_i}{\partial x_1}$ the displacement gradient, x_1 and x_2 the coordinate directions, and n_j the outward normal to the contour, Γ. This formulation is particularly useful because it is path independent; as long as it encloses the crack tip, the value will be the same.

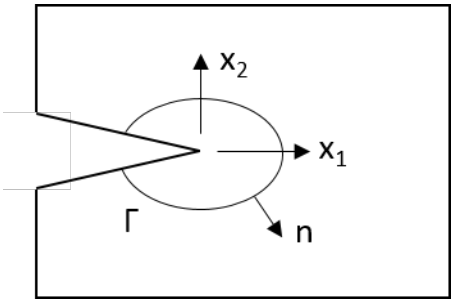

Figure 1.2: Crack with contour Γ around the crack tip with outward normal n.

Now consider the center-ellipse-cracked plate in Fig. 1.1b. Inglis found that the normal stress at the tip of the ellipse (point A) is [25]:

$$\sigma = \sigma_\infty[1 + \frac{2a}{b}]\,. \tag{1.9}$$

Holding the radius of the major axis constant, as the radius of the minor axis approaches zero, the ellipse approaches a sharp crack and the stresses at the crack tip approach infinity. Physically speaking, this is impossible. The material will yield in a region surrounding, resulting in finite stresses. This region, the plastic zone, is proportional to K^2/σ_0^2, where σ_0 is the yield stress of the material.

In 2D linear elasticity, the stress field at the tip of a crack tip in an infinite solid is:

$$\begin{aligned}
\sigma_{rr} &= \frac{K_I}{\sqrt{2\pi r}}(\frac{5}{4}\cos\frac{\theta}{2} - \frac{1}{4}\cos\frac{3\theta}{2}) + \frac{K_{II}}{\sqrt{2\pi r}}(-\frac{5}{4}\sin\frac{\theta}{2} + \frac{3}{4}\sin\frac{3\theta}{2}) \\
\sigma_{\theta\theta} &= \frac{K_I}{\sqrt{2\pi r}}(\frac{3}{4}\cos\frac{\theta}{2} + \frac{1}{4}\cos\frac{3\theta}{2}) - \frac{K_{II}}{\sqrt{2\pi r}}(\frac{3}{4}\sin\frac{\theta}{2} + \frac{3}{4}\sin\frac{3\theta}{2}) \\
\sigma_{r\theta} &= \frac{K_I}{\sqrt{2\pi r}}(\frac{1}{4}\sin\frac{\theta}{2} - \frac{1}{4}\sin\frac{3\theta}{2}) + \frac{K_{II}}{\sqrt{2\pi r}}(\frac{1}{4}\cos\frac{\theta}{2} + \frac{3}{4}\cos\frac{3\theta}{2})\,.
\end{aligned} \tag{1.10}$$

Equivalently in Cartesian coordinates:

$$\begin{aligned}
\sigma_{11} &= \frac{K_I}{\sqrt{2\pi r}}\cos\frac{\theta}{2}(1 - \sin\frac{\theta}{2}\sin\frac{3\theta}{2}) - \frac{K_{II}}{\sqrt{2\pi r}}\sin\frac{\theta}{2}(2 + \cos\frac{\theta}{2}\cos\frac{3\theta}{2}) \\
\sigma_{22} &= \frac{K_I}{\sqrt{2\pi r}}\cos\frac{\theta}{2}(1 + \sin\frac{\theta}{2}\sin\frac{3\theta}{2}) + \frac{K_{II}}{\sqrt{2\pi r}}\cos\frac{\theta}{2}\sin\frac{\theta}{2}\cos\frac{3\theta}{2} \\
\sigma_{12} &= \frac{K_I}{\sqrt{2\pi r}}\cos\frac{\theta}{2}\sin\frac{\theta}{2}\cos\frac{3\theta}{2} + \frac{K_{II}}{\sqrt{2\pi r}}\cos\frac{\theta}{2}(1 - \sin\frac{\theta}{2}\sin\frac{3\theta}{2})\,.
\end{aligned} \tag{1.11}$$

Williams obtains this result by considering the V-notch system loaded in tension shown in the inset of Fig. 1.3 [24, 26, 27, 28]. Williams uses the following ansatz:

$$\phi(r,\theta) = r^{\lambda+2} f(\theta), \tag{1.12}$$

in the Airy stress biharmonic equilibrium equation (body forces are assumed to be zero):

$$\nabla^4 \phi = 0. \tag{1.13}$$

The V-notch is not loaded on the notch surfaces, leading to traction boundary conditions:

$$\sigma_{\theta\theta}(r, \theta = \pi \pm \omega/s) = \sigma_{r\theta}(r, \theta = \pi \pm \omega/s) = 0, \quad 0 < r < +\infty. \tag{1.14}$$

The general solution for symmetric loading is the resulting ordinary differential

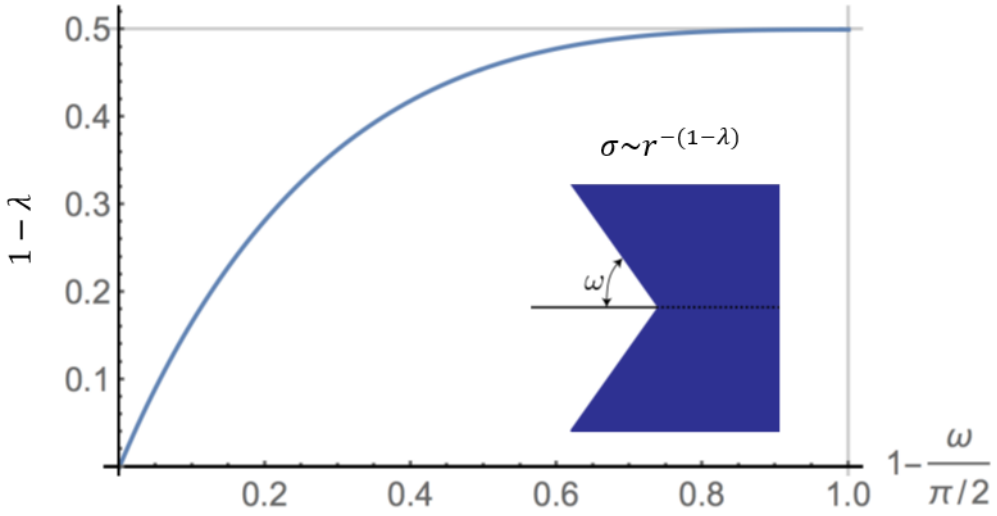

Figure 1.3: Strength of the singularity $(1 - \lambda)$ versus angle of the notch [29].

equation:

$$\phi(r, \theta) = r^{\lambda+2} A \cos \lambda\theta + B \cos(\lambda + 2)\theta. \tag{1.15}$$

Using the traction-free boundary conditions results in the equations:

$$\begin{aligned} A \cos(\lambda(\pi - \omega/2)) + B \cos((\lambda + 2)(\pi - \omega/2)) = 0, \\ A\lambda \sin(\lambda(\pi - \omega/2)) + B(\lambda + 2) \cos((\lambda + 2)(\pi - \omega/2)) = 0. \end{aligned} \tag{1.16}$$

The determinant of this system must equal zero for non-trivial solutions:

$$\sin(2\lambda(\pi - \omega)) + \lambda \sin(2(\pi - \omega)) = 0\,. \tag{1.17}$$

The plot in Fig. 1.3 shows the value of singularity versus the half-angle notch, ω. The singularity disappears for $\omega = \pi/2$, or no notch. The most singular solution with bounded energy occurs at $\lambda = -\frac{1}{2}$ for a crack-like notch, $\omega = 0$. This leads to the well known results in Eq. (1.11). Tanné et al. used this geometry to study crack

nucleation in variational phase-field simulations of brittle fracture, concluding that this type of model could accurately be used to predict crack nucleation [30].

Stress intensity factors are defined to be:

$$K_I = \lim_{r\to 0} \sqrt{2\pi r}\sigma_{22}|_{\theta=0}; \quad K_{II} = \lim_{r\to 0} \sqrt{2\pi r}\sigma_{12}|_{\theta=0}\,. \tag{1.18}$$

Stress intensity factors can be calculated for various geometries. If linear elasticity is assumed, the stress intensity factors of simple loadings can be added and subtracted to find the solution to a more complicated loading scenario by the principle of superposition [24].

Dugdale applied the principle of superposition to the problem shown in Fig. 1.4 to determine the size of the plastic zone in thin steel sheets [31, 32]. The problem is modeled as a slit, $2a$, in an infinite plate loaded in tension, σ_∞. The stress in zones of length s at the slit tips is limited to the yield strength of the material, σ_0. This problem is modeled as three simple problems: (1) a slit in an infinite plate loaded in tension, σ_∞, (2) a slit in an infinite plate with the entire slit loaded in compression, σ_0, and (3) the portion of the slit from $-a$ to a loaded in tension, σ_0. The solution to the original problem is found by superposition of the three simpler problems:

$$K_I = K_I^{(1)} + K_I^{(2)} + K_I^{(3)}\,. \tag{1.19}$$

In order to find the size of the yield zone, it is desired to solve the problem such that the stress is always finite (there is no stress singularity), $K_I = 0$. The solution is [22, 31, 32]:

$$s = a \sec \frac{\sigma_\infty \pi}{2\sigma_0} - a\,. \tag{1.20}$$

It is important to note that the material is not failed in the sense of fracture in the region s ahead of the crack tip; that is, there is still material in this region but the maximum stress it can hold is given by the yield strength of the material. Figure 1.5 shows the stresses ahead of the crack tip. If there were no yielded material, the stresses would approach infinity near the crack tip (the dotted line); however, because the material has yielded ahead of the crack tip, the stresses are finite in the region s (the solid line). This figure is misleading, however, as the length of the yielded zone is not merely the distance at which the stress field ahead of the crack tip equals the yield strength of the material. The yielded zone is larger because the load cutoff by limiting the stress to the yield strength of the material must be accounted for (the area between the solid horizontal line, σ_0, and the dashed line). Finally, note

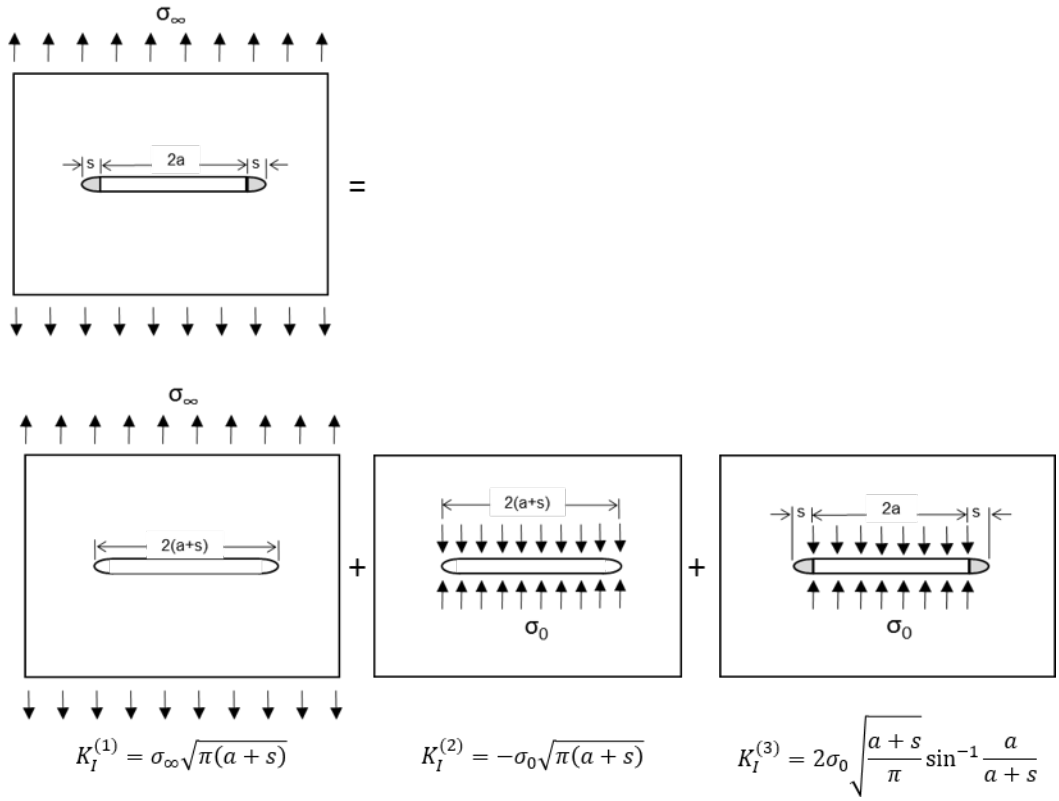

Figure 1.4: Dugdale problem for determining the size of the plastic zone.

the definition of the COD, or, the crack opening displacement in Fig. 1.5. Because the crack surfaces separate before failure, it is useful to define the separation of the fracture surfaces at the crack tip, a, as the COD [22, 32].

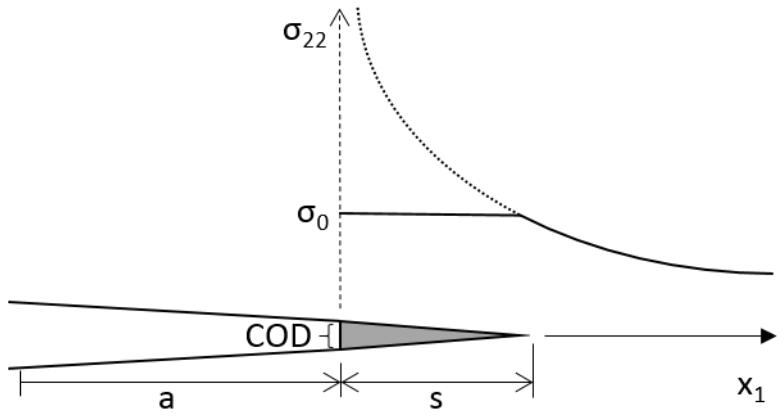

Figure 1.5: Stresses in the yielded zone.

Building on this formulation, Barenblatt generalized the problem to include stresses that are a function of the opening displacement in s, renaming s a 'cohesive zone'

[32, 33]. Figure 1.6 shows some common cohesive laws, also called traction-separation laws, of stress as a function of separation, δ, in the cohesive zone. The stress equals zero at δ_C, the critical COD. The area under the curve is defined to be the critical energy release rate of the material:

$$G_C = \int_0^{\delta_C} \sigma(\delta) d\delta. \tag{1.21}$$

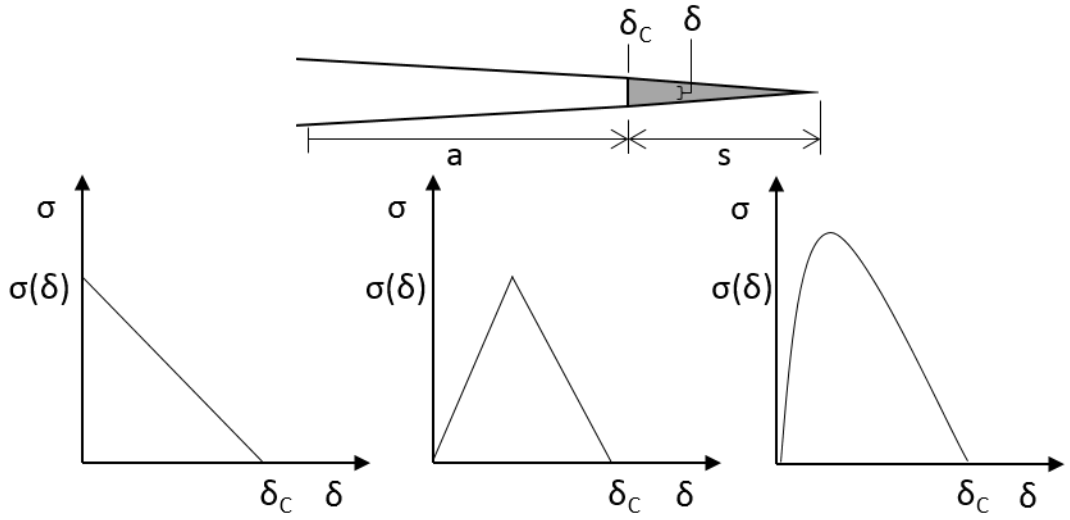

Figure 1.6: Commonly used cohesive (traction-separation) laws.

1.2 Heterogeneous Fracture Mechanics

High stiffness materials, such as ceramics and glass, are rarely used as structural materials. The reason for this is that, although the materials deform little when subjected to high loads, they are very brittle leaving them susceptible to failure originating from cracks and other small defects. As a result, increasing the resistance to fracture has been studied extensively in ceramics. One of the topics that has received a great deal of attention is toughening due to crack penetration in and deflection around second-phase particles [2, 34]. Crack penetration and deflection at bi-material interfaces has been studied more generally, such as in the works by He and Hutchinson and Cotterell and Rice [22, 35]. Building on the analysis presented in section 1.1, Zak and Williams showed that in the case of a bi-material interface, varies with the contrast of material properties [36]. Figure 1.7 shows the variation of the strength of the singularity versus the elastic contrast of the two materials. If $E_1 << E_2$, as in the case of the crack propagating from a soft to a stiff material, the power of r tends towards zero. This means the singularity vanishes so the crack

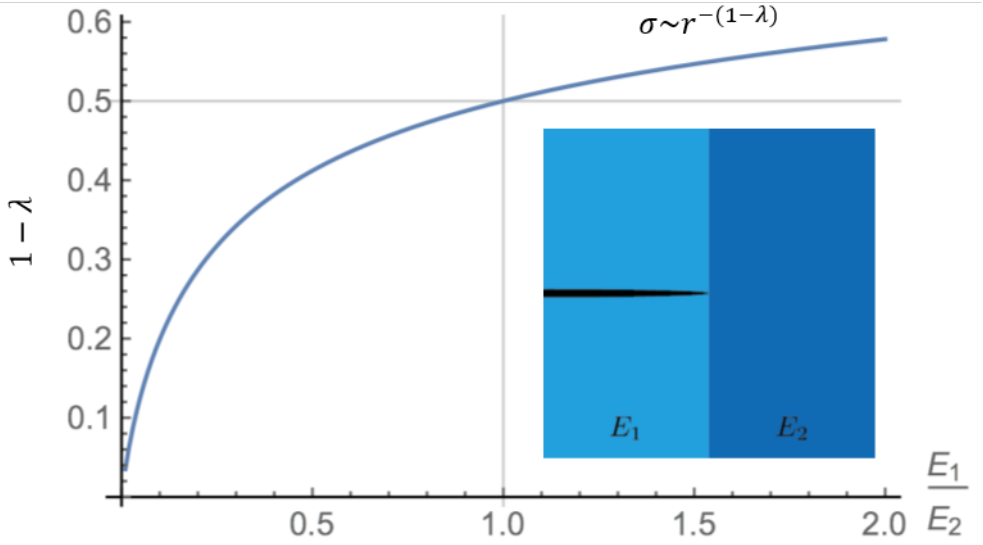

Figure 1.7: Strength of singularity vs material contrast as crack approaches the interface [29].

must renucleate to pass through the interface. Instead if $E_1 >> E_2$, as in the case of a crack propagating from a stiff to a soft material, the power of r increases, amplifying the strength of the singularity and driving the crack forward. In this case, the crack is likely to jump across the interface.

Hossain et al. performed variational phase-field simulations studying the crack propagation through heterogeneous media and showed that the elastic contrast can have significant influence on the fracture toughness. Additionally, they showed that fracture toughness could be asymmetric by implementing asymmetric material architectures [10]. Taking advantage of developments in additive manufacturing that allow for parts to be printed with variable material properties, Weng and Xia performed fracture experiments on heterogeneous materials, and found toughness enhancement in agreement with numerical simulations performed on the same [37].

1.3 Tape Peeling

Tape peeling can be considered a simplified one-dimensional fracture problem. Consider the problem in Fig. 1.8a. The peel front of the tape moves forward by creating new surfaces, analogous to Griffith fracture. Following Griffith's energy balance approach, Kendall related the adhesion energy to the measured peel force and angle, θ [21, 38]. The total amount of energy in the system is equal to the elastic energy stored due to deformation of the tape plus the potential energy due to the movement of the applied load plus the energy required to move the peel front from

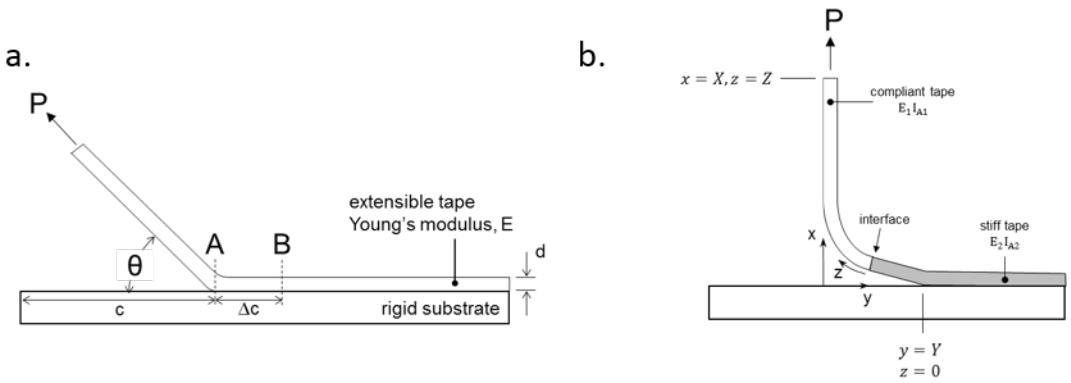

Figure 1.8: a. Schematic of a homogeneous tape peeling experiment; b. Schematic of a discontinuous tape peeling experiment. Tape has width, b.

point A to point B by forming new surfaces:

$$U_{tot} = U_{el} + U_p + U_s \,. \tag{1.22}$$

The elastic energy is equal to the area under the load-displacement curve:

$$U_{el} = \frac{1}{2} P\delta \,. \tag{1.23}$$

The stress in the tape due to the applied force, P is:

$$\sigma_t = \frac{P}{bd}\,, \tag{1.24}$$

where b is the width of the tape and d is the tape thickness. The displacement of the peeled tape in the region A-B is:

$$\delta = \epsilon\Delta c = (\frac{\sigma}{E})\Delta c = \frac{P}{Ebd}\Delta c \,. \tag{1.25}$$

Putting this into the equation for elastic energy gives:

$$U_{el} = \frac{P^2\Delta c}{2Ebd} \,. \tag{1.26}$$

The work due to peeling the tape is equal to the peel force times the distance it moves. If the elastic strains in the tape are small, this can be accurately approximated as inextensible and this distance is $\delta_C(1 - cos\theta)$:

$$U_p = P(1 - \cos\theta)\Delta c \,. \tag{1.27}$$

The energy associated with the creation of the new surfaces is:

$$U_s = -bG\Delta c\,, \tag{1.28}$$

where G is the adhesive energy. Using energy conservation to solve for G:

$$\frac{dU_{tot}}{d\Delta c} = 0 = \frac{P^2}{2Edb^2} + \frac{P}{b}(1 - \cos\theta) - G = 0\,. \tag{1.29}$$

Rearranging gives the equation for adhesion energy:

$$G = \frac{P^2}{2Edb^2} + \frac{P}{b}(1 - \cos\theta)\,. \tag{1.30}$$

The inextensible case,

$$\frac{P}{b} = \frac{G}{1 - \cos\theta}\,, \tag{1.31}$$

was given by Rivlin [7]. Because adhesion strength is generally very low, the stresses in the tape are usually negligible and the elastic term can generally be ignored [38].

Kendall modified the analysis for a two segment film to study the effects of discontinuous material properties across an interface, such as in Fig. 1.8b [8]. The energies are now described by the integrals:

$$\begin{aligned} U_s &= Gb\int_0^Z dz \\ U_{el} &= \frac{1}{2}P^2\int_0^Z \frac{y^2}{E_nI_n}dz \\ U_p &= -P\int_0^X dx\,. \end{aligned} \tag{1.32}$$

The integrals are evaluated using the beam equation:

$$\frac{d^2y/dx^2}{1 + (dy/dx)^{2\frac{3}{2}}} = \frac{Py}{E_nI_n}\,. \tag{1.33}$$

Solving for equilibrium as in Eq. (1.29), the maximum toughening enhancement is achieved when the peel front is at the interface and the force is [8]:

$$\frac{P}{b} = \frac{E_2I_2}{E_1I_1}G\,. \tag{1.34}$$

Xia et al. derived a relation for the toughening enhancement in periodic heterogeneous tapes [39]. Xia defines the length scale of the tape subject to bending under an applied load, $\lambda = \sqrt{D_E/G}$, where D_E is a representative bending rigidity based on the length fraction of the individual rigidities (EI) in the periodic tape. For periods much greater than λ, Kendall's equation is recovered. For periods on the same order as λ, the toughening enhancement is suppressed.

From Eq. (1.34) it can be observed that toughening can be induced either by varying the moment of inertia ($\frac{I_2}{I_1}$) or by alternately stiffening the tape ($\frac{E_2}{E_1}$). Kendall varied the moment of inertia by alternately thickening the tape ($I = \frac{bd^3}{12}$, where b is the width and d the thickness of the tape). In experiments on the thickened tape, Kendall showed that the radius of curvature as the peel front approaches and passes through the interface varies dramatically. This shape change is responsible for the increase of energy required to propagate the crack further. Kendall's experiments on both thickened and stiffened tape show that the velocity of the crack propagation slows near the interface to the higher bending rigidity and increases near the interface to the lower bending rigidity. Outside of areas near the interface, the velocity is a constant value despite the local stiffness or thickness. Xia et al.'s experiments on tape with variable thickness were in good agreement with theory; under the appropriate conditions, the peel force enhancement was proportional to the cube of the thickness.

1.4 Outline

This thesis examines fracture toughening mechanisms due to heterogeneities through experiments, simulations and analysis with the goal of developing a better understanding of how individual mechanisms contribute to toughening. Chapter 2 presents experiments exploring the effect of heterogeneities on crack propagation. Several material architectures, including a stiff matrix with soft inclusions and a soft matrix with stiff inclusions, are investigated. Generally, stresses are observed to be higher in the stiffer material. Fracture toughness is observed to increase in the presence of stiff inclusions and voids, although in the case of voids this is due to the crack terminating at the edge of the void and renucleating at the other edge.

Chapter 3 presents experiments, simulations, and theory studying the contribution of renucleation at material interfaces to overall toughening. A theoretical framework to predict the relative enhancements in toughening is presented. A comparative experiment of two material architectures is proposed to separate the effect of renucleation from the toughening enhancement due to elastic contrast. The results of the experiments show good agreement with the theory and variational phase-field simulations of the material architectures. The effect of renucleation was observed to be more substantial than that of the elastic contrast alone. Additionally, the amount of enhancement was observed to depend on the width of the heterogeneous layers.

Chapter 4 presents experiments and simulations studying the interactions of the

elastic stiffness heterogeneity with the resulting cohesive zone. Observations from the experimental peel test indicate that the cohesive zone suppresses the effect of the stiffness heterogeneity. The results of numerical simulations show that the peel force enhancement depends on the adhesive energy and the size of the cohesive zone.

Chapter 5 summarizes the thesis and provides recommendations for further studies.

Chapter 2

TOUGHENING MECHANISMS IN PERIODIC LAYERED MEDIA

Heterogeneities change how a material deforms resulting in stress fields that can be leveraged to increase fracture toughness. Until recently, experiments studying cracks in heterogeneous materials have generally been limited to laminate materials due to the difficulty of manufacturing heterogeneous solids. New manufacturing techniques, such as 3D printing, allow for control over material properties and can be used to create custom heterogeneous materials. The last decade has seen the emergence of commercial 3D printers capable of fabricating engineered heterogeneous materials. The Stratasys Connex3 Objet series printer is a particularly common commercially available printer that can print heterogeneous materials. Such printers have been used widely in research in the study of base-line material behavior of homogeneous additive manufactured materials, such as anisotropy due to the printing process and the effect of aging [40, 41]. Because of the ability to print in materials with contrasting mechanical properties, 3D printers have also been used to study material architectures. Dimas et al. performed systematic studies of material architectures based on those found in nature to explore the effect of material contrasts on mechanical properties such as fracture toughness [11]. Gu et al. examined nacre-inspired material architectures to study the role of hierarchical microstructures in material strength [42, 43]. Additionally, Gu et al. and Dimas et al. used the results of such studies to determine parameters that can be varied in architectures in order to tune material properties [11, 12, 43]. Gu et al. performed studies attempting to optimize the fracture toughness of a geometry under a specific load [44, 45, 46].

Simple architectures of layered materials have been used to examine the effect of elastic contrasts on fracture toughness enhancement in heterogeneous materials. Hossain et al. modeled crack propagation through layered materials and found that fracture toughness varies with proximity to interfaces [10]. Additionally, they found that the elastic contrasts could be used to introduce stress fields which caused the crack to meander rather than propagate straight ahead, which also increased fracture toughness. Wang and Xia studied crack propagation through heterogeneous layered materials using models and experiments on specimens printed on a 3D printer [37].

This chapter begins with experiments to determine the homogeneous material properties of 3D printed materials. Studies on the effect of simple material architectures on fracture toughness follow. Printed specimens with various material architectures are evaluated to determine their fracture toughness with digital image correlation, which is used to visualize and quantify the strain fields around the crack tip in the specimens.

2.1 Component Homogeneous Material Properties

The base resins used in the following sections are Stratasys' VeroWhitePlus (Vero) and TangoBlackPlus (Tango) using the Connex3 Objet500 PolyJet printer[1]. Due to the large print bed, all of the specimens for a test can be printed at one time. Vero is a proprietary acrylic photopolymer resin that cures into a rigid material. Tango is a proprietary urethane photopolymer resin that cures into a compliant material. The two resins can be mixed in different discrete proprietary ratios during the printing to achieve a range of material properties between those of Vero and Tango. DM8530 is the third mixture more compliant than Vero. DM8530 is the most compliant mixture available that fractures without tearing. Vero and DM8530 are selected to be studied because they maximize the elastic contrast available to be printed while still failing without large plastic deformations. The printer works by spraying the base resins out of a print head and passing a UV light over the deposited resins to cure them. By repeating this process many times, the parts are built up on the print bed. After printing, the specimens are removed from the print bed and cleaned. Specimens are stored in sealed bags to limit exposure to air until they are tested; specimens are tested five days after printing[2].

Tensile testing is performed to determine the Young's modulus and Poisson's ratio of the Polyjet materials VeroBlackPlus (the same as Vero except a different color) and DM8530. The tests are performed following the ASTM standard D638 [50], using type I dog bone specimens at the nominal strain rate 0.1 mm/mm-min. The experiment is performed on an MTS Servohydraulic load frame (Model No. 358.10,

[1] Printer Specifications[47]:
Maximum Build Size (XYZ): 490 x 300 x 200 mm
Resolution: X- and Y-axis: 600 dpi; Z-axis 1600 dpi
Minimum Layer Thickness: 16 microns
Accuracy (XY): 20-85 microns for features below 50 mm; 200 microns for full model size
Support Material: Soluble support material

[2] The specimens are damp immediately after printing due to the cleaning process. The specimens are allowed to dry for five days to mitigate the effects of absorbed water on the mechanical properties of the material. The specimens are stored in sealed bags to limit exposure to air as oxidation is a possible source of degradation of acrylates [48, 49]

max load: 14.7 kN). The full-field strain is measured using Digital Image Correlation (DIC) from a series of images taken during the loading [51]. As opposed to a displacement gage or a strain gage which is either bonded to the surface of a specimen or otherwise mechanically attached to it and provides only one measurement, DIC is a contact-free optical method that provides full-field displacements and strains. Specimens are prepared for DIC analysis by painting a random speckle pattern on the surface to be studied. Images of the prepared surface are captured during the experiment and then post-processed using DIC software. The software splits the images into smaller subsets of adjacent pixels and tracks the subsets, from which displacement and strain information can be determined. Open source Matlab-based DIC algorithms developed by Jones [52] and Blaber [53] are used in this work. In-plane strains in the specimen (ϵ_{xx}, ϵ_{yy}, and ϵ_{xy}) are determined by processing images of the gage length of the specimen taken during loading. Nominal stress is determined from the load readings from the load frame and plotted against ϵ_{yy}, the initial slope of which is used to determine the Young's modulus, E. Poisson's ratio, ν, is determined by averaging the x- and y-strains in each image and calculating, $\nu = -\epsilon_{xx}/\epsilon_{yy}$ for each image which are then averaged to calculate the Poisson's ratio for the material.

For the tensile tests, the images are acquired using a CCD camera (UNIQ UP-2000CL, Uniqvision, Santa Clara, CA) connected to a frame grabber (NI PCIe-1430, National Instruments, Austin, TX) with image acquisition started at the same time as the loading begins. Plots of stress versus strain for VeroBlackPlus are shown in Fig. 2.1 (although three of the specimens were tested to failure, the strain data does not cover that period of the test, so failure is not shown). Vero and DM8530 specimens from a different print were tested separately using the same process. The mechanical properties of all tested specimens are shown in Table 2.1.

Using all of the specimens, the Young's modulus and Poisson's ratio for the Vero material is determined to be 1960±120 MPa and 0.399±0.012, respectively. The peak tensile stress occurs at yield and is 48.3 MPa. The Young's modulus and Poisson's ratio for DM8530 (one specimen) are 1020 MPa and 0.414, respectively. The modulus of Vero is higher than that of DM8530. Henceforth, Vero will be referred to as the stiff material and DM8530 will be referred to as the compliant material. For both materials, the Young's modulus is on the lower end of the values published by 3D printing service providers: 2000-3000 MPa and 1100-1700 MPa, respectively [54, 55]. Part of this discrepancy may be due to the portion of the

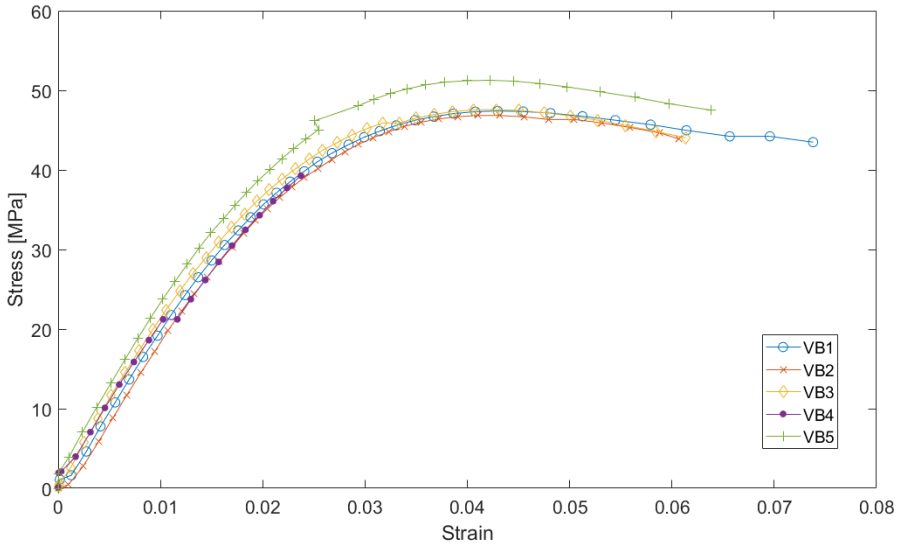

Figure 2.1: Stress versus strain plots of ASTM D638 dogbone tests of VeroBlack-Plus. Only the initial portion specimen #VB4 was captured and shown.

	Poisson's ratio ν	Young's modulus E [MPa] 1.50 %	Young's modulus E [MPa] 2.50 %	Peak tensile stress σ_{peak} [MPa]
Vero				
VB1	0.399	1970	1730	47.4
VB2	0.387	1900	1720	46.8
VB3	0.409	2080	1760	47.6
VB4	0.383	1780	1630	48.5
VB5	0.409	2100	1820	51.3
VW1	0.411	1910	-	-
DM8530				
DM1	0.414	1020	-	-

Table 2.1: Mechanical properties of Vero and DM8530. Percent indicates range of percent strain used for calculation of the Young's modulus, E.

plot used to calculate these values; the stress strain plots for the VeroBlackPlus tests in Fig. 2.1 show that the material has a fairly small linear region. The values of Young's modulus calculated for different upper limits of strain for VB1-5 shown in Table 2.1 demonstrate that the Young's modulus value increases dramatically as the upper limit is decreased. The Young's modulus using the linear region is the value that is used in the following work (Table 2.2).

Using the experimental setup, tensile tests were also performed on Vero specimens

	Poisson's ratio, ν	Young's modulus, E [MPa]
Vero	0.399	1960
DM8530	0.414	1020

Table 2.2: Mechanical properties of Vero and DM8530.

with the layers oriented in the direction of the tensile loading (along the z-axis of the printer). Additionally, these specimens were aged 12 months. The results of tensile tests are shown in Fig. 2.2 and Table 2.3. The Young's modulus and Poisson's ratio are 1710±90 MPa and 0.358±0.008, respectively. The ultimate strength is 26.5 MPa. Both the Young's modulus and the ultimate strength are found to have lower values when compared to the results presented earlier. Specimen elongation at failure is dramatically reduced. It is not clear how much aging and layer orientation individually contribute to the reduction in material properties. In comparison, for specimens aged ten weeks, Bass et al. found that the elongation at failure was greatly reduced but the Young's modulus changed only a little and the ultimate strength increased. In un-aged specimens, they found very little variability in material properties for specimens oriented in the xy-plane of the print bed [40].

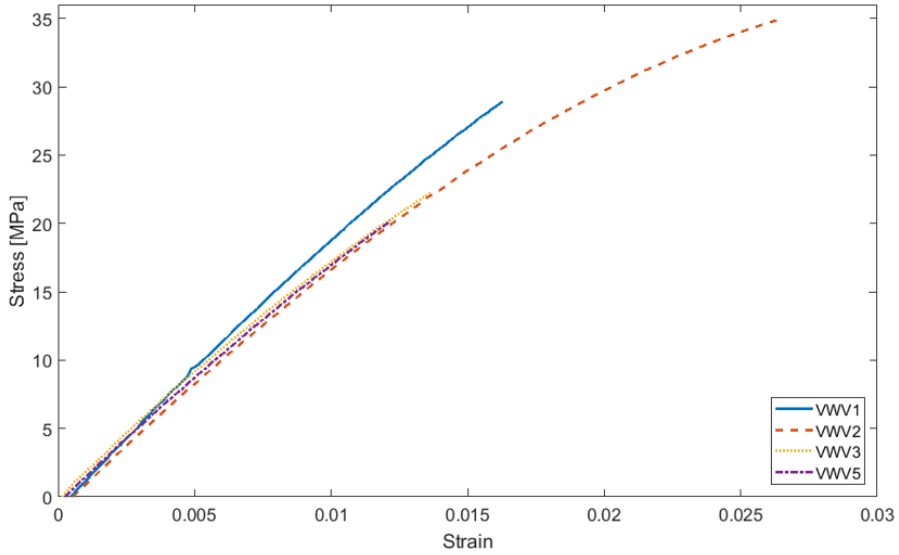

Figure 2.2: Stress versus strain plot of ASTM D638 dogbone test of vertically printed and aged Vero.

	Poisson's ratio, ν	Young's modulus, E [MPa]	Failure stress, σ_{fail} [MPa]
VWV1	0.358	1840	28.9
VWV2	0.363	1660	35.0
VWV3	0.347	1640	22.2
VWV5	0.364	1690	20.2
AVG	0.358	1710	26.5

Table 2.3: Mechanical properties of vertically printed and aged Vero. Loading occurs in a direction normal to the print interface.

2.2 Heterogeneous Bricks

Initial experiments are performed to study the influence of a stiff heterogeneity on crack propagation through a compliant matrix. This experiment is based on methods for determining fracture toughness and the fracture resistance curve of homogeneous polymers detailed in ASTM D5045 and ASTM D6068 [14, 15]. The goal of the experiments is to characterize the evolution of resistance to stable crack growth initiated from a preexisting sharp crack using load, displacement, and crack extension measurements. The energy release rate G is calculated using the double cantilever beam analysis found in Hutchinson [56].

Specimen Selection

Design studies are performed in order to create a specimen in which the heterogeneities affect the stress distribution in the matrix ahead of the crack. The specimens are manufactured using a Stratasys Connex3 Objet500 3D printer. Stratasys proprietary materials DM9895 (E=45 MPa [57]) and Vero (E=1960 MPa, ν=0.399) are selected as the respective compliant matrix and stiff heterogeneity materials. These materials are selected due to their compliance mismatch: DM9895 is the next more compliant polymer than DM8530 while Vero is the stiffest polymer the Stratasys Connex3 Objet500 can print. A simple brick-like pattern is used as the base configuration. Figure 2.3 shows an example of such a pattern. The width of the matrix between heterogeneities (Fig. 2.3a), the width of the heterogeneities (Fig. 2.3b), and the height of matrix in between the heterogeneities (Fig. 2.3c) are varied and stresses in the specimen are simulated in Solidworks using prescribed displacement boundary conditions. Because cracks tend to propagate in the direction of highest tensile stresses, contour plots of circumferential (hoop) stresses for different variations are compared qualitatively. The variation whose contour plot demonstrates the largest tensile hoop stress is selected as the configuration for the 3D printed specimens. Figure 2.4 shows hoop stresses in the selected configuration

as the crack extends through the specimen. Overall specimen dimensions are 50.8 mm x 45.7 mm x 9.5 mm.

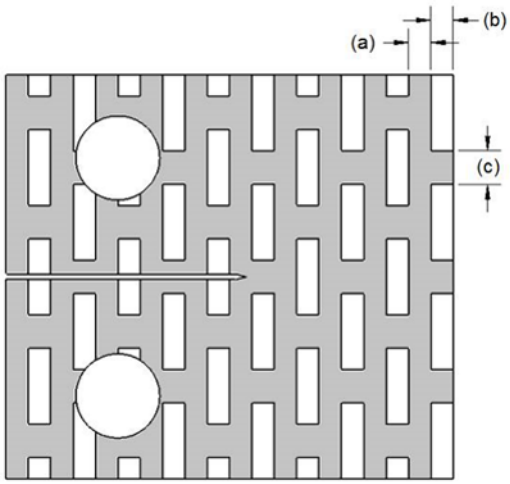

Figure 2.3: Front view of fracture specimen with brick architecture. Design studies vary lengths (a), (b), and (c). Matrix (grey) printed in DM9895; inclusions (white) printed in Vero.

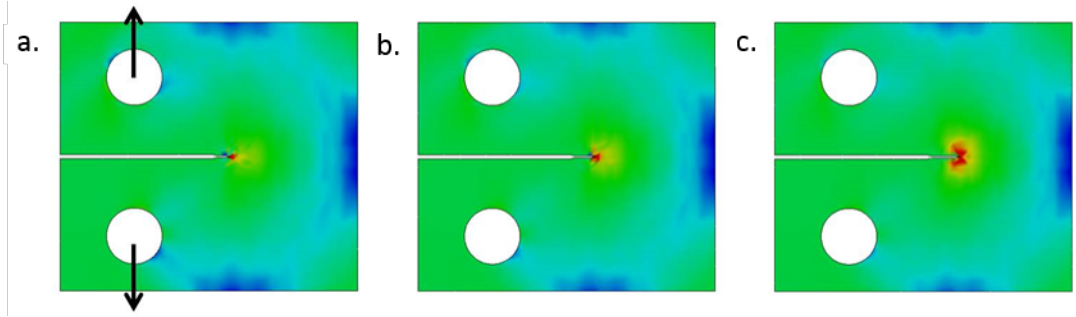

Figure 2.4: Design study showing magnitude of hoop stress ($\sigma_{\Theta\Theta}$) for a propagating crack in the selected configuration. Red denotes large positive (tensile) stress and blue denotes large negative stress. a. Δa=1.9 mm, arrows denote location of simulated application of prescribed displacement loading; b. Δa=3.2 mm; and c. Δa=4.4 mm.

Experimental

Initial notches of width 0.6 mm with a 30° tip are modeled and printed into the specimens. A fresh razor blade is pressed into the tip of the notch to a depth of 1.3 mm to ensure an initial sharp crack. The specimens are pulled to failure in a load frame at a loading rate of 2.54 mm per minute. A camera pointed at a face of the specimen speckled for DIC analysis begins to acquire images at the same time as the loading. To ensure good contrast for DIC everywhere on the face of the

specimen, the face is first spray painted white before being spray painted with black speckles. The camera captures, timestamps, and saves images of the experiment at a rate of approximately seven images per second for the entire duration of the test. DIC is used to compute the full field strains in deformed specimens [51, 52]. Load and displacement data is collected by the load frame, while crack extension data is measured from the collected images post-test. It is assumed that the crack front is straight through the material; that is, that the crack front visible on the surface is the length as the crack front through the interior of the specimen.

Results

Figure 2.5 shows a fracture resistance curve for the heterogeneous specimen. The curve is calculated using the equation for the energy release rate:

$$G = \frac{12P^2a^2}{Eb^3}, \tag{2.1}$$

where P is the measured load (per unit thickness), a the crack length, and b the flank height [56].

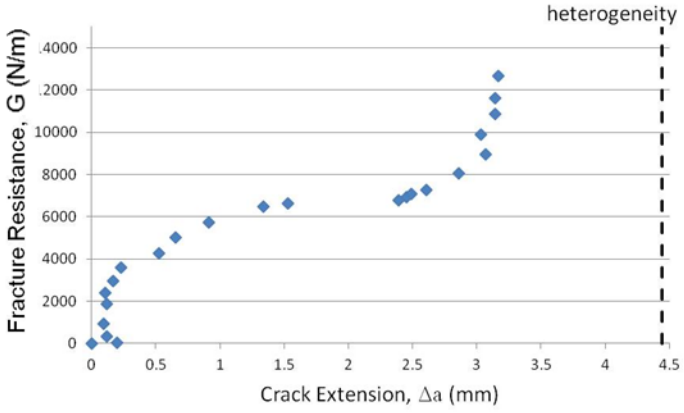

Figure 2.5: Fracture resistance curve from load test data.

Young's modulus, E, is estimated using finite element simulations of the heterogeneous material. The fracture resistance curve indicates an increase in toughness as the crack approaches the heterogeneity.

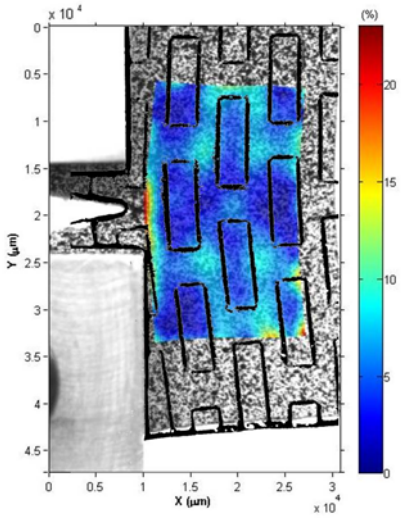

Figure 2.6: Equivalent strain obtained from the DIC measurement overlaid with outline of deformed specimen.

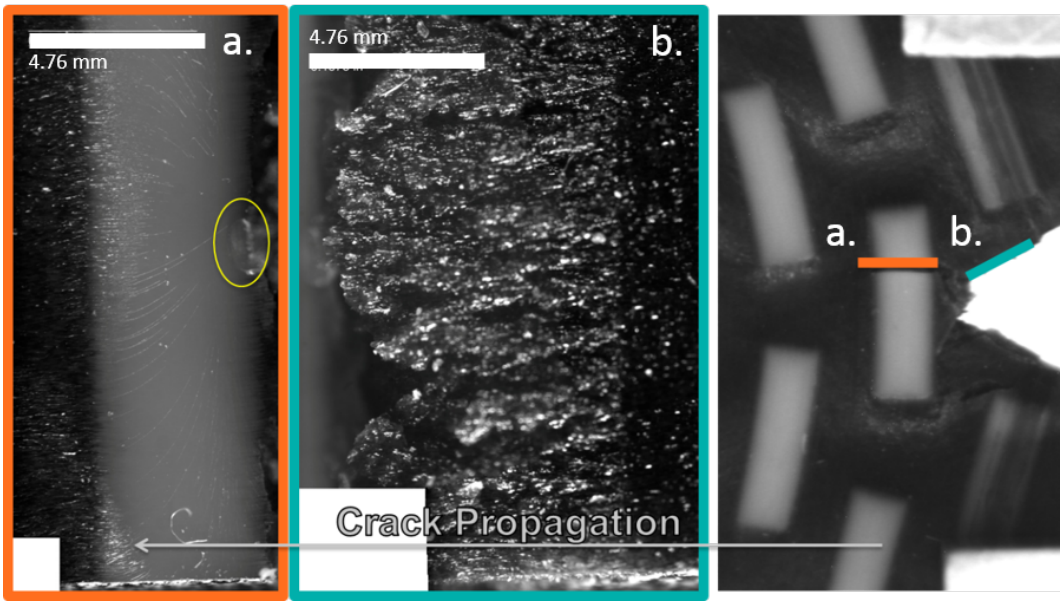

Figure 2.7: Optical images of the fracture surface.

Figure 2.6 shows equivalent strain determined from DIC overlaid with the outline of the deformed specimen. The strain is redistributed mainly into the compliant matrix and the stiff inclusions carry very little strain. This result is consistent with experiments carried out by Dimas [12, 13] studying the effects of decreasing stiffness ratio versus flaw tolerant behavior in bio-inspired composites. The matrix in between the inclusions ahead of the crack appears to carry considerably less strain

than the rest of the matrix. It is possible that the heterogeneities are shielding this area or could be a result of edge effects.

Discussion

Results from this experiment indicated that the stiff inclusions in the specimens studied increase the fracture resistance as the crack tip approaches the inclusion. However, it is difficult to draw definitive conclusions from this experiment because of the limitations of the experiment. For instance, the matrix material was very compliant, resulting in extreme deformations in the specimen. The deformations resulted in >20% strains which are too large to be measured precisely using DIC. Additionally, large out of plane deformations were observed at these strains; in addition to negating the plane strain assumption, these deformations also reduce the accuracy of DIC. Furthermore, the specimens were small relative to size of the heterogeneities so edge effects could have influenced the outcome significantly. Finally, this experiment assumed that the crack does not renucleate at the interfaces between the heterogeneities and that the observed increase in fracture toughness is not solely a result of arresting and renucleating the crack. Fractographic evidence does not support this assumption. Figure 2.7 shows microscopic images taken of the fracture surfaces. Circled in yellow in Fig. 2.7a appears to be a flaw indicating a point of origin for the fracture through the heterogeneity. The existence of a flaw indicates that the crack renucleated in the heterogeneity at that point. It is not clear how much the renucleation event contributed to the overall increase in fracture toughness.

2.3 Heterogeneous Plates

Subsequent experiments are performed to build upon results from the initial experiments while improving experimental design and data collection methods. Significantly stiffer materials are selected to prevent excessive deformations and specimens are much larger to reduce edge effects. The change in specimen geometry prompts a change in analysis methods; the energy release rate G is calculated using the infinite strip (Fig. 2.8a) analysis found in Hutchinson [56].

Experimental

The brick-like pattern from the previous experiment was modified with fillets at the corners of the bricks and printed into a plate. Figure 2.8b shows the specimen in the loading configuration. Overall specimen dimensions are 163.2 mm x 104.1 mm

x 9.5 mm. The hole pattern is positioned in the center of the plate with a height of 120 mm with 21.6 mm flanges at the top and bottom of the plate to grip. The specimens are fabricated using a Stratasys Connex3 Objet500 3D printer. DM8530 (E=1020 MPa, ν=0.414) and DM8510 (E=1700-2300 MPa [54]) are selected as materials for different plates. These materials are selected because they are more rigid than DM9895 and less brittle than Vero while maintaining a fairly large elastic contrast. Plates are tested with unfilled holes and with holes filled with an alternate material. Initial notches of length 28 mm, width 0.6 mm and a 30° tip are modeled and printed into specimens. The 20-85 micron print tolerance of small features of the 3D printer is assumed to be sharp enough that further initial cracking is not deemed necessary. The plates with holes are pulled monotonically to failure in a MTS Servohydraulic load frame (Model No. 358.10, max load: 14.7 kN) at a loading rate of 1 mm/min. The plates with filled holes are pulled monotonically to 5340 N (the load was limited due to the loading grips). No crack propagation was observed at this load. The image acquisition procedure described in section 2.2 was also used for these experiments.

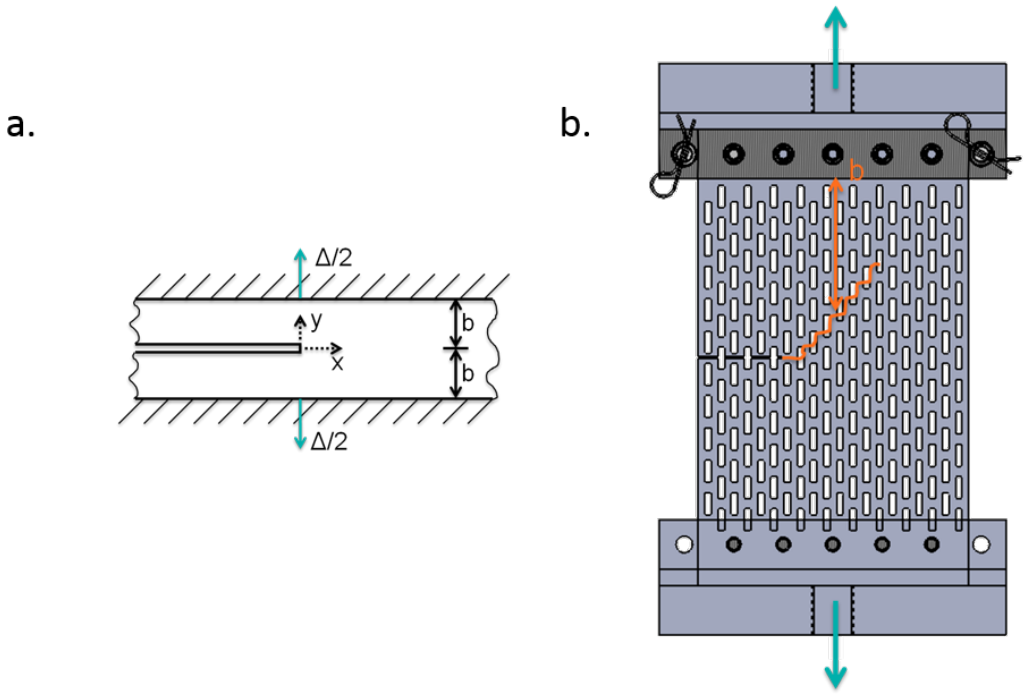

Figure 2.8: a. Schematic of the infinite strip fracture specimen b. Schematic of the of experimental setup.

Discussion

For the plates with unfilled holes, the crack initially propagated horizontally through the remaining ligament of material between the tip of the initial crack and the next hole in the material. Further crack propagation in DM8530 occurred individually in remaining ligaments, stair-stepping up as shown in Fig. 2.9a. Further crack propagation in DM8510 occurred catastrophically, with all of the remaining ligaments in the original crack plane rupturing simultaneously. Figure 2.9 shows the stress-strain loading plots overlaid with the stress intensity factor (K) values calculated each time the crack extends. The energy release rate G is calculated using the following relation [56]:

$$G = 2b(\text{SED})^{\infty}, \tag{2.2}$$

where b is shortest distance between the crack plane and the loading grips, the strain energy density is given by:

$$(\text{SED})^{\infty} = \frac{1}{2}\sigma_{yy}\epsilon_{yy}. \tag{2.3}$$

The stress intensity factor K can be calculated using the Irwin relation:

$$G = \frac{K^2}{E}. \tag{2.4}$$

Figure 2.9 shows the load versus displacement during the experiment overlaid with the stress intensity factor calculated using this method for DM8530 and DM8510 plates with holes. Despite having the same material architecture, the two plates exhibit very different failure behavior. The load for DM8530 plate (more compliant plate, Fig. 2.9a) increases until it reaches a maximum, when the first ligament (with an initial notch) breaks. The load drops a little before increasing again, reaching a maximum (lower than the previous maximum) where the next ligament breaks and the load drops again. This process repeats itself for each ligament, with the load dropping as each ligament ruptures individually. The load for the DM8510 plate (stiffer plate, Fig. 2.9b) is very different. The load increases until it reaches a local maximum, when the first ligament (with an initial notch) breaks and the load drops a little. Then, the load continues increasing (much higher than the previous maximum), until it reaches a new maximum and the rest of the ligaments fail at once. For both plates, the calculated critical stress intensity factor, K, is much lower for the failure of the first ligament (with the notch) than for the second ligament (without the notches). This is not surprising. Recalling the work of Williams on a V-shaped notch, the strength of the singularity at the tip of the sharp notch is much

higher than that of the free face of ligament [26]. Essentially, the crack terminates in the void and must renucleate in order to continue.

The stress in the y-direction, σ_{yy}, is calculated by dividing the measured load by the remaining cross sectional area in plane with the crack as shown in Fig. 2.9b. The strain in the y-direction, ϵ_{yy}, is calculated by dividing the applied displacement by the height of the specimen. The Young's modulus, E, of the composite material is estimated using finite element simulations of the heterogeneous material. The plots indicate increased fracture toughness after an initial crack propagation event.

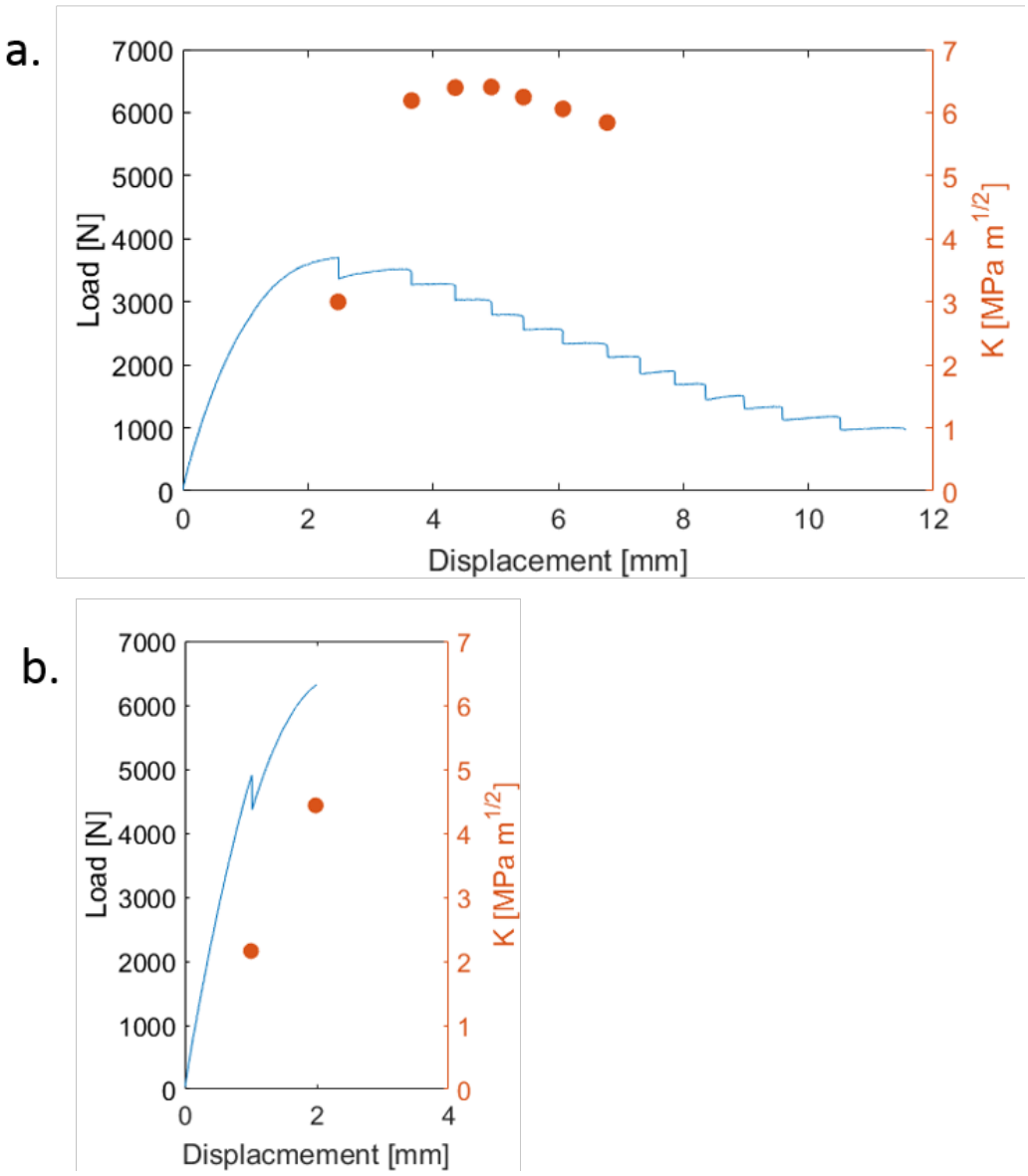

Figure 2.9: Load-displacement plots of plates with holes tensile tests overlaid with markers indicating K values as crack extends for a. DM8530 plate and b. DM8510 plate.

Figure 2.10 shows the hoop ($\epsilon_{\theta\theta}$) strain obtained from DIC measurements for both the plates with holes. These results are obtained by transforming Cartesian strains assuming the origin is at the location the crack will next propagate. The maximum hoop strain is isolated on the ligament immediately adjacent to the crack tip but distributed relatively uniformly elsewhere.

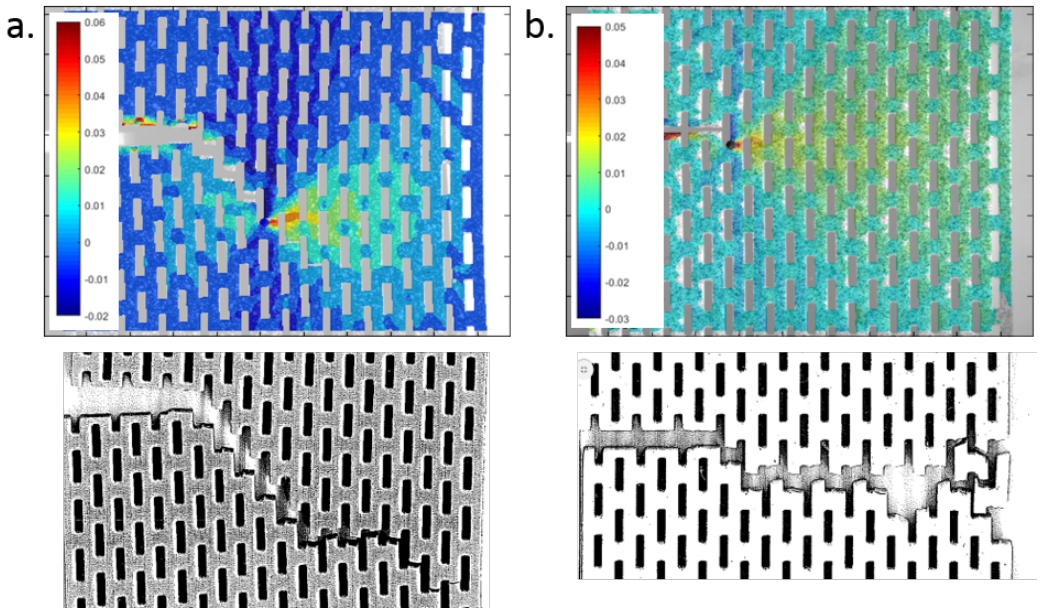

Figure 2.10: Hoop (circumferential) strains ($\epsilon_{\theta\theta}$) and post failure images for (a) DM8530 plate with holes and (b) DM8510 plate with holes. Origin indicated by a black dot at the crack tip.

Figures 2.11 and 2.12 show the individual components of the strain and von Mises stress in the undeformed configuration at the highest load in the experiment. The color of the material can be used to identify the material and therefore the local Young's modulus at any given point in the specimen, because DM8510 is light gray in color while DM8530 is dark grey. However, speckling the surface of the specimen for DIC obscures the color of the material. To determine the Young's modulus, the front (DIC) and back (unpainted) faces of the plates are imaged during the experiment and the images are matched in post-processing using an affine transformation of registration points incorporated into the loading grips. The location of each strain point produced by the DIC algorithm is sampled in the transformed unpainted image and a threshold operation is used to determine the color of the material at the point.

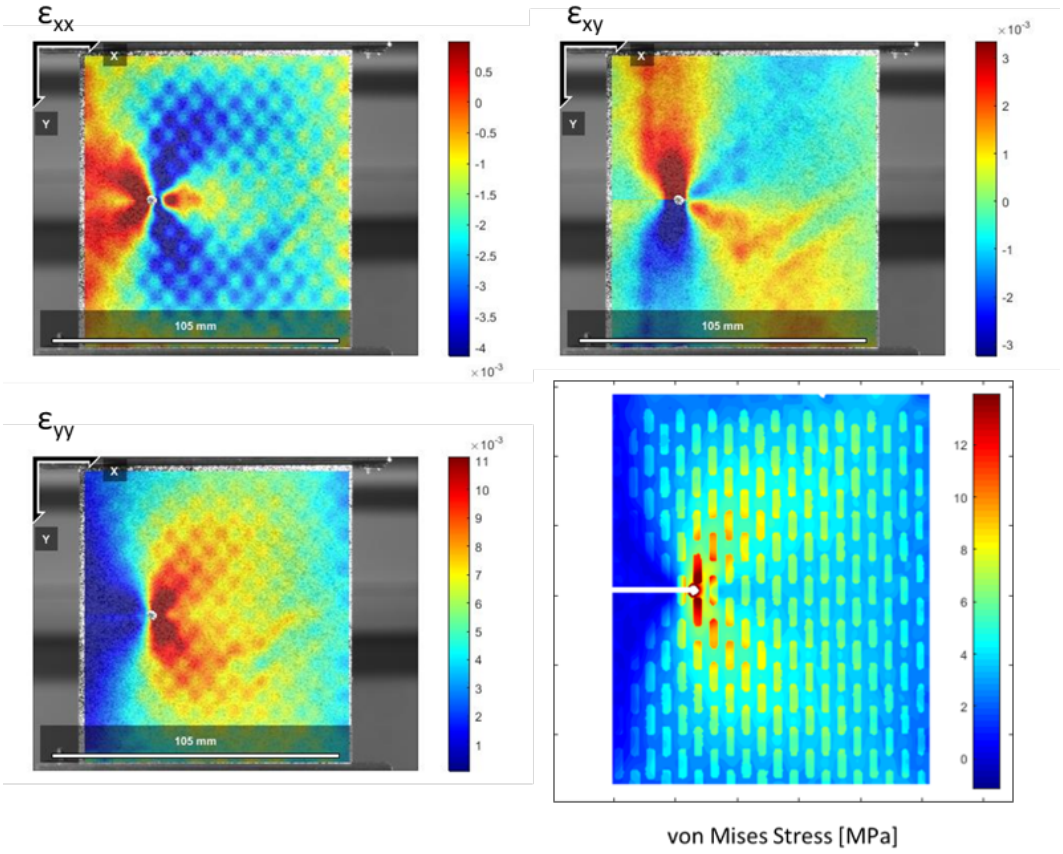

Figure 2.11: Full-field map of strain components and von Mises stress at the highest load for the composite with DM8530 matrix with DM8510 filled holes.

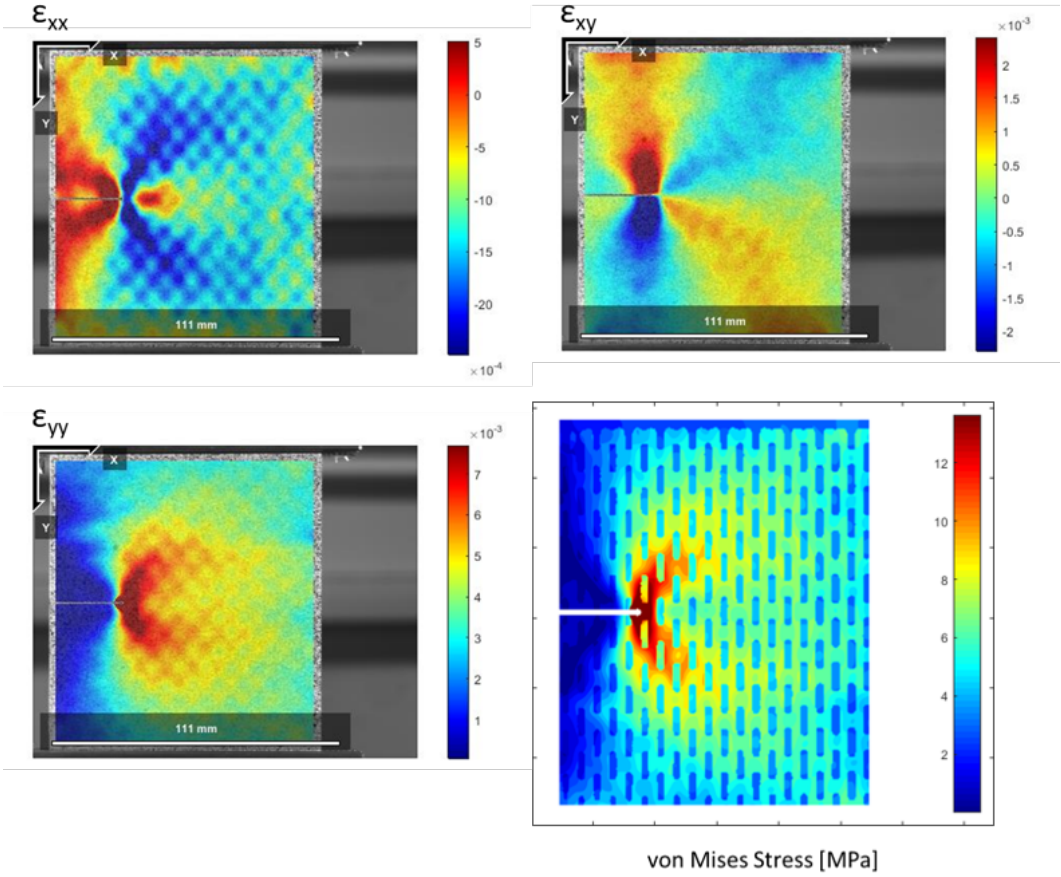

Figure 2.12: Full-field map of strain components and von Mises stress at the highest load for the composite with DM8510 matrix with DM8530 filled holes.

The results indicate increased toughness as the crack propagates through the specimen. This is expected because the crack propagates to the nearest hole where it terminates and must be re-nucleated to continue. It is interesting to note that the 'toughness' of propagating through a ligament with no initial crack was twice that of propagating from a sharp notch for both specimens. Figure 2.10 shows the front faces of the specimens post-experiment. It is notable that the ligaments did not break at the corner of the holes of specimen 1 but rather approximately half a millimeter away while the ligaments of specimen 2 broke at the corners.

For the soft matrix with stiff inclusions (Fig. 2.11), the stress is concentrated in the heterogeneities. For the stiff matrix with the soft inclusions (Fig. 2.12), the stress is concentrated in the matrix.

2.4 Heterogeneous Stripes

Exploratory experiments were performed to determine the influence of the size of heterogeneities on fracture toughness. For this experiment, the heterogeneities are oriented parallel to the crack (also called crack divider orientation) to simplify the analysis. DM8530 (E=1020 MPa, ν=0.414) and Vero (E=1960 MPa, ν=0.399) are used to maximize the material contrast while still being brittle enough to allow the crack to propagate.

Theory

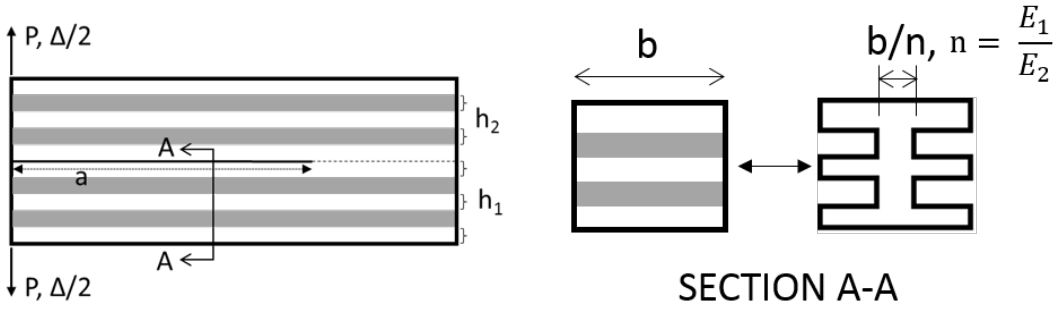

Figure 2.13: Schematic of the double cantilever beam specimen (DCB), cross sectional view of the specimen and equivalent area.

Recall from the introduction that the energy release rate can be written as:

$$G = \frac{1}{2}P^2\frac{dC}{da}, \tag{2.5}$$

where P is the load (per unit thickness), C is the compliance, and a is the crack length. Considering the specimen in Fig. 2.13, the top and bottom of the specimen can be considered as cantilever beams, and the compliance is given as:

$$C = \frac{2}{3}\frac{a^3}{EI}, \tag{2.6}$$

where I is the moment area of inertia [56]. Because the moment area of inertia is independent of the length of the cantilever, the equation for the energy release rate can be given in terms of I:

$$G = \frac{P^2a^2}{EI}. \tag{2.7}$$

Using the method of equivalent areas and the superposition of moments, two materials with different stiffnesses can be approximated as one material to find the composite moment area of inertia.

The specimens are designed so that the crack is in the midplane of a layer of Vero. Assuming that because of this the material will fail at the fracture toughness of the Vero material, using the relation between the energy release rate, G, and the critical stress intensity factor, K_{Ic}, $G = \frac{K^2}{E}$, and rearranging Eq. (2.7) for the critical applied force gives:

$$F = \frac{bK_{Ic}}{a}\sqrt{\frac{I}{b}}, \tag{2.8}$$

where $P = \frac{F}{b}$ and b is the width of the specimen. Figure 2.14 shows a plot of the difference between the force calculated using Eq. (2.8) for two horizontal layers and twenty horizontal layers in each beam for volume fraction of Vero between 0.01 and 0.99. The purpose of this plot is to determine the optimum volume fraction for maximizing toughness due to the horizontal layers. The optimum volume fraction is found to be roughly 0.40.

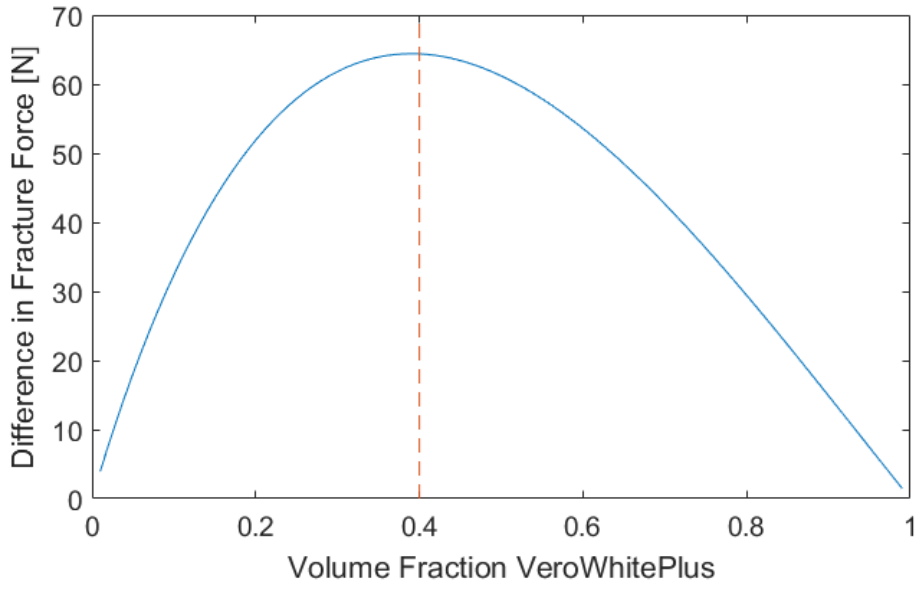

Figure 2.14: Difference in fracture force between a double cantilever beam with two horizontal layers and one with twenty horizontal layers in each beam versus volume fraction of Vero.

Figure 2.15 shows the analytical results of calculating the fracture force for the selected size of compact tension specimen assuming a volume fraction of 0.40.

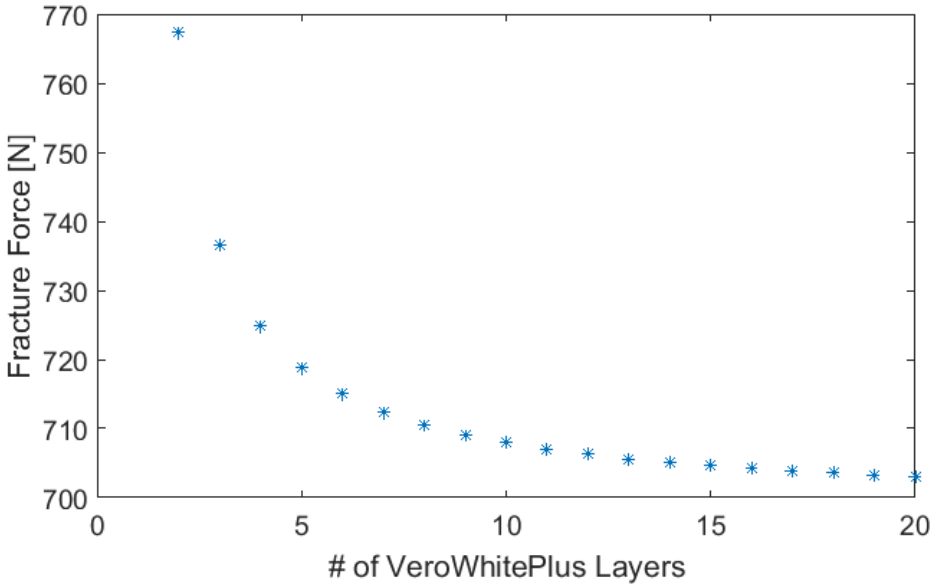

Figure 2.15: Predicted fracture force versus number of Vero layers in each beam.

Experimental

Compact tension specimens designed to the specifications in ASTM standard 5045 are shown in Fig. 2.16 [14]. A volume fraction of 0.40 Vero is used, and specimens are printed with 2, 4, 6, 10, 20, 30 and 40 layers in each beam (three of each layer number are printed). Vero layers are 4.57, 2.29, 1.52, 0.91, 0.46, 0.31 and 0.23 mm thick and DM8530 layers are 13.71, 4.57, 2.74, 1.52, 0.72, 0.47, and 0.35 mm thick, respectively. An initial notch is printed into the specimen. For the 2, 4, 6 and 10 layer specimens, the final depth of the precrack is reached by pressing a razor blade into the notch. Several specimens cracked completely during this operation, leaving some of the layer numbers without the three tests, which was planned for each layer thickness. To reduce the rate at which specimens failed prior to testing, for the 20, 30 and 40 layer specimens the final depth is achieved by sliding a razor across the notch. Only one specimen failed during this operation. The experiments are performed on an MTS Servohydraulic load frame at a displacement rate of 1 mm/min (Model No. 358.10, max load: 14.7 kN). Displacement and load are measured and recorded from the load frame. Some specimens are prepared for DIC with speckle patterns and images of the speckled patterns are taken during the loading. The image acquisition procedure described in section 2.2 was also used for these experiments.

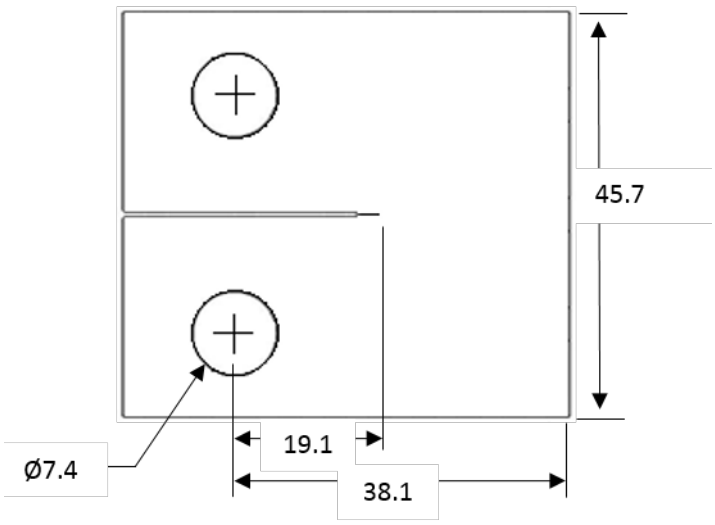

Figure 2.16: Schematic and dimensions (in mm) of compact tension specimen. The specimen is 12.7 mm thick.

Results

Figure 2.17 shows the measured load at fracture. The specimens designated as HH-0616-10-1 and HH-0616-40-3 failed at much lower loads than any of the other specimens. Upon inspection of the fracture surfaces, both specimens show evidence of two fracture events; it is possible the first occurred during precracking compromising the strength of the specimens. Figure 2.18a shows a typical fracture surface with the failure starting at the notch. Figure 2.18b shows the fracture surface for HH-0616-10-1 showing a crack that started and stopped from the lower right edge, and a second crack starting where it ends and propagating through the rest of the specimen. Figure 2.19 shows the full-field strain components and Fig. 2.20 shows the von Mises stress for 2, 4, 20, and 30 layer specimens prior to failure.

Figure 2.21 shows the results of calculating the energy release rate, G, according to ASTM standard 5045 and the J-integral using area based J-integrals from the DIC data (G and J are equivalent in linear elasticity) [56]. Hsueh et al. showed that the J-integral can be calculated for heterogeneous media provided the contour is sufficiently large compared to the the size of the heterogeneity [58]. Calculating the J-integral from DIC data is difficult to do accurately, as the J-integral requires both displacements and strains. DIC measures displacements and calculates the strains by taking the derivatives of the displacements. Noise is inherent to experimentally measured data, and taking the derivative of noisy data amplifies the noise. When the J-integral is computed from this data, the results can be off by orders of magnitude

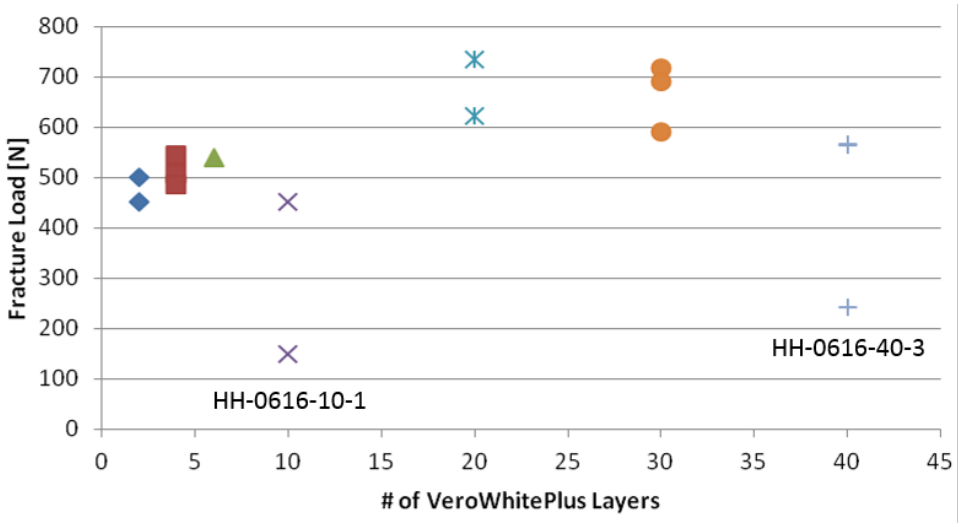

Figure 2.17: Measured fracture load versus number of Vero layers. Two specimens that appear to be outliers are noted with specimen numbers.

[19, 20]. In order to reduce the effects of noise, the DIC strain data is smoothed prior to calculating the J-integral using principal component analysis with local pixel grouping (LPG-PCA) [59]. Principal component analysis (PCA) determines the orthogonal set of vectors that describes the variation in a group of data points. By using only the set of vectors that contributes most to the variation and discarding the rest, data can be smoothed [60]. Local pixel grouping is a technique that uses smaller subsets of the data to effectively denoise data while better preserving local structures. The algorithm used in this work is a two-stage LPG-PCA developed by Zhang et al. [59].

Discussion

The trend predicted by the theory (section 2.4) for the force (toughness) for fracture and the trend observed in the experiment are not in agreement. The fracture force in the experiments rises asymptotically to the 600-700 N while the fracture force predicted by theory descends asymptotically to 700 N. One of the possible reasons for the discrepancy is that the Euler-Bernoulli beam theory is not applicable to the compact tension specimen because the 'beams' are not slender enough. Another possible reason is that the layers of DM8530 are too far away to contribute to fracture toughness in the specimens with a few layers. In the von Mises stress distributions in the specimen shown in Fig. 2.20, the stress is concentrated in a circular region around the crack tip in the two layer specimens and develops into a lobed shape as the number of layers increases.

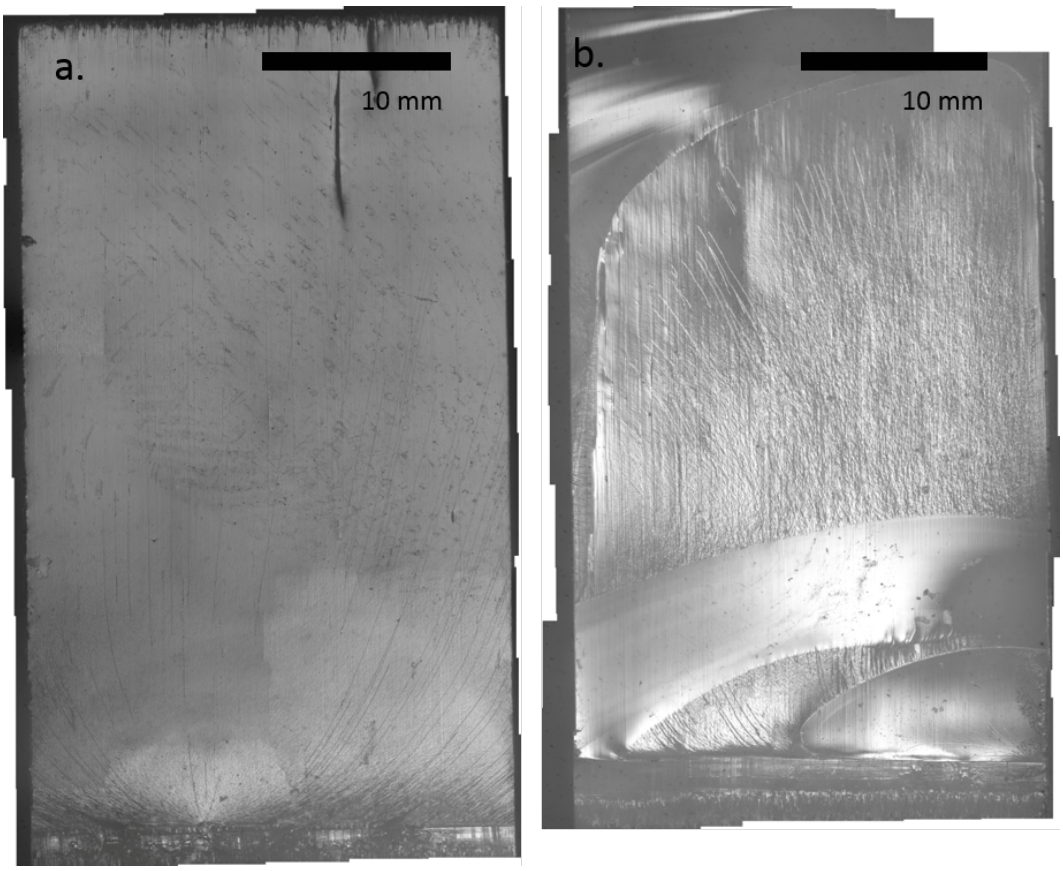

Figure 2.18: a. Fracture surface of HH-0616-10-3 resulting from crack originating at the razor-sharpened notch only. b. Fracture surface of HH-0616-10-1 showing a crack that started and stopped from the lower right edge, and a second crack starting where it ends and propagating through the rest of the specimen.

The LPG-PCA algorithm produced values for J-integral (energy release rate) agree with those determined by using the methodology in ASTM standard 5045 for the smaller number of layers but poorly for the larger number of layers. There may be some error at the large number of layers due to the size of the layers being comparable to the resolution of DIC in the experiments.

2.5 Conclusion

This chapter presented investigations into the fracture behavior of heterogeneous materials. The heterogeneous brick experiment shows that a compliant material can be toughened by the inclusion of stiff heterogeneities. The heterogeneous plate with holes experiments study the inverse problem: a stiff matrix with compliant (E = 0) inclusions. These experiments showed that once the crack reached a hole, continued propagation was dominated by renucleation in the next ligament, greatly increasing

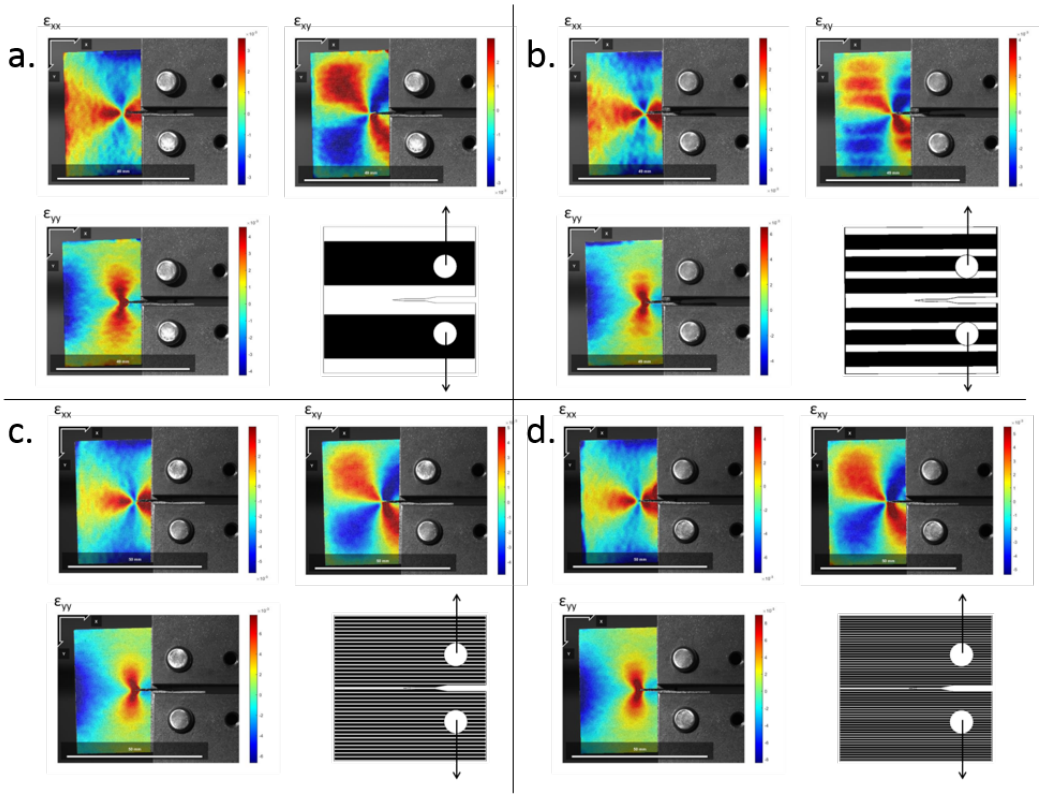

Figure 2.19: Full-field strain components obtained using DIC prior to failure for a. 2; b. 4; c. 20; and d. 30 layer specimens.

resistance to continued fracture.

While useful as preliminary experiments of toughening behavior in heterogeneous materials, experiments employing the brick heterogeneity structure contain too many variables (e.g. the spacing, length, and pattern of the bricks) to determine generalizations that are broadly applicable to all fracture problems. The heterogeneous stripes experiment attempted to study the effect of the size of heterogeneities on toughening behavior in layered materials with the heterogeneities oriented in the plane of the crack. The experimental results did not agree with the proposed theory, and several explanations are proposed. Ultimately, this investigation was abandoned because heterogeneities oriented parallel to the crack only provide minimal toughening and the toughening may not have been measurable separate from the variation seen between specimens of the same configuration.

The following chapter (Ch. 3) builds on the ideas and lessons learned in the experiments presented in this chapter.

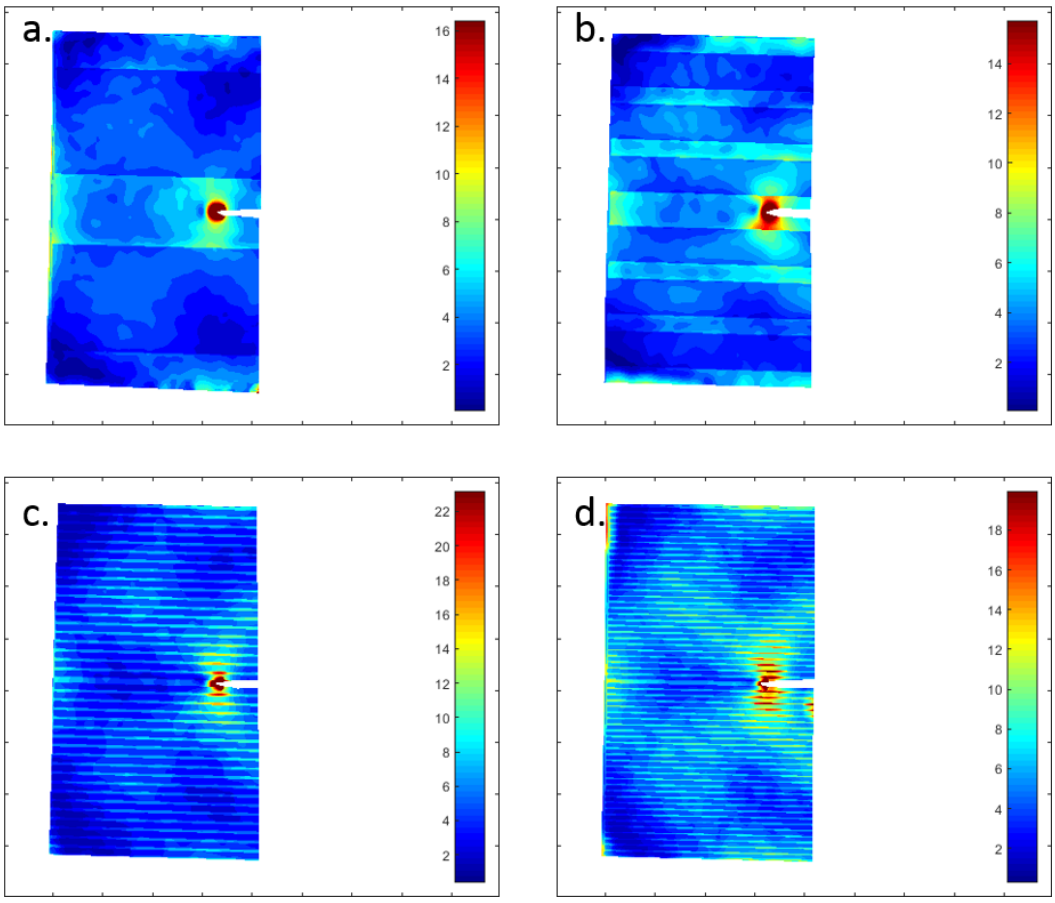

Figure 2.20: Contours of von Mises stress prior to failure for a. 2; b. 4; c. 20; and d. 30 layer specimens.

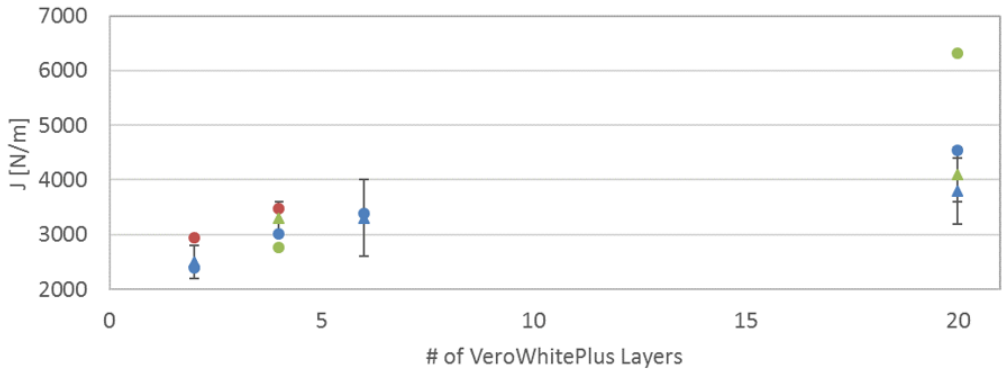

Figure 2.21: *G* calculated from ASTM 5045 (filled circles, assuming linear elasticity *G*=J) and J calculated from LPG-PCA smoothed DIC data (triangles, error bars represent standard deviation of many contours).

Chapter 3

CRACK RENUCLEATION AND PROPAGATION IN PERIODIC LAYERED MEDIA

[1] C.-J. Hsueh, L. Avellar, B. Bourdin, G. Ravichandran, and K. Bhattacharya. "Stress Fluctuation, Crack Renucleation and Toughening in Layered Materials". *Journal of the Mechanics and Physics of Solids* (2018). DOI: 10.1016/j.jmps.2018.04.011.

3.1 Introduction

Many intrinsic and extrinsic factors contribute to toughening a material against fracture. Intrinsic toughening happens ahead of the crack tip and is associated with nucleation and propagation toughening. Crack tip blunting, the process by which the sharpness of the crack tip is reduced due to plastic deformation at the crack tip, is an example of intrinsic toughening. On the other hand, extrinsic toughening happens behind the crack tip and is associated with a crack that is already propagating. Crack bridging, the spanning of the crack opening by material, applies a closing force to the crack, reducing the force driving it forward [1]. While many studies have been devoted to understanding how many of these factors work together to contribute to toughening as a system, it is not understood how they individually contribute to toughening.

Zak and Williams established through theoretical consideration that a layered material heterogeneity enhances fracture toughness in a layered composite material [36]. However, heterogeneities do not need to be layered in order to contribute to toughening. Faber and Evans determined that heterogeneous particles embedded in a material can cause crack deflection that results in toughening [34]. Using theoretical considerations, Bower and Ortiz determined that tough particles in a brittle matrix contribute to crack trapping and crack bridging behavior which are effective toughening mechanisms [61]. Argon and Cohen's experimental studies on polycarbonate rod reinforced brittle epoxies agreed well with Bower and Ortiz's theory [62].

Using variational phase field simulation, Hossain et al. showed that elastic contrasts can be incorporated into material architectures that increase fracture toughness [10]. Wang and Xia used computational analysis and experiments to show that contrast

in elastic modulus could be used to increase fracture resistance in layered materials, subject to the size of the layers being sufficiently large compared to the size of the cohesive zone and provided an appropriate volume fraction of constituent materials is present [37]. Hsueh et al. performed experiments on heterogeneous materials showing improved fracture toughness due to the presence of elastic heterogeneity [63].

One of the common results of studies of heterogeneous fracture toughness is that increasing the complexity of material architecture increases resistance to fracture [11, 64]. It is understood that heterogeneities contribute to fracture resistance both by redistributing the stress at the crack tip thereby reducing the crack driving force and, in some cases, reducing the stress intensity to zero causing the crack to renucleate in order penetrate an interface; however, the relative importance of each of these mechanisms is not well understood.

This chapter investigates the individual contributions of elastic contrast and crack renucleation to fracture toughening through experiments using 3D printed layered architectures. VeroWhitePlus and DM8530 (Young's modulus: E=1960 MPa and E=1020 MPa, respectively section 2.1) are the two 3D printed constituent materials used in the experimental architectures. This chapter begins with experiments to determine the homogeneous fracture properties of the two materials. Computational modeling, theoretical considerations and experiments on material architectures designed to separate the effects of elastic contrast and renucleation follow.

3.2 Evaluation of Fracture Toughness in Homogeneous Materials

Quantitative Fractography

A great deal of information about fracture can be determined from observations of the fracture surfaces post material failure using fractography. Information about the initiation and nucleation of a crack from a flaw and subsequent propagation can be determined from observing the fracture surfaces at low levels of magnification using optical microscopy. The fundamental features of a fracture surface after brittle fracture (i.e. little to no yielding is present) are the flaw, mirror, mist, and hackle (Fig. 3.1a) [16, 65, 66]. The crack originates at the flaw, which acts as a stress concentration. When the load reaches a critical value, the crack propagates resulting in the failure of the material. The crack propagates slowly in the mirror region where the surface is smoothest and quickly in the hackle region where the surface is roughest; as the crack picks up speed in the mist region, resulting in a

	a [mm]	b [mm]	σ_{yield} [MPa]	σ_{fail} [MPa]	K_{IC} [MPa $m^{0.5}$]
1A	1.10	1.04	47.9	31.5	1.30
1B	1.10	0.94	47.9	31.5	1.27
4A	1.27	0.98	48.9	32.4	1.37
4B	1.26	0.96	48.9	32.4	1.36
5B	0.97	0.64	51.8	33.4	1.18
AVG					1.30

Table 3.1: Flaw dimensions and mechanical and fracture properties of VeroBlack-Plus. The flaw size is determined from quantitative fractography (Fig. 3.1c) and mechanical properties from tensile tests.

transition where the surface has parabolic gouges [16, 65]. In fracture experiments on ceramics, it was observed that:

$$\sigma\sqrt{c} = \text{material const}, \tag{3.1}$$

where σ is the fracture stress and c is the critical flaw size [66]. Irwin derived the critical stress intensity factor (K_{Ic}) of an elliptic flaw in a plate (Fig. 3.1b):

$$K_{IC}^2 = \frac{1.2\sigma^2 a}{\Phi^2 - 0.212(\frac{\sigma}{\sigma_{YS}})^2}, \tag{3.2}$$

where σ is the fracture load, a is the radius of the minor axis of the flaw, σ_{YS} is the yield strength and Φ is the elliptic integral of the second kind [67]. Randall combined Eqs. (3.1) and (3.2) to develop an experimental technique to determine the fracture toughness of ceramics by measuring the size of the flaw and the failure stress of a uniaxial tension specimen [68]. Plangsangmas showed that the technique could be extended to polymers and diFrancesco showed that it was accurate for polymers compared to other methods of calculating fracture toughness, such as compact tension and single edge notch bend tests [18, 65].

Quantitative fractography is used to determine the fracture toughness of VeroBlack-Plus, the stiffer of the constituent materials. Dogbone specimens (ASTM D638) were tested to failure as described in section 2.1. After failure, the fracture surfaces were analyzed to measure the major (a) and the minor (b) axes of the flaw using a Nikon Measurescope MM-22 with 2.5x-5.0x objectives. The data from the elliptical crack can be used to construct an equivalent circular crack with radius $c = (ab)^{\frac{1}{2}}$ [65].

Using the flaw size from the quantitative fractography (Fig. 3.1c) analysis (Table 3.1) and the mechanical properties from the tensile test (Section 2.1, Table 2.1), the

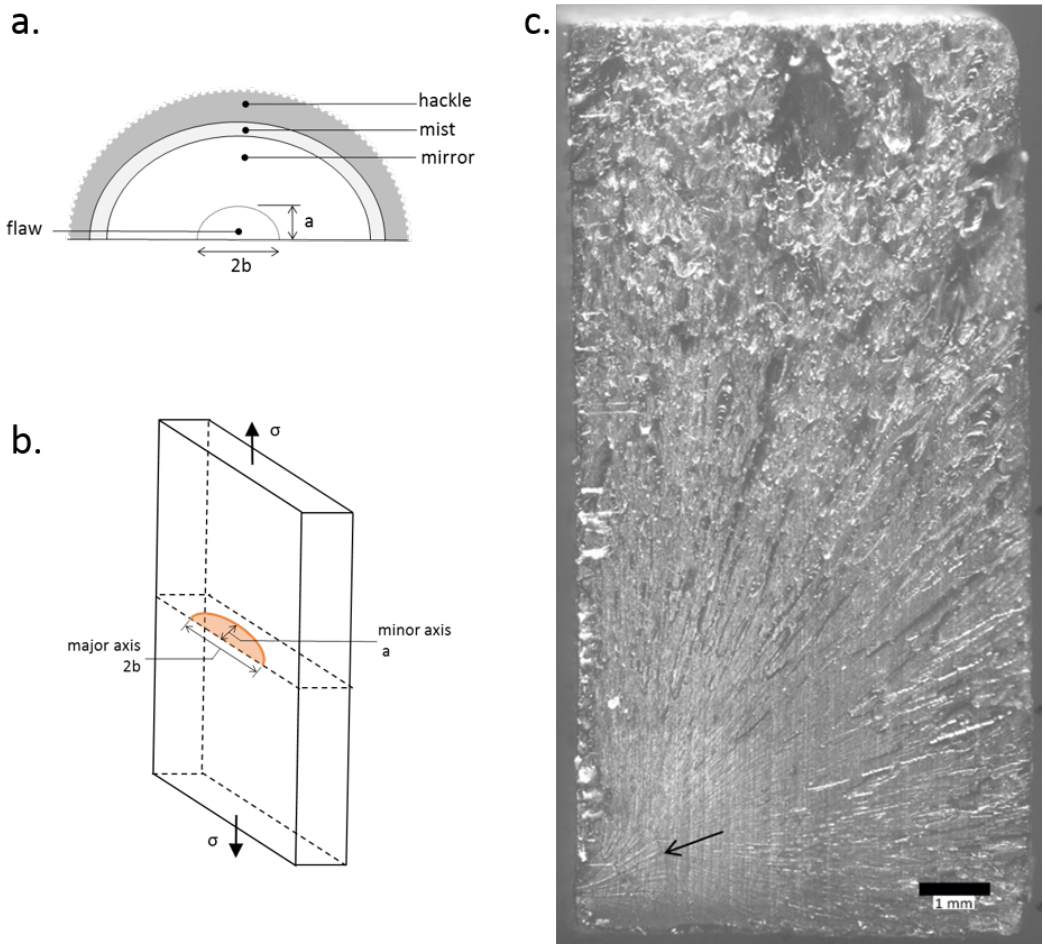

Figure 3.1: a. Schematic of the flaw, mirror, mist and hackle regions on a fracture surface; b. Schematic of the elliptical crack in a plate problem; c. Fracture surface of a VeroBlackPlus specimen (2.5x magnification) subjected to uniaxial tension. The black arrow points to the flaw.

Mode I average critical stress intensity factor for VeroBlackPlus using Eq. (3.2) was estimated to be $K_{IC} = 1.3$ MPa$\sqrt{\text{m}}$.

Compliance Method

Recall from section 1.1 that the critical energy release rate, G_C, of a material can be determined by measuring the change of compliance with respect to crack length $G_C = \frac{1}{2}P^2\frac{dC}{da}$, where C is the compliance (slope of the displacement versus load during a tensile test), a is the crack length, and P is the load at failure. This method is used to determine the energy release rate of DM8530, the more compliant of the two constituent materials. Quantitative fractography is not being used for DM8530

because its elongation at break is much higher than Vero[1]; as a result, the ASTM tensile dogbone specimens could not be pulled to failure with the stroke available in the load frame that was used to measure the tensile material properties.

Experimental

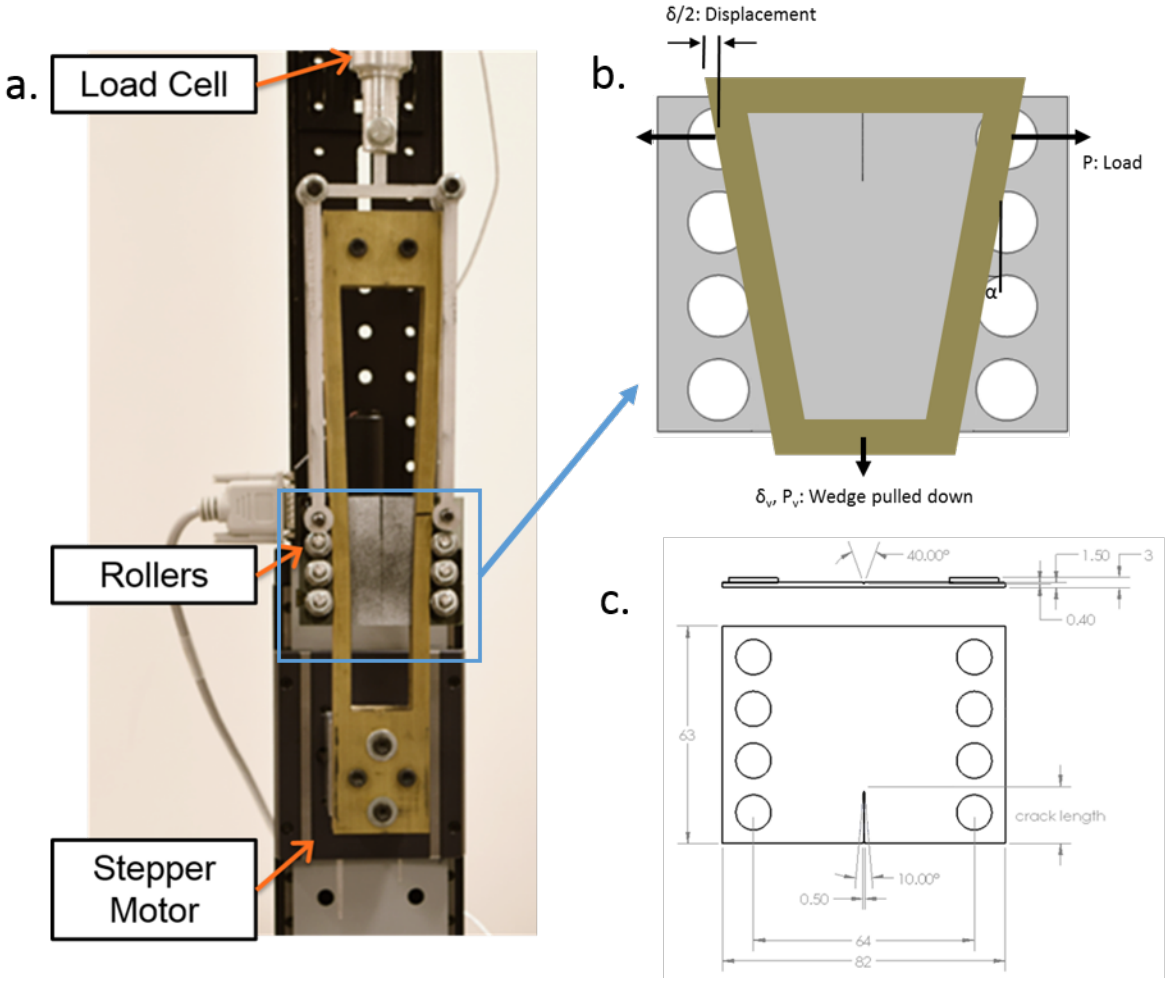

Figure 3.2: a. Picture of the wedge loading experimental setup; b. Schematic of the specimen and the rail; c. Schematic of the specimen with the dimensions in mm.

The experimental test setup and specimen dimensions are shown in Fig. 3.2. The specimen is suspended from the load cell using two aluminum arms that support the top pair of holes (Fig. 3.2). Each loading hole is fitted with a stub with a clearance fit steel bushing and ball-bearing collars. The brass wedge is water-jetted and polished to create a smooth contact surface between the collars and the wedge.

[1]The values published by Stratasys for elongation at break are 10-15% for Vero and 15-25% for DM8530 [54]

The specimen is suspended from the top two loading holes and is, initially, the only contact point. The wedge is mounted on a PI M-410.CG motor controlled via a C-863 Mercury controller. The opening displacement is applied by pulling the wedge down through the loading points, pushing them apart. The angle of the wedge is 2.20°. The other loading points keep the specimen aligned symmetrically on the rail and help prevent out of plane deformation as the test progresses. The wedge is monotonically pulled down at a rate of 0.5 mm/s, which corresponds to an opening displacement, δ, of 0.0383 mm/s (2.3 mm/min). Additionally, the motor controller is programmed to provide digital signals corresponding to its motion, from which applied displacement can be determined using the known stage velocity.

The load applied by pulling the wedge down is measured using an Interface Inc. (Scottsdale, AZ) WMC-25 load cell. An Omega DP25B-S-A1 (Omega, Norwalk, CT) strain meter processes the load signal and converts it to a scaled analog output. A NI USB-6251 BNC DAQ (National Instruments, Austin, TX) acquires the digital signals from the motor controller and analog signal from the strain meter. The front face of the specimen is prepared for DIC imaging with a speckle pattern if that is desired and imaged during the experiment. Images are captured using an Edmund Optics (Barrington, NJ) EO-1312M CCD Monochrome Camera. A LabVIEW (National Instruments, Austin, TX) virtual instrument (VI) gathers and saves data from the camera, strain meter and motor controller.

The compliance is calculated by measuring the slope of the displacement versus load plots, excluding the initial loading toe. The slope of the compliance curve, dC/da, is found by plotting the individual compliance values against the measured crack lengths, fitting a line to the data and taking its slope. The load, P, is taken as the failure load of the specimen.

Validation Using Acrylic

Fracture specimens with an initial notch are laser cut from 3.175 mm thick acrylic. A sharp crack is introduced into the specimen by pressing a fresh razor blade into the notch until the depth of the sharp crack is at least as long as the width of the initial notch. Pre-crack length ranges from 14.5 to 16.5 mm (22% - 25% of specimen length). The precise measurement of the length of the initial crack is taken after specimen failure using calipers from the failure surface. The compliance measurements versus the measured crack length are shown in Fig. 3.3. The critical strain energy release rate for the normal pull speed of 0.5 mm/s was estimated using

the compliance method to be 1.05±0.23 kJ/m^2.

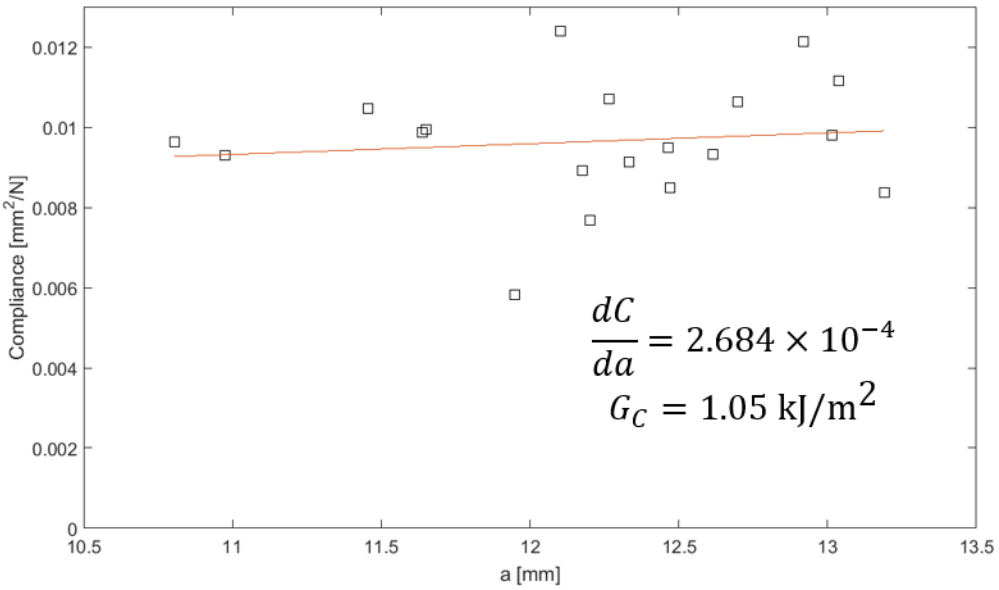

Figure 3.3: Compliance vs crack length plot for acrylic with a sharp crack.

Toughness of DM8530

Specimens of the compliant material are 3D-printed by Stratasys Direct Manufacturing (Eden Prairie, MN) and sent by overnight mail. The specimens were individually saran-wrapped and bagged to mitigate exposure to air. Specimens are printed without an initial notch to make them more robust to shipment. The initial notch is sawed into the specimens using a fine-toothed saw. The notch position is controlled using a laser-cut jig. The initial sharp crack front is achieved by pressing a fresh razor blade into the specimen to a depth of at least the width of the initial notch. The precise measurement of the total length of the initial notch is taken after specimen failure using calipers on the failure surface.

The specimens are loaded twice to a sub-critical load before the final loading to failure. The compliance for each of these loadings is averaged. The compliance measurements versus the measured crack length are shown in Fig. 3.4. The critical strain energy release rate (G) was estimated using the compliance method to be 27.6±9.7 kJ/m^2.

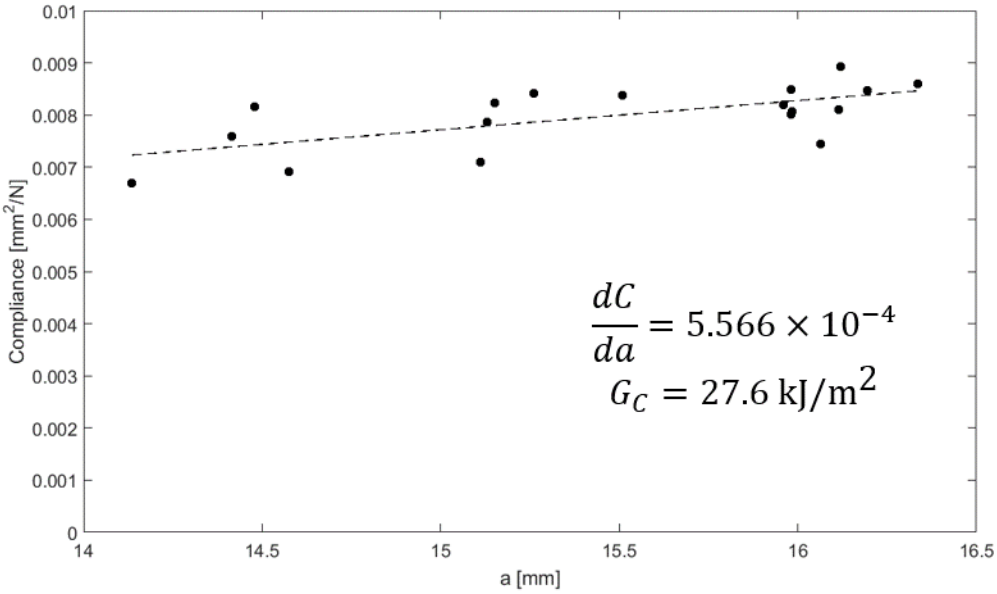

Figure 3.4: Compliance vs crack length plot for homogeneous DM8530.

3.3 Renucleation and Toughening

Two mechanisms of toughening are to be considered in this section: the effect of an elastic contrast at a bi-material interface and of crack renucleation as it passes through the interface. In order to separate the effects of these mechanisms, it is proposed to 'remove' the interfaces by introducing a thin spine of material in the plane of fracture. Schematics of these architectures are shown in Fig. 3.5. By comparing the results of propagating a crack through a material with and without interfaces, the individual contribution of renucleation to overall toughening can be determined.

Computational Analysis

The computational analysis described in this section is adapted from the dissertation of Chun-Jen Hsueh [63]. Simulations are performed using the phase field fracture approach [69, 70, 71, 72]. This is a regularized method that introduces a scalar field v taking values in [0, 1] to describe the material state with regions with $v = 0$ representing intact material and regions with $v > 0$ representing regularized cracks. The energy functional for this approach is:

$$\mathcal{E}^{\ell}(u, v) = \int_{\Omega} \frac{(1-v)^2}{2} e(u) : C : e(u) + \frac{3G}{8}\left(\frac{v}{\ell} + \ell|\nabla v|^2\right) dx\,, \tag{3.3}$$

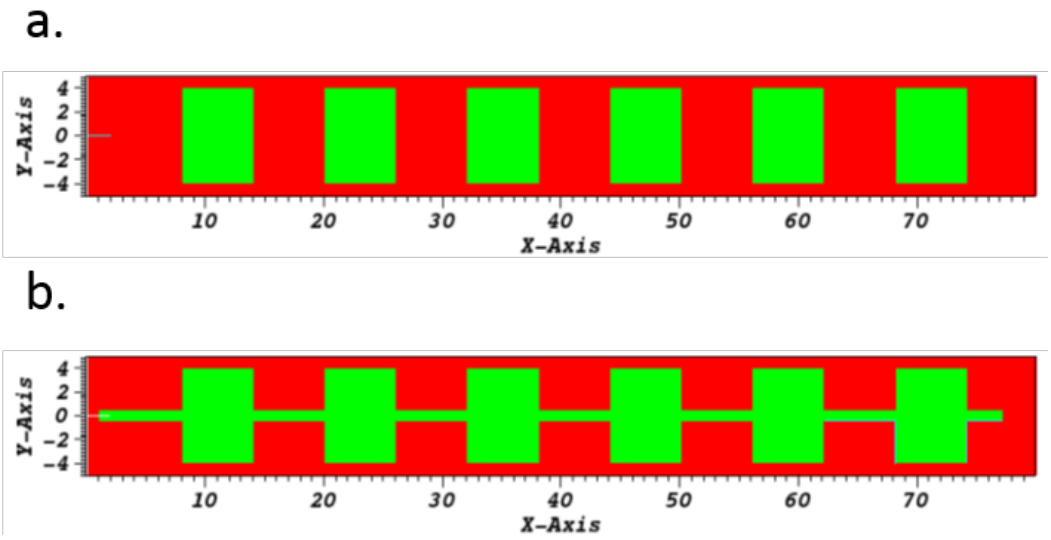

Figure 3.5: a. Periodic layered media without spine; b. Periodic layered media with spine. Red is the stiff material and green is the compliant material [29].

where C is the elastic modulus, $e(u)$ is the strain associated with the displacement u, G is the critical energy release rate and ℓ is an internal length. It can be rigorously shown that this phase field fracture method in Eq. (3.3) approximates (i.e., Γ-converges to) the classical brittle fracture model when the internal length ℓ approaches 0 [73]. The body is subjected to some time-dependent boundary condition and at each time the energy is minimized subject to the boundary condition and the constraints that v is monotone increasing and $0 \leq v \leq 1$. The solutions are characterized by crack-like regions of width $O(\ell)$ which are the regularized cracks. It has been shown that cracks nucleate in this model when the stress reaches a critical value that depends on the domain and the loading mode. In uniaxial tension, the critical stress is:

$$\sigma_c = \sqrt{\frac{3GE}{8\ell}}\,. \tag{3.4}$$

This critical stress for crack nucleation increases with decreasing ℓ, and ℓ may be regarded as a parameter that determines crack nucleation [74, 75]. For details of the numerical implementation, refer to Bourdin [71].

Following Hossain et al. [10], the so-called surfing boundary condition is used in the following simulations. This boundary condition is a time-dependent steadily translating crack opening displacement field:

$$u^*(e_1, x_2, t) = U(x_1 - vt, x_2) \tag{3.5}$$

with U to be the mode I crack opening field

$$U(x_1, x_2) = \frac{K_I}{2\mu}\sqrt{\frac{r}{2\pi}}(\kappa - \cos\theta)(\cos\frac{\theta}{2}\hat{e}_1 + \sin\frac{\theta}{2}\hat{e}_1) \tag{3.6}$$

for some fixed stress intensity factor K_I, effective shear modulus μ, effective bulk modulus κ, $r = \sqrt{x_1^2 + x_2^2}$, $\theta = \arctan(x_2/x_1)$ and v is the translation velocity. This boundary condition forces a macroscopic mode I crack opening that translates at a steady velocity, but does not constrain the crack growth at the microscopic scale. In particular, if the material is heterogeneous, the crack can propagate in an unsteady manner, meander, branch, nucleate daughter cracks, etc. As it does so, the forces on the boundary fluctuate. The energy release rate or J-integral is computed at the boundary at each instant; this value fluctuates and the peak value is taken to be the effective toughness. If the domain is large compared to the scale of the heterogeneities and if the crack is sufficiently far from the boundary then the J-integral is path independent [58]. Further, the effective toughness is independent of the specific form of U and of v [10].

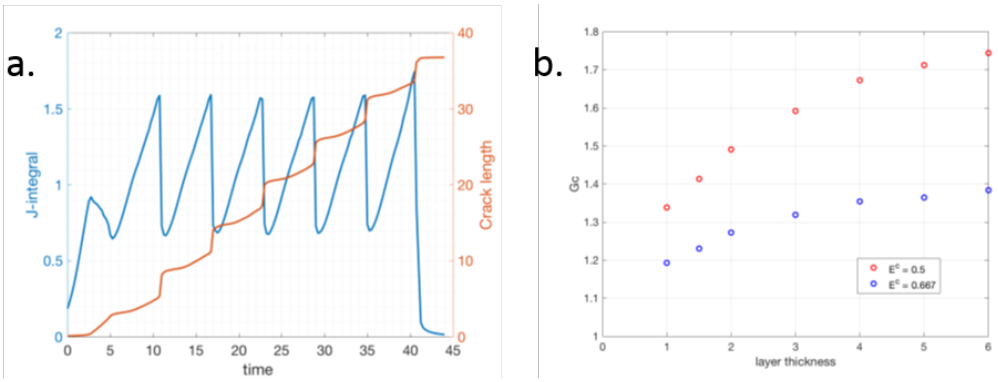

Figure 3.6: Crack propagation through a layered material without a spine. a. Crack tip position and J-integral versus time with $E^c/E^s = 0.5$ and layer thickness 4. b. Effective toughness (G_c) versus layer thickness (t) for two elastic contrasts [29].

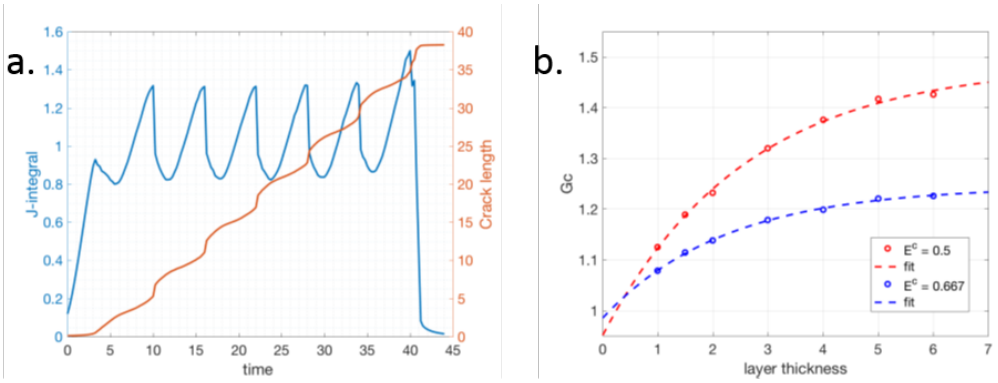

Figure 3.7: Crack propagation through a layered material with a spine. a. Crack tip position and J-integral versus time with $E^c/E^s = 0.5$ and layer thickness 4. b. Effective toughness (G_c) versus layer thickness (t) for two elastic contrasts. The dashed lines are the exponential fits $G_c^{eff} = c_0 + c_1 \exp^{-\frac{t}{c_3}}$ [29].

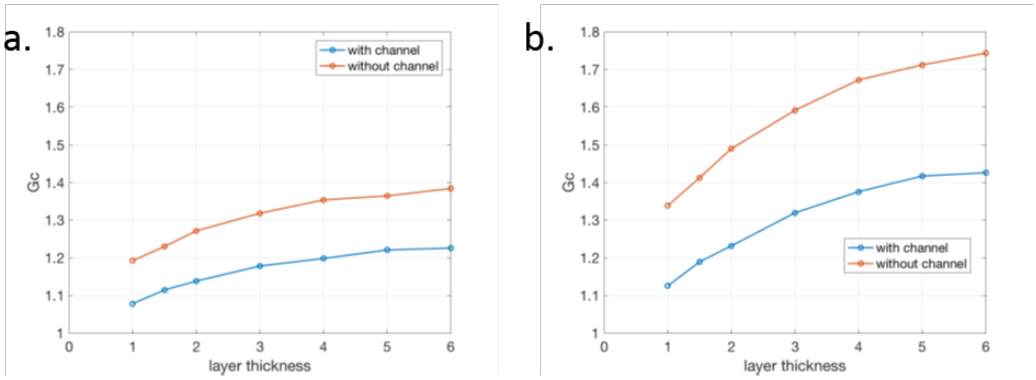

Figure 3.8: Comparison of the toughening for the two microstructures for two separate elastic heterogeneities: a. $E^c/E^s = 0.6674$ and b. $E^c/E^s = 0.5$. Both microstructures result in toughening, but it is more pronounced in the case of the layered material (without the spine) [29].

Phase field fracture simulations are used to study the two microstructures shown in Fig. 3.5. All of the following computational results are presented in non-dimensional units. Figure 3.5a shows a microstructure with alternating layers while Fig. 3.5b shows a microstructure with alternating layers with a thin central spine running through it. Plane strain conditions are assumed where both constituent materials have uniform toughness $G_c = 1$, Poisson's ratio $\nu = 0$ and internal length $\ell = 0.45$. The Young's moduli are different and $E_s = 1$ in the stiff phase (red) material and either $E_c = 0.5$ or $E_c = 0.667$ in the compliant (green) material. The thin central spine is always made of the compliant material. The crack is introduced on the left and the surfing boundary condition drives the crack to the

right. Because of the symmetry of the microstructure and the loading, the crack remains straight. However, it propagates in an unsteady manner as the state of stress is not uniform. Further, it is forced to move from one material to another in the layered microstructure but is always confined to one material in the presence of the central spine. Heuristically, the stress distribution is similar in both materials, but one has renucleation in the layered material (Fig. 3.5a) but not in the layered material with a spine (Fig. 3.5b).

Figure 3.6 shows the results of crack propagation in the layered material. Figure 3.6a shows that the crack is pinned at the interface going from the compliant to the stiff material leading to a rise in the J-integral. This determines the effective toughness which is significantly higher than the uniform material value of one thereby demonstrating the toughening due to elastic heterogeneity. The effective toughness is shown for two separate contrasts and for various layer thickness in Fig. 3.6b. The effective toughness increases with contrast, and it increases with layer thickness reaching an asymptotic value for large layer thickness. Figure 3.7 shows the corresponding result in the layered material with a central channel. There is toughening in this system as well, but the amount of toughening is smaller in this case. These results for the two materials are contrasted in Fig. 3.8. There is toughening in both microstructures for each layer thickness, but the toughening is more pronounced in the specimen without the channel and with the larger elastic contrast.

Theory

The state of stress near an interface is not uniform due the elastic contrast, thus the crack-tip experiences different driving force. Because the channel containing the crack is narrow, this stress heterogeneity mechanism is operative in both materials. The following simple model is proposed to estimate the toughening due to stress heterogeneity. Consider a layered architecture of two materials with Young's modulus $E^s > E^c$ under tensile loading along the layers. Due to compatibility, the longitudinal strain in both layers must be the same. This implies that the ratio between the stresses in a layer and the average stress is equal to the ratio of the Young's modulus of the material to the average Young's modulus:

$$\epsilon^s = \epsilon^c \quad \Rightarrow \quad E^{eff} = \langle E \rangle, \quad \frac{\sigma^i}{\langle \sigma \rangle} = \frac{E^i}{\langle E \rangle} \quad i = s, c\,, \tag{3.7}$$

where $\langle \cdot \rangle$ indicates the volume average. If the layer thickness is large enough that the K-dominant region is in a single layer and the crack tip is in material i, then the

stress-intensity factor at the crack tip is proportional to the stress σ^i in the material i. From Irwin's formula for the energy release rate under plane stress $G = (1-\nu^2)\frac{K_I^2}{E}$:

$$G^i = C\frac{|\sigma^i|^2}{E^i} = C\frac{\langle\sigma\rangle^2}{\langle E\rangle}\frac{E^i}{\langle E\rangle} = G^i_{macro}\frac{E^i}{\langle E\rangle} \quad \Rightarrow \quad \frac{G^i}{G^i_{macro}} = \frac{E^i}{\langle E\rangle}, \tag{3.8}$$

where C is a geometric factor and G^i_{macro} is the macroscopic energy release rate when the crack-tip is in the ith layer using Eq. (3.7). The ratio between the local and macroscopic energy release rate is equal to the ratio between the local and average elastic modulus. Because $G = G_c$ for the crack to propagate:

$$G^{macro} = \begin{cases} \frac{G^c_C\langle E\rangle}{E^c} & \text{crack-tip in compliant material} \\ \frac{G^s_C\langle E\rangle}{E^s} & \text{crack-tip in stiff material} \end{cases} \tag{3.9}$$

The effective toughness is given by the maximum macroscopic energy release rate:

$$G^{eff}_C = \max\{G^c_C\frac{\langle E\rangle}{E^c}, G^s_C\frac{\langle E\rangle}{E^s}\}\,. \tag{3.10}$$

Recall the Zak and Williams analysis of the strength of singularity at the crack tip near a bi-material interface from section 1.2 [36]. They showed that in the case of the crack propagating from a soft to a stiff material, the power of r tends towards zero sending the crack driving force to zero. The crack must renucleate at this interface. In order to do so, additional driving force must be applied which results in increased fracture toughness. The additional toughness is the difference between the toughness of the layers with and without the channel containing the crack.

In order to quantify the additional toughening, consider the crack nucleation criterion Tanné et al. proposed based on simulations of crack initiation due to a V-notch of half-angle ω described in section 1.1 [75]. Define the generalized stress-intensity factor:

$$K = \frac{\sigma_{\theta\theta}}{r^{\lambda-1}}|_{r\to 0}\,. \tag{3.11}$$

The crack nucleates when this generalized stress-intensity factor reaches a critical value K_c that depends on λ. The variational phase-field simulations presented by Tanné et al. are well approximated by:

$$K_c = K_{Ic}^{2-2\lambda}\sigma_c^{2\lambda-1}, \tag{3.12}$$

where K_{Ic} is the critical stress intensity factor and σ_c is the critical stress at which a crack nucleates at a free edge. When $\omega = 0,\ \lambda = 1/2$, Eq. (3.12) recovers the

crack propagation criterion $K_I = K_{Ic}$. When $\omega = \pi/2,\ \lambda = 1$, Eq. (3.12) recovers the critical stress crack nucleation criterion $\sigma = \sigma_c$. Tanné et al. showed that their results were in agreement with numerous experimental observations.

This nucleation criterion, Eq. (3.12), is used to study the toughening due to renucleation at interfaces in a layered system. Define the generalized stress-intensity factor:

$$K = \frac{\sigma}{L^{\lambda-1}}, \tag{3.13}$$

where σ is the macroscopic stress and L is a configuration dependent characteristic length. The crack nucleates when:

$$\frac{\sigma_f}{L^{\lambda-1}} = K_{Ic}^{2-2\lambda}\sigma_c^{2\lambda-1} = \frac{K_{Ic}L^{\lambda-1}}{l_{ch}^{\frac{2\lambda-1}{2}}}, \tag{3.14}$$

where σ_f is the stress at which failure occurs, and $l_{ch} = (K_{Ic}/\sigma c)^2$ is a material length. The failure stress is related to the effective critical energy release rate:

$$G_c^{eff,rn} = L\frac{\sigma_f^2}{E}, \tag{3.15}$$

where 'rn' indicate that this is toughening due to renucleation. Combining with 3.14 and the critical energy release rate in plane strain $G_c = (1-\nu^2)K_{Ic}^2/E$:

$$G_c^{eff,rn} = \frac{G_c}{1-\nu^2}\left(\frac{L}{l_{ch}}\right)^{2\lambda-1}. \tag{3.16}$$

Figure 3.9 compares Eq. (3.16) to the results of Tanné et al. and finds good agreement if $L = 0.962$. The renucleation toughening of 0.178 and 0.317 for $E_c/E_s = 0.667$ and $E_c/E_s = 0.5$ agree well with the asymptotic difference between toughening in layered materials with and without a spine in Fig. 3.8.

Specimen Design and Printing

Figure 3.10 shows representative dimensions of the specimens. Layer thicknesses of 1.5 mm and 3.0 mm are used with a spine thickness of 0.6 mm. Five specimens of both layer thicknesses with and without the spine are printed in a single print. Features, such as loading holes, side groove, and initial crack are 3D printed into the specimens. The specimens are grooved on only one side to allow for DIC visualization of the other side. The specimens are printed in stiff and brittle VeroWhitePlus (Vero) and more compliant DM8530. In specimens containing a spine, the spine material is DM8530.

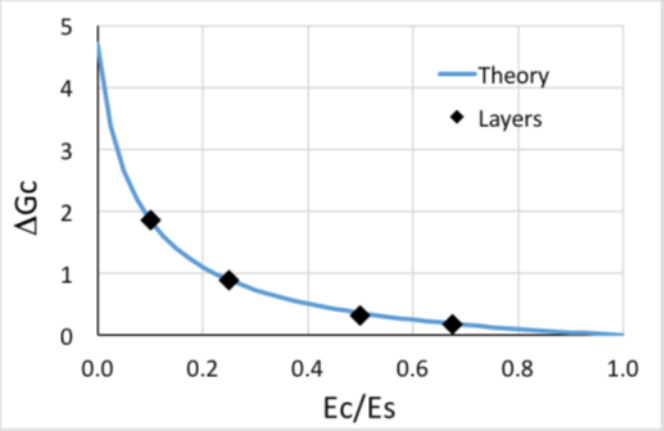

Figure 3.9: Comparison of toughening due to renucleation predicted by Tanné et al. [30] and toughening due to renucleation predicted by Eq. (3.16) [29].

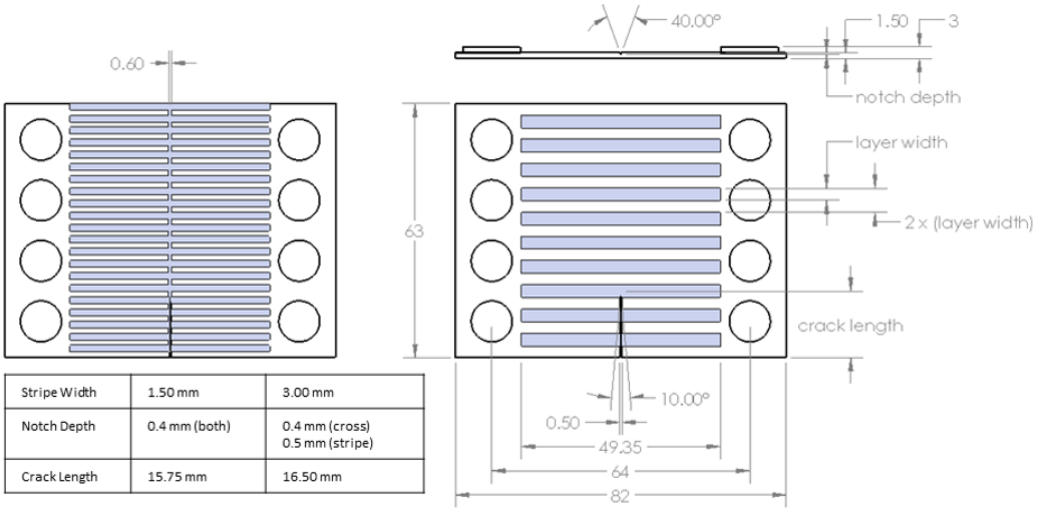

Stripe Width	1.50 mm	3.00 mm
Notch Depth	0.4 mm (both)	0.4 mm (cross) 0.5 mm (stripe)
Crack Length	15.75 mm	16.50 mm

Figure 3.10: Representative specimen dimensions for the stripe geometry. Grey is DM8530; white is Vero. Dimensions are in mm [29].

Specimens of different types are alternated on the print bed in order to mitigate the effects of any local imperfections introduced by the printer. Additionally, the specimens are distributed at a 45° angle relative to the travel direction of the print head. Poor interface strength was observed in experiments when the stripe direction was aligned with the motion of the print head. It was common for the interfaces to debond before the crack could reach the interface or for the crack to turn and propagate along the interface. Neither of these behaviors have been observed in specimens that were oriented at 45° during printing.

Post-printing, specimens are stored for five days prior to testing in a sealed bag to

mitigate exposure to air. Multiple material thickness measurements are taken and averaged for each specimen. Manufacturer published printer tolerances are similar to that of a blunt crack, so a razor blade is pressed into the crack to create a sharper crack tip.

Methods and Results

Specimens are loaded using the wedge loading setup shown in Fig. 3.2ab and described in section 3.2. The wedge is monotonically pulled down at a rate of 0.5 mm/s, which corresponds to an opening displacement, δ, of 0.0383 mm/s (2.3 mm/min). Depending on the size of the region of interest of the images, data acquisition ranges from 5 to 10 points per second. Measurements of crack advance are determined post-test by manually locating the crack tip in each of the images. If the crack is not continuous, the forward-most point that the material is visibly cracked is taken as the crack tip. Attempts were made to automate the process; however, the crack tip was too subtle to be reliably identified using simple thresholding and the images were too similar to train a robust neural network.

Plots of representative raw load and crack length data are shown in Figs. 3.11 and 3.12, respectively. The raw load data include an offset for the weight of the aluminum arms, bolts, bushings, and bearings which is accounted for prior to subsequent data processing. The load increases smoothly until the crack begins to propagate. At that point, the load stays roughly constant while the crack propagates slowly near the Vero (stiff) to DM8530 (compliant) interface and drops sharply when the crack propagates rapidly across the DM8530 layer and into the next Vero layer where it is arrested and begins to propagate slowly again. An early experiment imaged the specimens without DIC speckle pattern and the results showing the locations of the crack arrest and slow propagation is shown in Fig. 3.13. The drops in load in Fig. 3.11 correspond with the crack length jumps in Fig. 3.12.

The vertical load, P_v, is scaled with the net thickness, t, of the specimen (thickness of the thinnest point, at the tip of the side notch). The vertical load per unit thickness is integrated against the vertical displacement of the stepper motor, δ_v, to find the area under the $P_v - \delta_v$ curve. The resulting energy per unit thickness, U/t, is used to determine the energy release rate.

A representative U/t is plotted against crack location in Fig. 3.14. The energy has a defined stair-step structure. The increasing part of the stair-step comes from the crack slowly advancing near the stiff to soft interface while the energy increases due

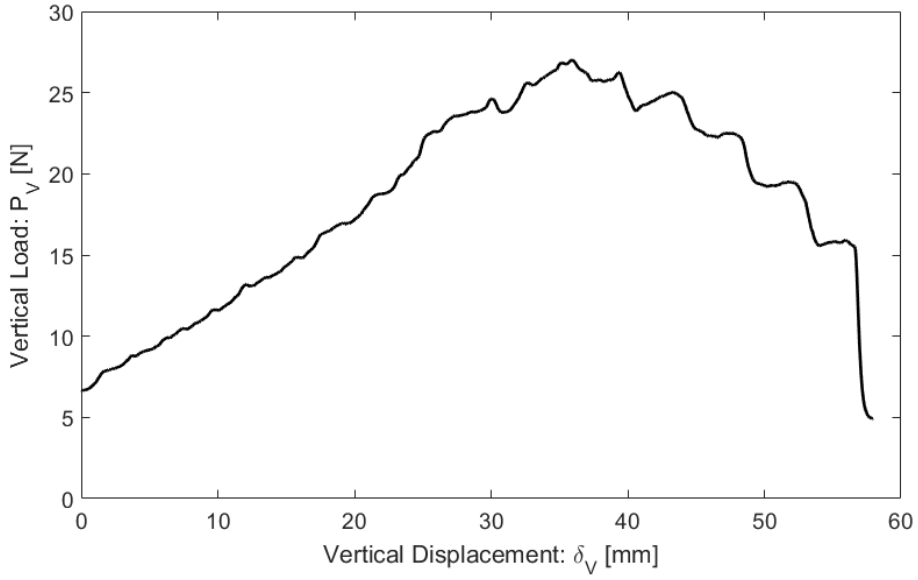

Figure 3.11: Representative raw load data versus vertical displacement of the rail (Specimen #S300-01). The 5 N offset is due to the weight of the fixture, which is accounted for prior to further data processing.

to loading the specimen. After the crack has propagated through the region with the elastic heterogeneity, the local resistance to fracture reduces abruptly and the crack is rapidly driven forward through the adjacent soft and stiff layers, forming the horizontal part of the stair step. In order to calculate the critical energy release rate, $G_c = dU/da$, the 10-90% rise time for each stair step is considered. The final stair step is discarded due to crack propagation out of the field of view, therefore it is not possible to measure crack extension for the full stair step. Using a linear fit, the slope of each step is determined for all specimens. The data are plotted to determine outliers, as in Fig. 3.15. All results are shown in Table 3.2 with the outliers highlighted in yellow. The outliers are associated with the crack not propagating smoothly (generally the first or second step) or with there being few points (< 10) available for the calculation. Tests numbered C300-01, S300-02 and S30-01 ruptured early in the test. The means are calculated for each group of specimens, excluding all of the identified outliers, and are shown in Table 3.3.

A Mann Whitney U[2] test is performed on the distributions to determine the significance of the results. The U test is selected because the results are not normally

[2] A t-test is not applicable because the samples are not normally distributed nor sufficiently large. A Mann Whitney U test (Wilcoxon Rank Sum Test) is an alternative test for when the samples are small and not normally distributed.

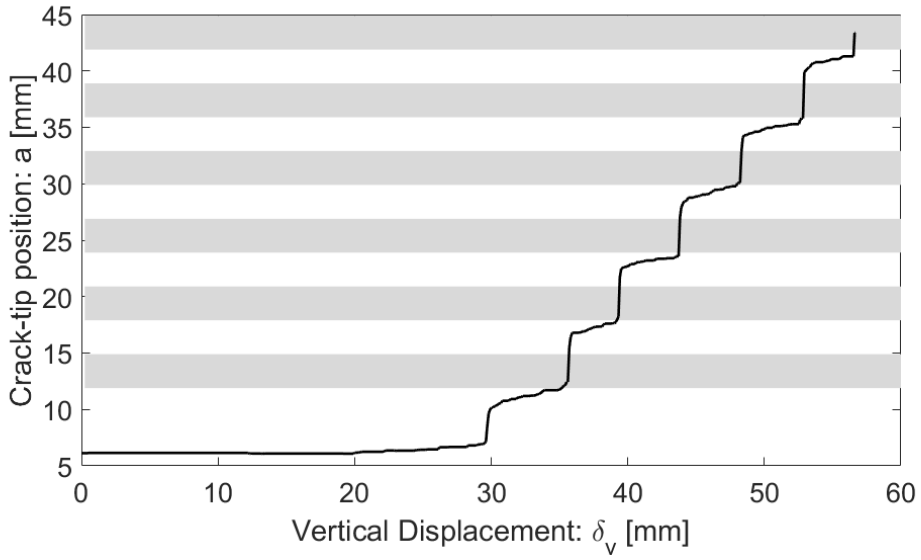

Figure 3.12: Crack length versus vertical displacement (Specimen #S300-01). Crack-tip position measured from the edge of the image frame. Shaded horizontal stripes are approximate locations of DM8530 (compliant) layers determined from image registration of the first image of the test.

distributed so Student's t test may be inaccurate [76]. The null hypothesis (that the samples come from populations with identical medians) is rejected at a 85% (α=0.1269) and 97.5% (α=0.0246) confidence interval for the 1.5 mm and 3.0 mm stripe specimens (excluding all outliers), respectively.

Using digital image correlation, plots of strain in the y-direction (normal to the crack) for selected points of a step are shown for specimens with and without a spine in Figs. 3.16 and 3.17, respectively. The strain plots for both specimens are very similar at points 1 and 2, with both demonstrating a lobed strain distribution at the crack tip. However, at points 3 and 4 the specimen without the spine sharpens the lobe intersection at the crack tip while the specimen with a spine sees the lobes merge.

3.4 Discussion

The theory, computational and experimental results indicate that fracture toughness due to a crack propagating across an interface is affected by both the redistribution of stresses at the crack tip due to the elastic contrast and by renucleating at the interface due to vanishing stress intensity. The agreement between the renucleation theory of Tanné et al. and the computational results indicates that renucleation in layered materials is necessary and that this material architecture can be used to study it.

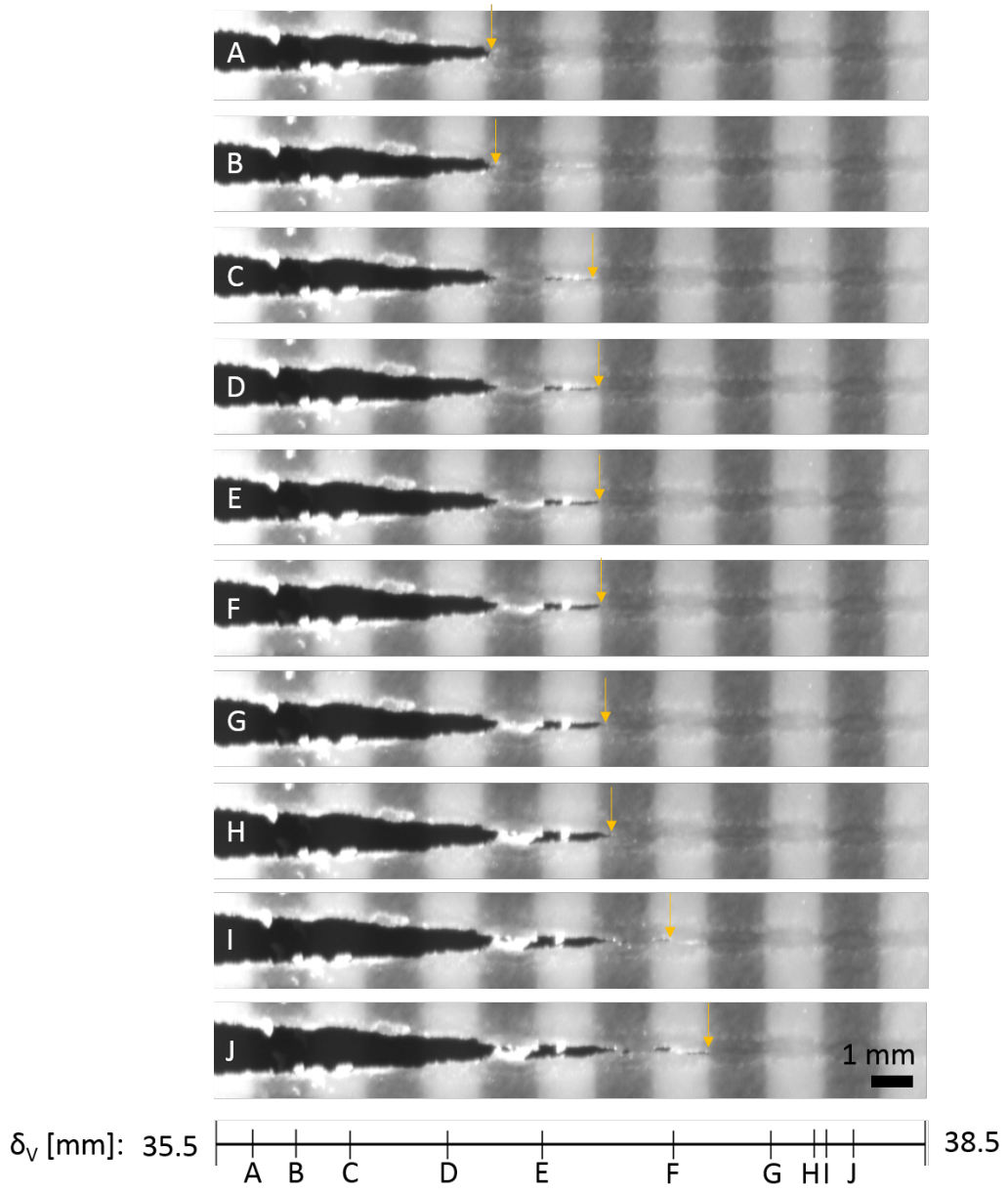

Figure 3.13: Crack propagating through layered stripe specimen. The forward-most point of the crack is marked with an arrow and considered as the crack tip.

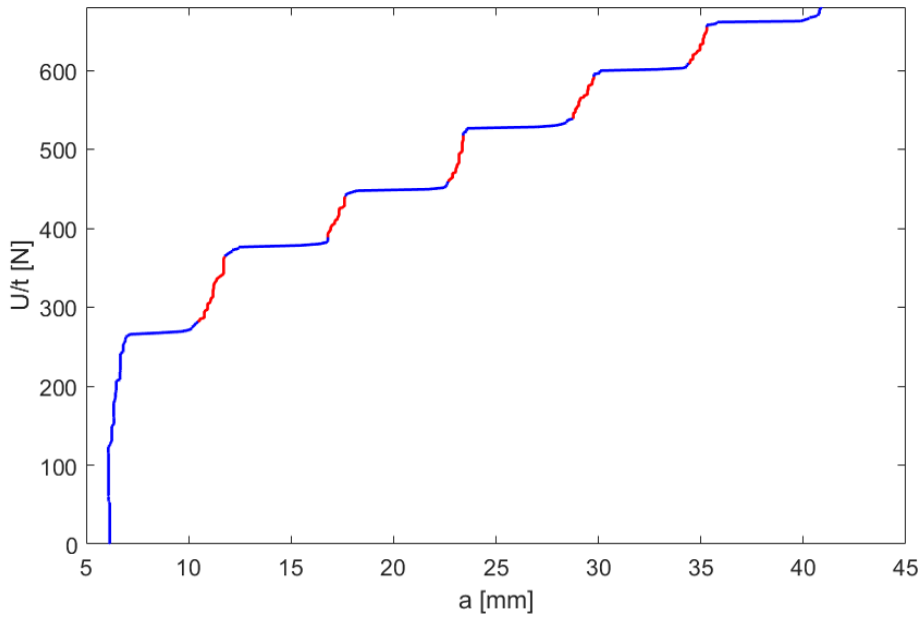

Figure 3.14: Representative result of integrating the vertical load versus vertical displacement (Specimen #S300-01). 10-90% rise is highlighted in red [29].

For the architecture with the spine (the only toughening is due to elastic heterogeneity), the theoretical consideration that the effective toughness of a specimen with sufficiently large layers is equal to the larger ratio: $\max\{G_c^c \frac{\langle E \rangle}{E^c}, G_c^s \frac{\langle E \rangle}{E^s}\}$ (Eq. (3.9)) was confirmed through computational modeling. The value predicted by Eq. (3.9), 40.1 kJ/mm, agrees well with the experimentally observed value of 44.2 kJ/mm.

For the architecture without the spine (the toughening is due to both elastic heterogeneity and renucleation), the theoretical consideration based on the work of Tanné et al, Eq. (3.16) was in good agreement with the computational modeling. The value predicted by this method, 57.5 kJ/mm, agrees well with the experimentally observed value of 56.3 kJ/mm. Additionally, from the computational modeling in both cases, it was expected to see the effective toughness increase with layer width, which was in agreement with the experimental observations in Table 3.3.

The simulations, theory, and experiments described in this chapter demonstrate that both elastic contrast and crack renucleation at interfaces contribute to toughening behavior in layered materials. It is important to note that this result depends on the bi-material interface being sufficiently strong to allow crack propagation into the adjacent material, rather than the crack deflecting and propagating along the interface. Additionally, the work presented in chapter shows that toughening requires a minimum size of the heterogeneity. If the heterogeneities are too small, full toughening

Table 3.2: Summary of all measured values of dU/da for the fracture specimens. Outliers highlighted in yellow

Specimen Name (Test Date)	#	dU/da measurements for individul stair steps												
C150	1	34.4	17.1	21.9	39.3	29.7	31.1	49.0	12.3	37.4	15.4	12.3		
7/17/2017	2	45.2	21.4	17.3	26.1	23.8	21.5	30.2	12.9	28.5	16.7	12.5		
	3	53.8	24.7	16.5	48.6	44.4	36.9	19.5	31.4	12.8	23.8			
	4	74.7	22.7	25.3	16.7	25.7	25.3	48.3	34.7	40.9	29.6	19.0		
	5	30.2	22.4	48.0	66.3	81.9	22.8	15.7	16.8	27.3			both 7 data points	
C300	1	49.3												
7/17/2017	2	73.5	34.8	49.5	30.7	29.7								
	3	55.2	39.5	70.7	34.4	30.7								
	4	52.6	40.5	42.0	45.4	28.3								
	5	95.4	25.5	57.3	35.4	60.5								
S150	1	56.7	32.5	18.2	13.0	22.9	12.1	20.7	35.1	24.3	13.4	27.1		
7/17/2017	2	61.4	39.2	43.5	59.1	35.4	15.4	35.9	20.9	27.4	28.4	24.2		
	3	39.6	40.7	20.1	30.6	29.9	28.9	10.2	22.2	27.3	10.0	20.8		
	4	45.7	37.1	28.3	24.1	37.9	70.0	13.7	45.1	30.6	16.5		> 10 data points	
	5	30.7	40.9	52.6	23.5	24.5	25.4	21.7	23.3	22.9	27.8			
S15	1	110.6	56.2	34.4	37.2	49.6	32.8	30.9						
4/12/2017	2	194.8												
	3	79.1	87.1	34.5	36.3	41.9	38.8	26.4	20.8					
S300	1	63.6	52.0	78.5	44.8	48.5								
7/17/2017	2	85.8												
	3	76.5	44.6	45.5	53.7	44.6								
	4	118.2	66.7	57.6	53.6									
	5	92.1	91.7	47.6	60.6	50.3								
S30	1	98.3	56.8											
4/12/2017	2	40.4	37.0	38.3	21.8	25.6								
	3	68.6	39.0	50.5	51.1									

Table 3.3: Experimental results for the energy release rate, G_c for the four architectures considered with values predicted by Eq. (3.10) and (3.16) assuming large layer width [kJ/m^2]

.

Layer Size [mm]	1.5	3.0	Theory
w/ Spine	27.3	44.3	40.1
w/o Spine	30.6	56.2	57.5

enhancement is not achieved; once the heterogeneities reach a sufficiently large size, there is no further enhancement.

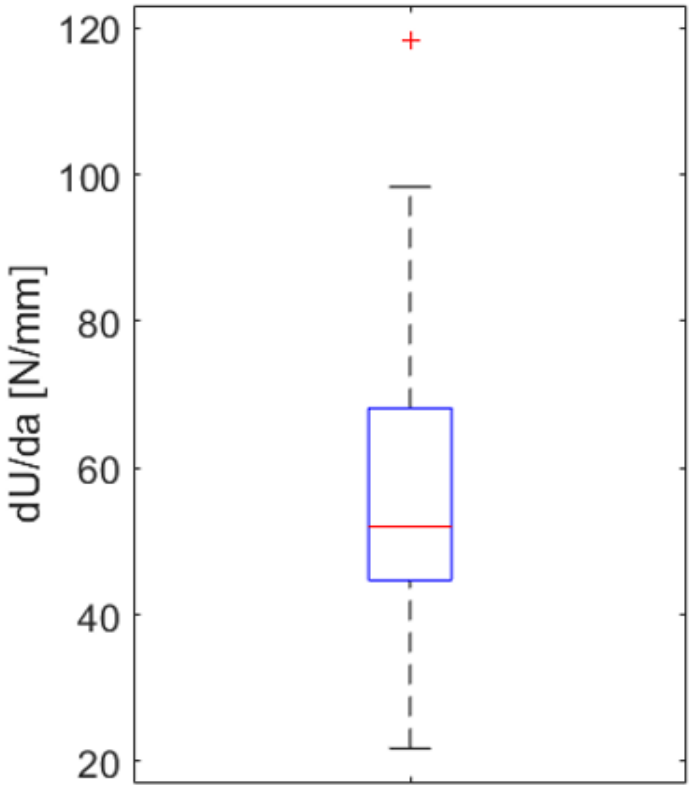

Figure 3.15: Box-and-whiskers distribution of slopes for 3.00 mm stripe specimens. The median is indicated by the horizontal red line. The outlier is identified by the red cross [29].

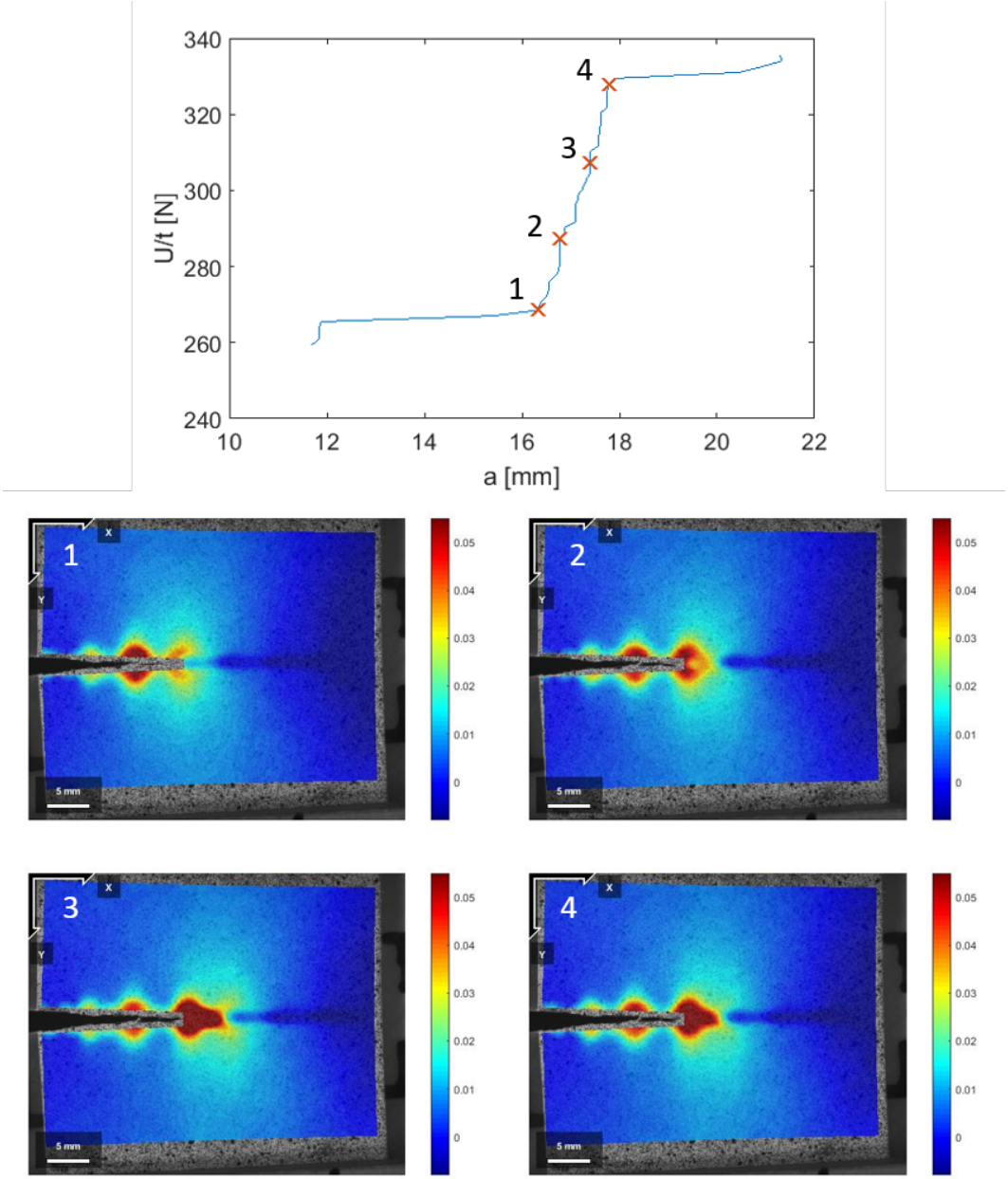

Figure 3.16: Full-field map of the strain component ϵ_{yy} at selected loading points for specimen with spine (Specimen C300-03).

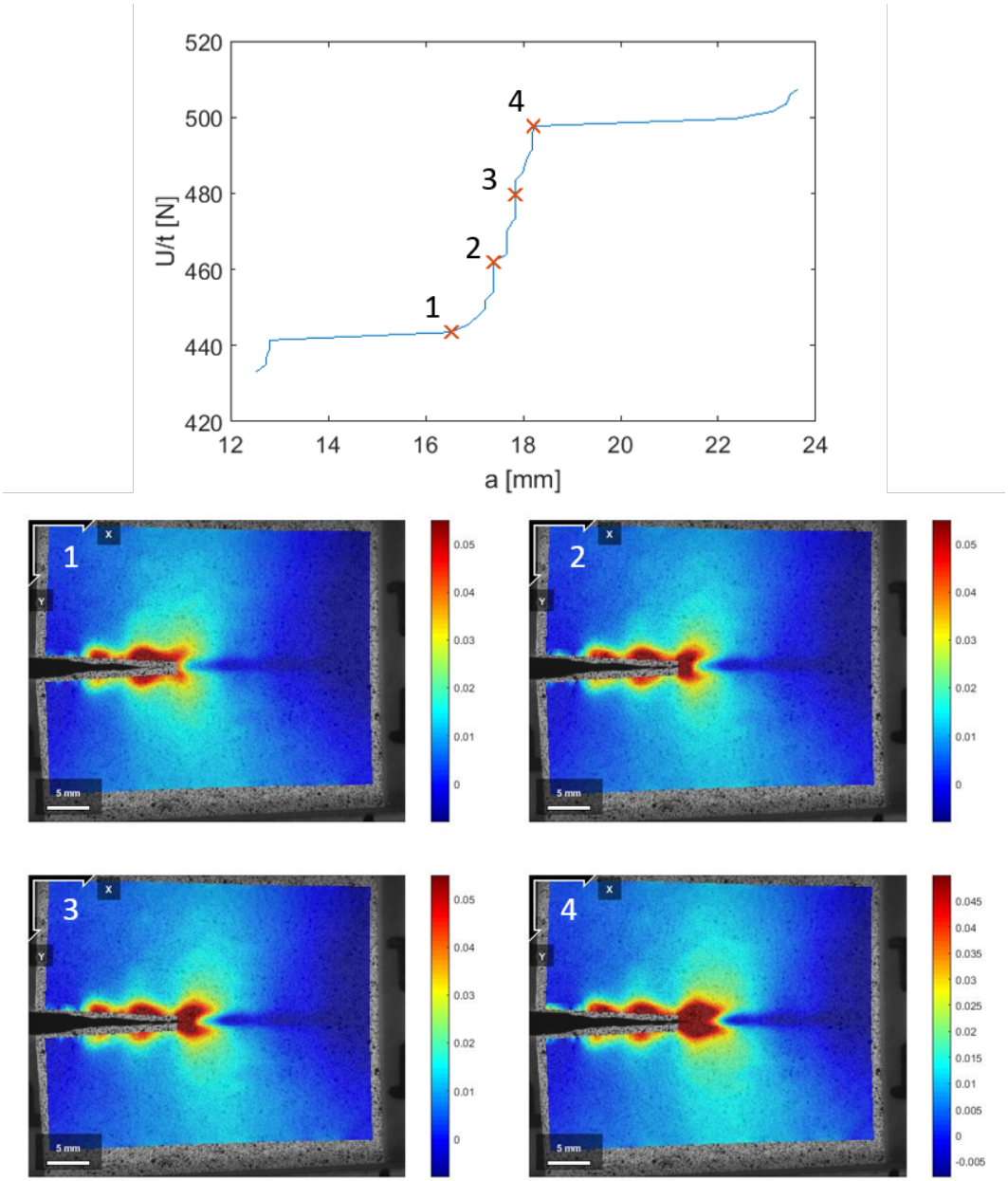

Figure 3.17: Full-field map of the strain component ϵ_{yy} at selected loading points for specimen without spine (Specimen S300-03).

Chapter 4

PROCESS ZONE SMOOTHING OF HETEROGENEOUS EFFECTS IN TAPE PEELING

4.1 Introduction

In the fracture of 2D- and 3D-materials, it is well understood that elastic contrasts in composite materials affect crack propagation [36, 77]. In tape or film peeling, often studied as a one-dimensional approximation to fracture, either an elastic contrast or a difference in thickness can be used to introduce a bending stiffness heterogeneity that has a similar effect in influencing the force required to advance the peel front [8, 9, 39, 78]. It has been shown that substantial enhancement in peel force can be achieved by introducing elastic heterogeneities in the tape. Kendall showed that in order for the peel front to pass through a contrast in bending stiffness, the shape of the peeling profile changes dramatically; the bending energy required to change the peeling profile is what causes variation in the overall peeling force [8]. Furthermore, he proposed design criteria for peel resistant composites. He also showed that for toughness enhancement to occur, the stiff heterogeneities should be on the order of the size of the stress field in the stiffened region and spaced at a minimum on the order of the size of the stress field in the unstiffened (compliant) region. If the stiffened region is not sufficiently large, it will fail to pin the crack. If the spacing is not sufficient, the crack will not decelerate enough to be pinned by the next stiff interface. Xia et al. used numerical studies and experiments on nominally brittle adhesive systems to show that at a step-up in thickness in laminate peeling with sufficiently large heterogeneities, the amount of peel force increases as the cube of the thickness, and can be predicted based on Euler-Bernoulli beam theory [39, 78]. They also showed that the amount of toughening resulting from stiffening depends strongly on the size and spacing of the heterogeneities with respect to the characteristic length. The characteristic length scale of a tape subjected to bending during peeling is $\lambda = \sqrt{D_e/2G}$, where D_e is characteristic bending stiffness of the periodic tape and G the adhesive energy.

Past experiments and theories have been developed assuming brittle peeling; that is, that the cohesive zone at the peel front is negligible. The work presented in this chapter studies peeling of a heterogeneous pressure sensitive tape with a substantial

cohesive zone. The present study aims to understand the role of the cohesive zone on the enhancement on the peel force during the peeling of elastically heterogeneous tapes. This chapter begins with experiments on a heterogeneous pressure sensitive tape. Simulations performing a parametric study of the adhesive strength, G, and cohesive zone size follow.

4.2 Experimental

Materials and Method

Peel experiments of a pressure sensitive tape (3M 810 Scotch™ tape, acetate backing with acrylic adhesive) adhered to a substrate are performed using the setup shown in Fig. 4.1a. The 3M 810 tape has a Young's modulus (E) of 1.65 GPa and has an adhesive energy (G) for bonding to glass of 34.5 N/m when pulled at 0.01 mm/s [79]. The width and the thickness of the tape are 19.05 mm and 0.0635 mm, respectively. The primary substrate considered is glass; sand-blasted acrylic, Teflon, and 1200-grit sandpaper are also examined as substrates. Prior to the adhesion of the tape, the glass, acrylic, and Teflon substrates are cleaned by wiping with an ethanol wetted Kimwipe followed by a dry Kimwipe. The substrate is then allowed to dry for one to two minutes. In the case of the 1200-grit sandpaper, it is adhered to a rigid substrate and inspected for grit integrity and replaced if degradation is observed. The base layer of tape is applied to the substrate and smoothed using a squeegee. The tape is long enough that it can be clamped in the loading grip. The initial length of the tape from the substrate to the grip is long enough so that the change in peel angle during peeling is minimized. Heterogeneities are applied to the base layer by the following process: if the heterogeneity is to be more than one layer, the heterogeneities are laid up by applying the first layer to wax paper and smoothing subsequent layers on top of the first layer until the desired layer count is reached. Strips of the tape 1-5 mm in width, but much longer than the width of tape are cut from the built-up tape. The strip is then removed from the wax paper and applied to the base layer spaced 4-5 mm apart.

Following Xia et al., the sufficient size for the stiff heterogeneities is [39]:

$$\lambda = \sqrt{\frac{D}{2G}}, \tag{4.1}$$

where $D = (\sum_{m=1}^{m=2} \chi^{(m)}/D^{(m)})^{-1}$, and $\chi^{(m)}$ is the length fraction and $D^{(m)}$ is the bending stiffness of each stiffness heterogeneity, m. The minimum heterogeneity size and spacing (for equal length fraction heterogeneities) is evaluated to be $\lambda = 0.78$

mm for the 3M 810 tape peeling from glass substrate[1].

A 10-15 mm length of adhered tape is left without heterogeneities before the first heterogeneity. The average value of the peel force in this region is used to normalize the results. The heterogeneity is trimmed to the width of the tape and smoothed using a squeegee. An image of the tape with heterogeneities is shown in Fig. 4.1b. The tape is left a minimum of 20 minutes before the beginning of the peel test to ensure consistency of adhesion [79]. The tape is then installed in the loading grip, with a 20 cm peel arm to reduce the effects of the change in peel angle over the course of the test 5 cm peel distance.

The loading grip is pulled up at the rate of 0.05 mm/s using a PI 410.2S stepper motor and PI Mercury C663 controller (Physik Instrumente, Irvine, CA). The peel force is measured during the test using an LC101-50 load cell (Omega, Norwalk, CT), DP41-BA-C24 strain meter (Omega, Norwalk, CT) and NI USB-6251 DAQ box (National Instruments, Austin, TX). A Navitar Inc (Rochester, NY) microscope lens (1-6010 C-mount coupler, 1-6030 2X Standard Adapter, 1-60135 6.5X Zoom 12 mm Fine Focus) is attached to a μEye EO-1312m USB camera (Edmund Optics, Barrington, NJ) and images are taken while the peel front is in the field of view. The images and load cell readings are collected and recorded using a LabVIEW Virtual Instrument (National Instruments, Austin, TX).

Results

Figures 4.2 through 4.6 show the results for the heterogeneous peel experiments. There are five phases of the load evolution during the experiment:

1. The load reaches a steady state (after an initial transient phase) while the tape is being pulled through the homogeneous region;

2. As the peel front edge of the tape approaches the heterogeneity, the load increases and peaks when the peel front reaches the step up in the heterogeneity;

3. After propagating through the front side of the heterogeneity (step up side), the tape returns to the steady state peel force (1) in the region of increased (multi-layer) thickness heterogeneity;

[1]The adhesion strength of Scotch™ tape depends on the peel speed. A peel speed of 0.05 mm/s was used in the following experiments and the associated adhesion strength was found to be 50 N/m.

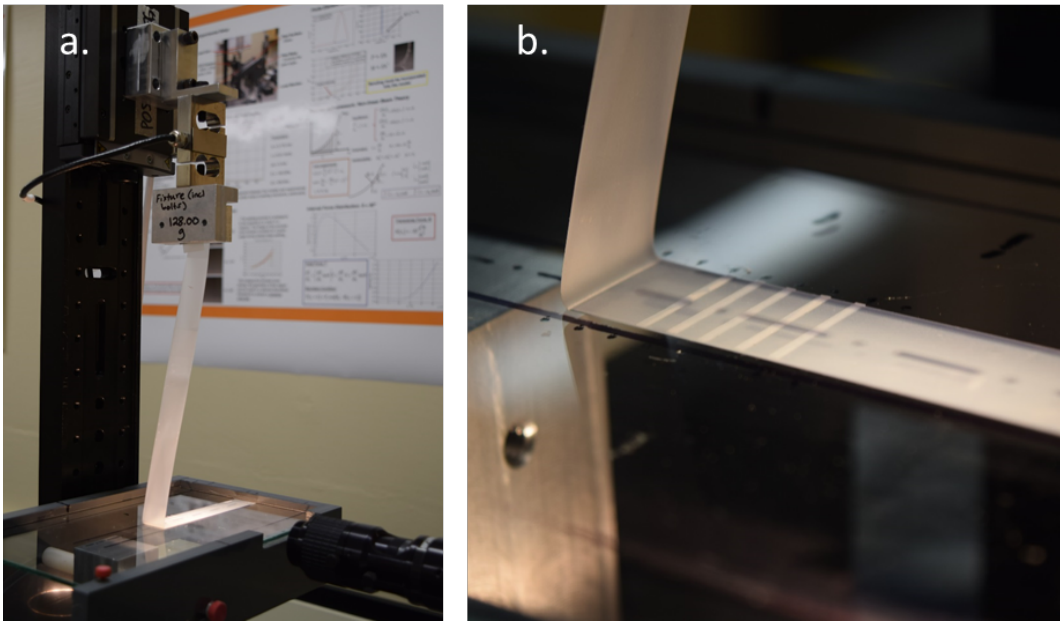

Figure 4.1: a. Tape peeling experiment configuration; b. Close up view of the heterogeneities.

4. At the back side of the heterogeneity (step down side), the load experiences an abrupt drop to a value below the steady state value of peel force associated with peeling of a homogeneous tape, (1);

5. The peel force recovers from the drop and reaches the steady state value associated with homogeneous peeling, (1).

These phases are present in the load plots for all the substrate materials considered here. Figure 4.2 shows the results for peeling 3M 810 Scotch™ tape with 1-, 2- and 3- layer heterogeneities from a glass substrate; the normalized peak peel loads range from 1.5-2.1 times the homogeneous peel force. These values are substantially lower than the 8, 27 and 64 times predicted by Euler-Bernoulli beam theory [39]. The normalized valley peel loads are 0.3-0.5 times the homogeneous peel force. The normalized peaks and valleys do not appear to be greatly affected by the number of layers of tape making up the heterogeneity; that is, the amount of load increase appears to saturate.

Using the relation between the adhesive energy, G, and peel force, P:

$$P = \frac{G}{1 - cos(\theta)}, \tag{4.2}$$

the effective G can be varied by varying P. This is achieved by using different substrates with the same tape. Figure 4.3 shows the results of these experiments.

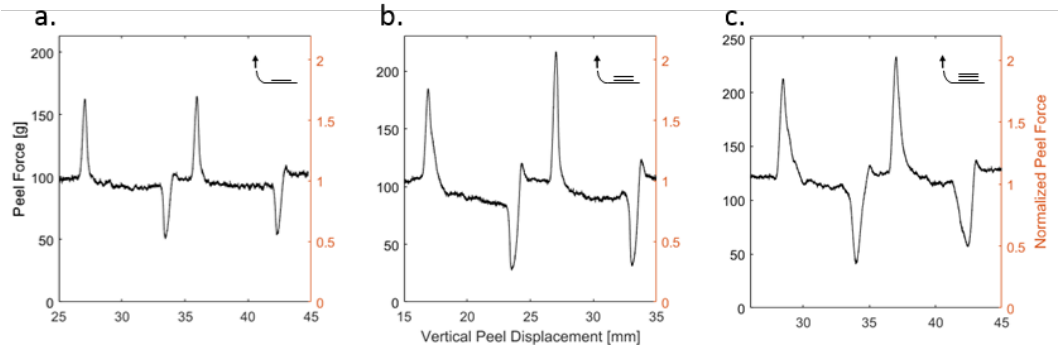

Figure 4.2: Results for peeling Scotch™ tape with heterogeneities from a glass substrate. a. 1- b. 2- and c. 3- layer heterogeneities (see inset). Heterogeneities are 6 mm wide spaced 2 mm apart.

While sandpaper and Teflon have slightly lower peel forces (slightly lower effective G) than glass, the normalized peak values are slightly higher than those of glass. The sand-blasted acrylic has slightly higher peel force and the normalized peak appears to be further suppressed.

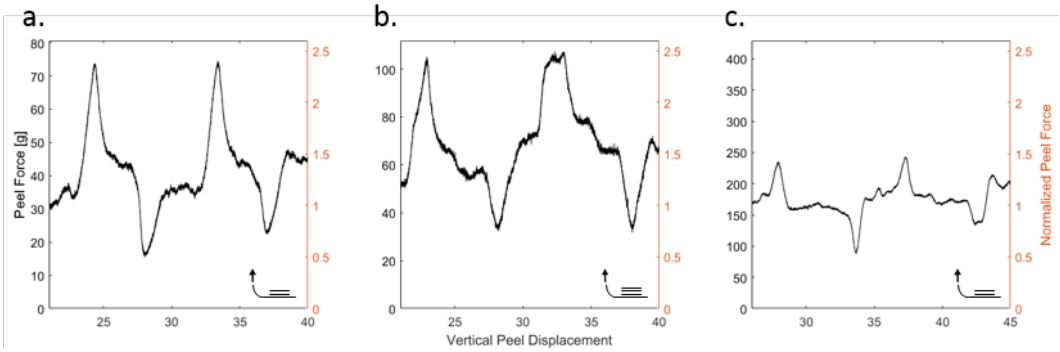

Figure 4.3: Results of peeling Scotch™ tape with heterogeneities from various substrates; a. 1200 grit sandpaper (2 layers, 5 mm long spaced 4 mm apart); b. Teflon (3 layers, 6 mm long spaced 3 mm apart); c. sand-blasted acrylic (2 layers, 5 mm long spaced 2 mm apart, 0.025 mm/s peel velocity).

Additional peeling experiments with the 3M 810 pressure sensitive Scotch™ tape from a glass substrate were performed to study the effect of very narrow heterogeneities. Figure 4.4 shows the results of a test with 1 mm wide heterogeneities (2-layers, 6 mm spacing). The normalized peak and valley values are roughly the same as in the tests with wider heterogeneities (see Fig. 4.2 for 6 mm wide heterogeneities). The only major difference is the absence of a steady state region, which can be attributed to the small width of the heterogeneities.

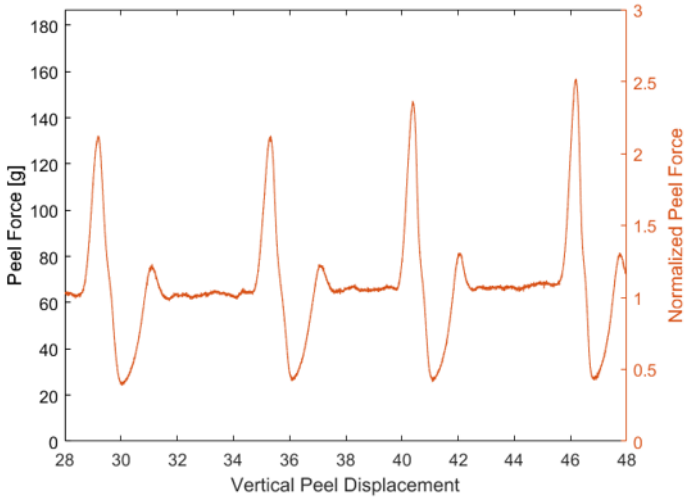

Figure 4.4: Peel force versus vertical displacement for peeling adhesive tape with 2-layer heterogeneities (1 mm wide, 6 mm spacing) from a glass substrate.

Occasionally, for narrow heterogeneities, the heterogeneity deadhered from the base layer. Figure 4.5 shows an example of this behavior. In image A the tape approaches the heterogeneity at the steady-state peel force. The load begins to increase at B, but at C the adhesive bonding of the heterogeneity to the base layer fails, resulting in a visible gap between the base layer and the heterogeneity. The load drops at D as it returns to a steady state at E and F without exhibiting a load drop to a valley. The deadhesion of the heterogeneity is so pronounced when it occurs that the absence of a visible gap in the photographic records of other tests gives confidence that this is not the primary mechanism of peak load suppression.

In order to determine whether the suppression of the highest value of the peak was due to a similar deadhesion event at the front of the heterogeneity, an experiment is performed with packing tape (3M 142) as the heterogeneity and with 3M 810 as the base uniform layer. Figure 4.6 shows the normalized (with respect to the homogeneous single layer peel force) peel variation and the evolution of the radius of curvature near the peel front. The heterogeneities are two layers thick; since 3M 142 (0.0787 mm [80]) is thicker than 3M 810 (0.0635 mm [81]), the total thickness is slightly more than 3 times the base layer thickness. The normalized peak load is 2.65, which is substantially less than the 27 that would be predicted by the Euler-Bernoulli theory [39]. The tape is peeled from a glass substrate at 0.05 mm/s. The normalized minimum (valley) load is 0.35. The tape starts with a relatively small radius of curvature in the homogeneous region, A-B. When the tape approaches the

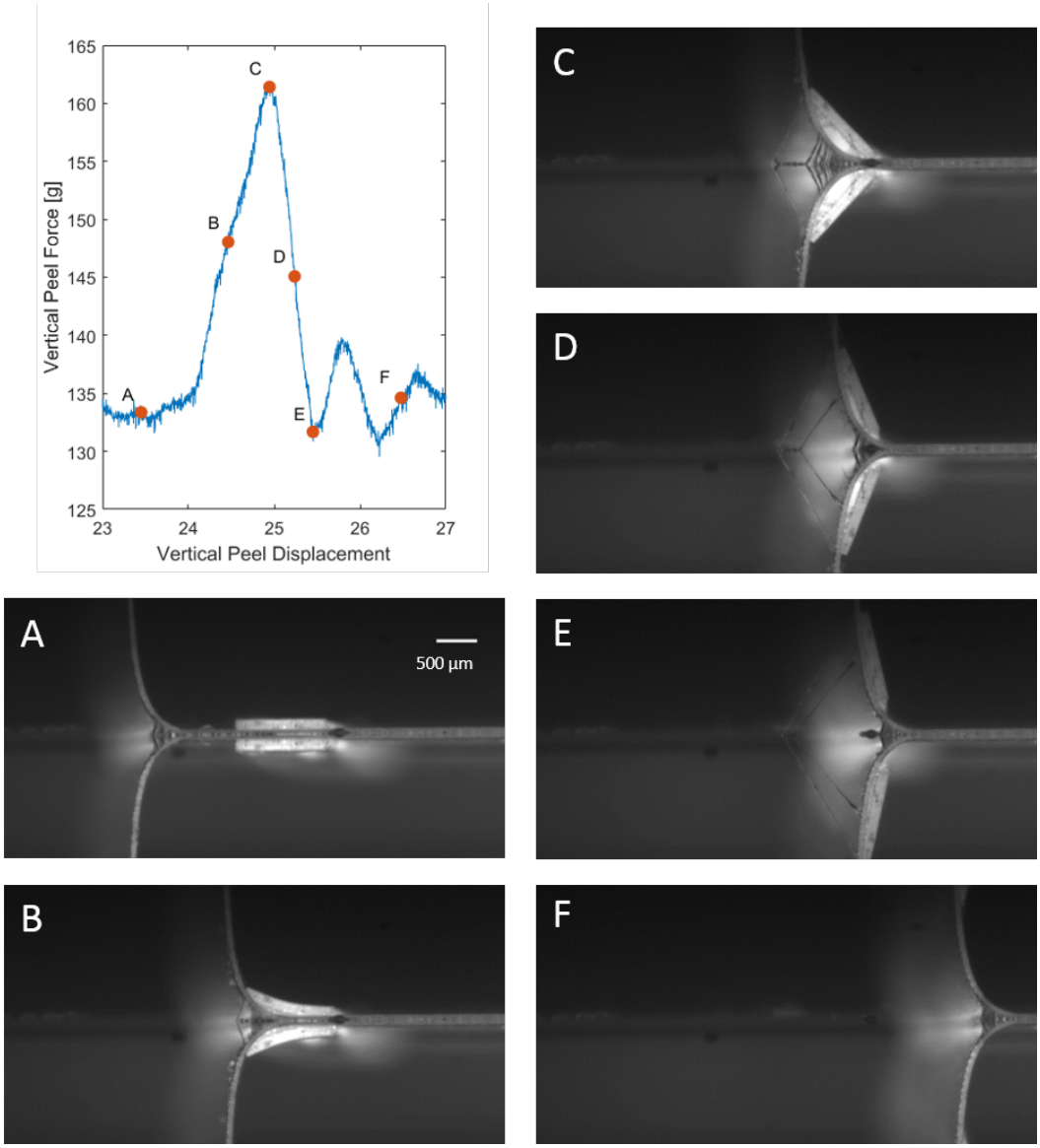

Figure 4.5: Peeling adhesive tape with 2-layer heterogeneities from a glass substrate. Peel force versus vertical displacement is plotted. The images A-F show the various stages of peeling and the cohesive zone.

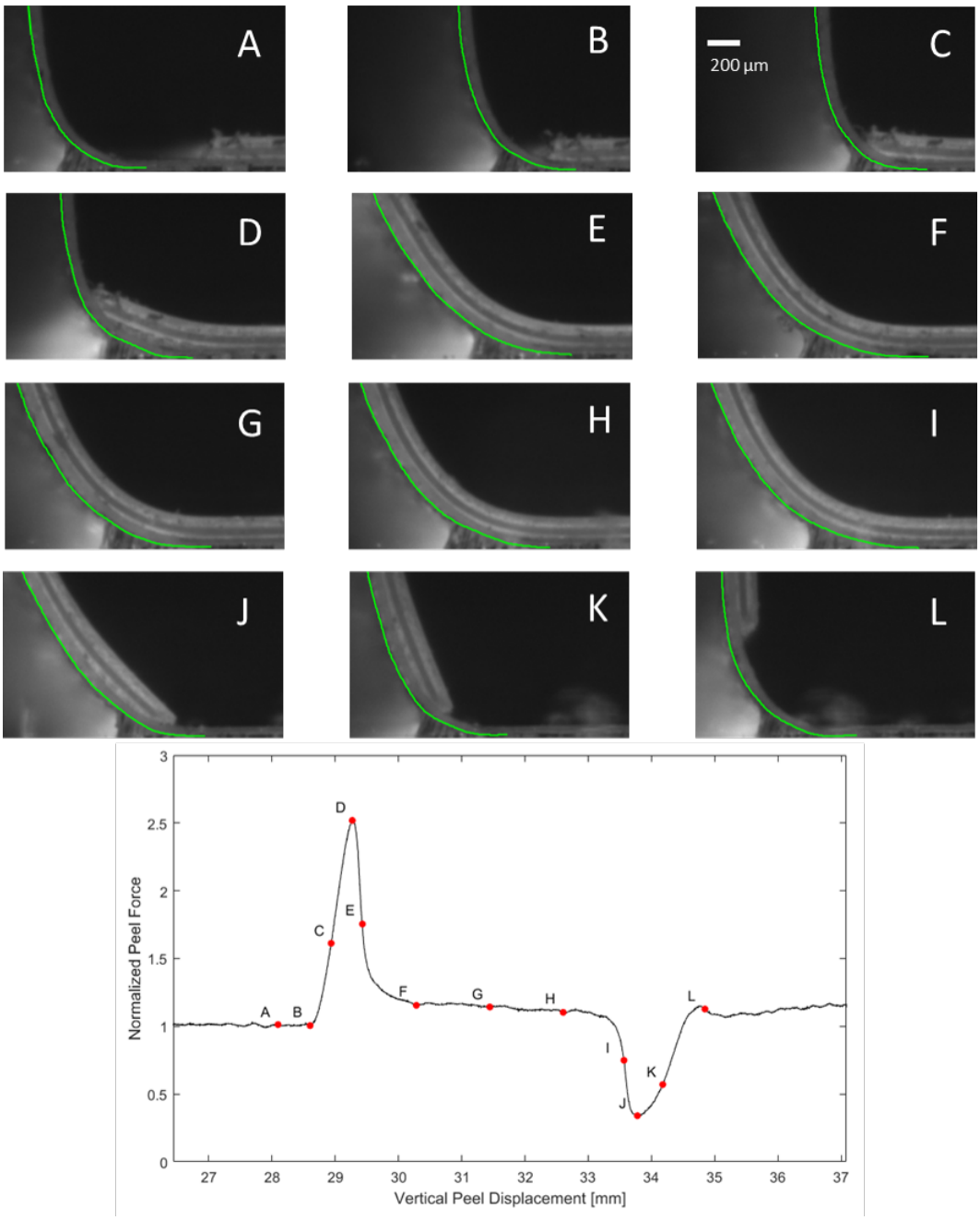

Figure 4.6: Images A-L show the various stages of peeling a heterogeneous tape with two layers of packing tape on a uniform layer of Scotch™ tape. Normalized peel force is plotted as a function of vertical displacement.

heterogeneity, the radius of curvature increases at C-E before becoming a steady state larger curvature at F-H. At the step down, I-K, the radius of curvature reduces back to the original radius of curvature at L. The width of the cohesive zone can also be observed to vary in these images. The cohesive zone in the beginning and end of this process, A-C and J-L, is narrower than in the middle, D-I. Also note that the peel front has begun to penetrate into the heterogeneous region as early as C, even though the peak load is reached at D. In fact, the cohesive zone in D can be seen to be entirely contained in the heterogeneous region.

In order to study the origin of the valley in the peel force (lowest value), it is interesting to consider the brittle (no cohesive zone) case. The numerical simulations and experimental observations presented by Xia et al. for heterogeneous film peeling experiments do not show the same 5 phases described above [39]. Rather, the load increases and reaches its maximum as the peel front approaches the step-up in film thickness, then the load rapidly decreases to its lowest value as the peel front propagates rapidly through the specimen until it is pinned by the next step-up in film thickness where the load begins to increase, again. Because there is no obvious valley (lowest value) in these experiments, it is desired to determine if the brittle case is unaffected by a step-down in film thickness (i.e., the peel front propagates at constant force through the step-down interface) or if the load does, in fact decrease abruptly, but this behavior is obscured by the peel front rapidly propagating all the way through the heterogeneity to the step-up of the next one.

Following the experiment preformed by Xia et al. [39], a single step-down heterogeneity was studied using PET film (0.1778 mm thick) adhered to epoxy (Devcon 2 Ton clear epoxy) and cured overnight, which approximates brittle peeling. The tape (2 cm wide) was formed by gluing a second layer of the same thickness of PET onto the base layer using a UV curable super glue. Each tape has only one thickness step-down discontinuity. The epoxy/PET tape was adhered to a substrate of acrylic which was secured in the peel test setup. The tape is pulled at 0.15 mm/s. A schematic of this experiment and representative results are shown in Fig. 4.7. At points A-C, the peel front propagates under a relatively steady state force. Between C-D, the crack rapidly propagates approximately 9 mm while the applied vertical displacement increased 0.72 mm; hence, the load decreases rapidly. Since the tape is very stiff and constrained at the peel front end and in the loading grip, a resultant compressive force is observed. The load remains low while slack is removed from the tape, D-E. Subsequently the crack begins to propagate and reaches a new steady

state, E-F. The rapidly decreasing load from C-D indicates that the brittle case is affected by the step down in film thickness, it is likely that the rapid crack propagation that follows the pinning results in slack in the system that must be removed, obscuring this phenomenon.

4.3 Simulation

Model

The ABAQUS/Standard finite element software package is used to simulate the peeling of heterogeneous adhesive tapes from a rigid substrate. The simulations are used to develop insights on the experimental observations described above. The 2D finite element model geometry is shown in Fig. 4.8. The model consists of two parts - the tape and the adhesive. The tape is 0.10 mm thick and it is 10 mm wide in the z-direction. Four-node plane strain elements are used (CPE4R); mesh size is 0.014 (thickness) by 0.5 mm (length). Material properties of the tape, Young's modulus and Poisson's ratio, are chosen to be, E = 1000 MPa and ν=0.35, respectively. The thickness of the cohesive (adhesive) layer is 0.001 mm. Two-dimensional cohesive elements are used (COH2D4) with element deletion with a uniform mesh size of 0.001 x 0.025 mm. The bottom of the tape and the top of the cohesive layer are connected using a tie constraint.

The cohesive behavior of the adhesive layer is modeled using the traction separation law, as shown in Fig. 4.9. The parameters which describe the traction separation law are T, E_i, and δ_f. T defines the load at which the cohesive elements begin to fail. δ_f defines the opening displacement at which the element fails. E_i is a penalty parameter that depends on the size of the elements, T, and the ratio of initiation of damage δ_0 to element failure δ_f. If E_i is too large, the simulation runs into numerical problems. However, if E_i is too small it introduces compliance into the system [82, 83]. The area under the traction-separation relation defined by these parameters is G_C, the adhesive or fracture energy of the tape. E_i is varied with T and δ_f to maintain constant ratio of initiation of damage δ_0 to failure δ_f at 4e-5.

The tape is loaded by applying a vertical displacement to Δ_y (Fig. 4.8). The bottom edge of the cohesive layer and the far right edge of the tape and cohesive layer are fixed in the x- and y- directions (clamped boundary conditions). An artificial viscosity coefficient of 0.001 and NLGEOM with a stabilization parameter of 1e-7 to 1e-9 are used in the simulations to assist convergence.

Simulations are performed for various values of G_C and δ_f to study how the tough-

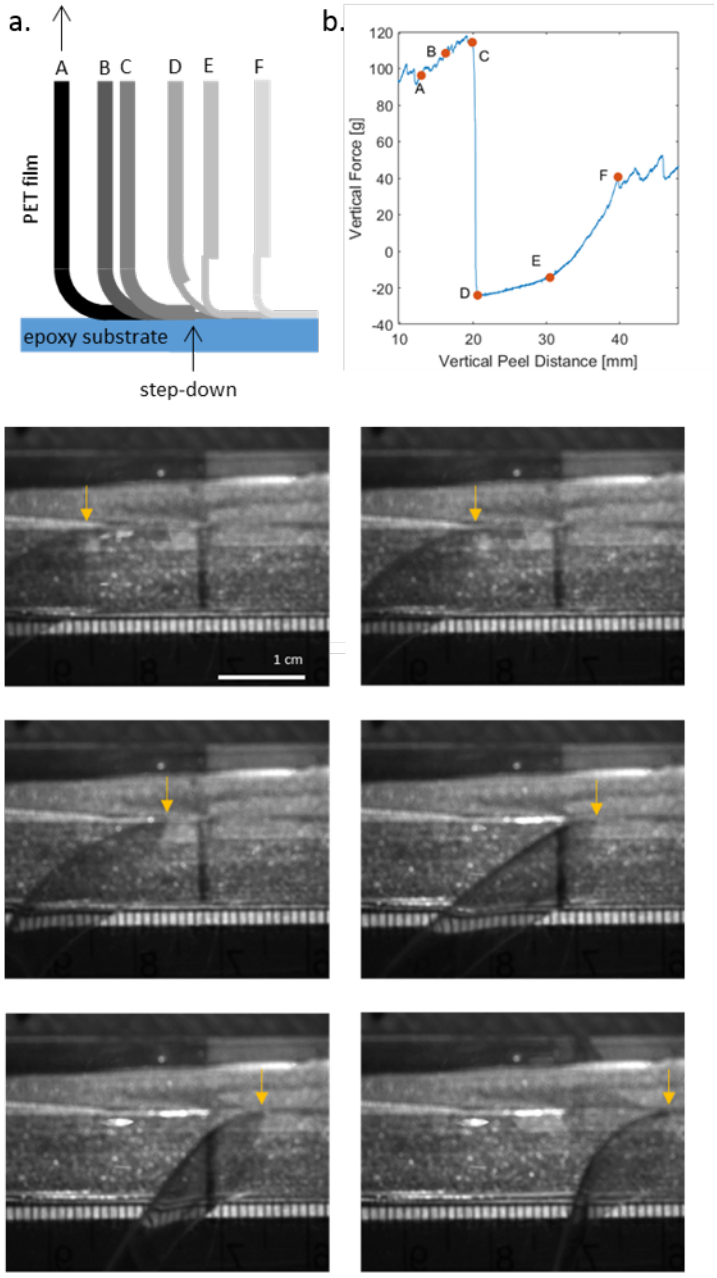

Figure 4.7: Peeling of a PET/epoxy tape from an acrylic substrate with a step down heterogeneity; a. Schematic of the tape; b. Peel force versus tape displacement. A-F show images of the peel front (marked with an arrow) corresponding to the loads in b.

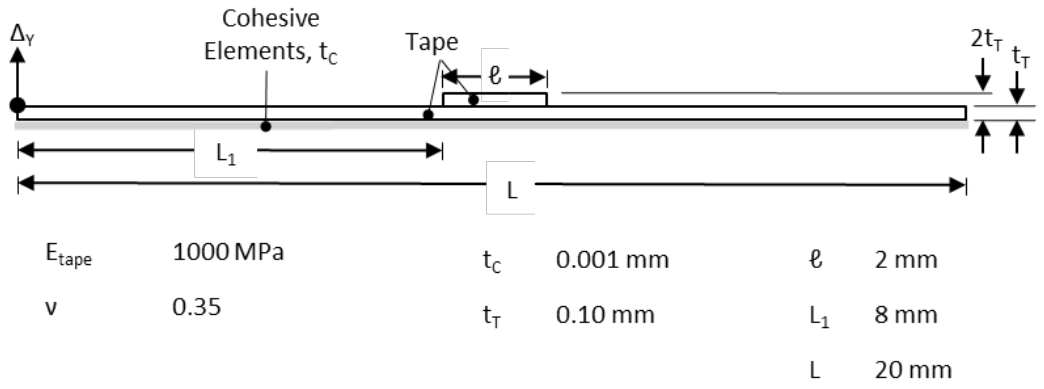

Figure 4.8: Geometry of the tape and simulation parameters for modeling the heterogeneous adhesive tape peeling from a rigid substrate.

Parameters	
T_u	$G_c = T_u\delta_f/2$ $E = T_u h_{eff}/\delta_0$
δ_f	
E_1, E_2, E_3	
Viscosity Coefficient	Stabilization Criteria

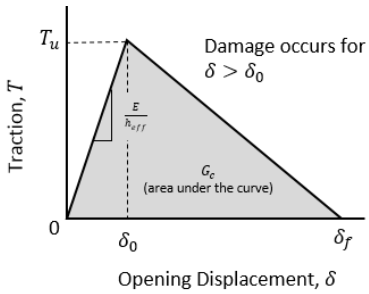

Figure 4.9: Traction separation laws and associated parameters used in ABAQUS simulations.

ness and the size of the cohesive zone affect the peak and valley loads in peeling heterogeneous tapes.

Results

Figures 4.10 and 4.11 show representative results of the tape peeling simulations. These simulations are for an adhesive energy, G_c = 25 N/m and δ_f = 0.1. Peel force and the cohesive zone size are plotted as a function of time (applied vertical displacement). The peel force reaches a steady state value in the homogeneous section of the tape as it approaches the heterogeneity at A in Fig. 4.10. The load begins to rise and the size of the cohesive zone increases as the crack front reaches the heterogeneity at B-C. The load peaks at C, and the cohesive zone has penetrated well into the heterogeneous region of the tape. The load begins to decrease and as the crack front passes through the heterogeneity at D the stress is more evenly distributed through the deadhered portion of the tape. The load decreases rapidly as the front reaches the other side of the heterogeneity at E-F and the load is once again

concentrated in the uniform thinner portion of the tape. The size of the cohesive zone returns to its original value. The tape reaches the same steady state value at F as in the beginning at A as the peel angle returns to 90 degrees.

Figure 4.11 shows additional detail of the variation of the cohesive zone size with peel force. The size of the cohesive zone takes two constant values during crack propagation associated with the thickness of the tape above the crack front. The size of the cohesive zone does not begin to increase until after the peel force has reached roughly half of its peak value. The peak load coincides with the maximum size of the cohesive zone.

The beginning of the cohesive zone size increase varies with the size of the cohesive zone. Figure 4.12a-d show selected load and cohesive zone size results for $\delta_f = 0.05$. The beginning of the cohesive zone size increase is marked with a dashed vertical line. In the simulations, as the crack approaches the heterogeneity it is pinned and the load begins to increase while the cohesive zone stays the same size or reduces slightly. At some load prior to the peak, the cohesive zone size begins to increase which coincides with the beginning of peel front penetration into the heterogeneous region. The location of this increase relative to the peak load varies with adhesive strength, G. In order to quantify this variation, the increase load is normalized by calculating the ratio of the load at the onset of increasing cohesive zone size to peak load:

$$\frac{P_{inc} - P_{hom}}{P_{peak} - P_{hom}}, \tag{4.3}$$

where P_{inc} is the peel force when the cohesive zone size begins to increase, P_{peak} is the peak peel force, and P_{hom} is the homogeneous peel force. Figure 4.12e plots onset of the increase in cohesive zone size versus the size of the cohesive zone in the initial homogeneous region. There is a correlation between the size of the initial cohesive zone and the onset of peel front penetration into the heterogeneous region; as the cohesive zone size increases, the peel front penetrates into the heterogeneous region at a proportionally lower load relative to the peak load. However, Fig. 4.12f plots onset of the increase in cohesive zone size versus the normalized peak force and does not demonstrate nearly as clear of a correlation between the two quantities. For individual values of adhesion strength, G, higher peak loads occur with later penetration into the heterogeneous region. However, the onset of the increase in cohesive zone size depends on the adhesion strength as well, and lower values of adhesion strength correspond with earlier onsets of penetration into the heterogeneous region.

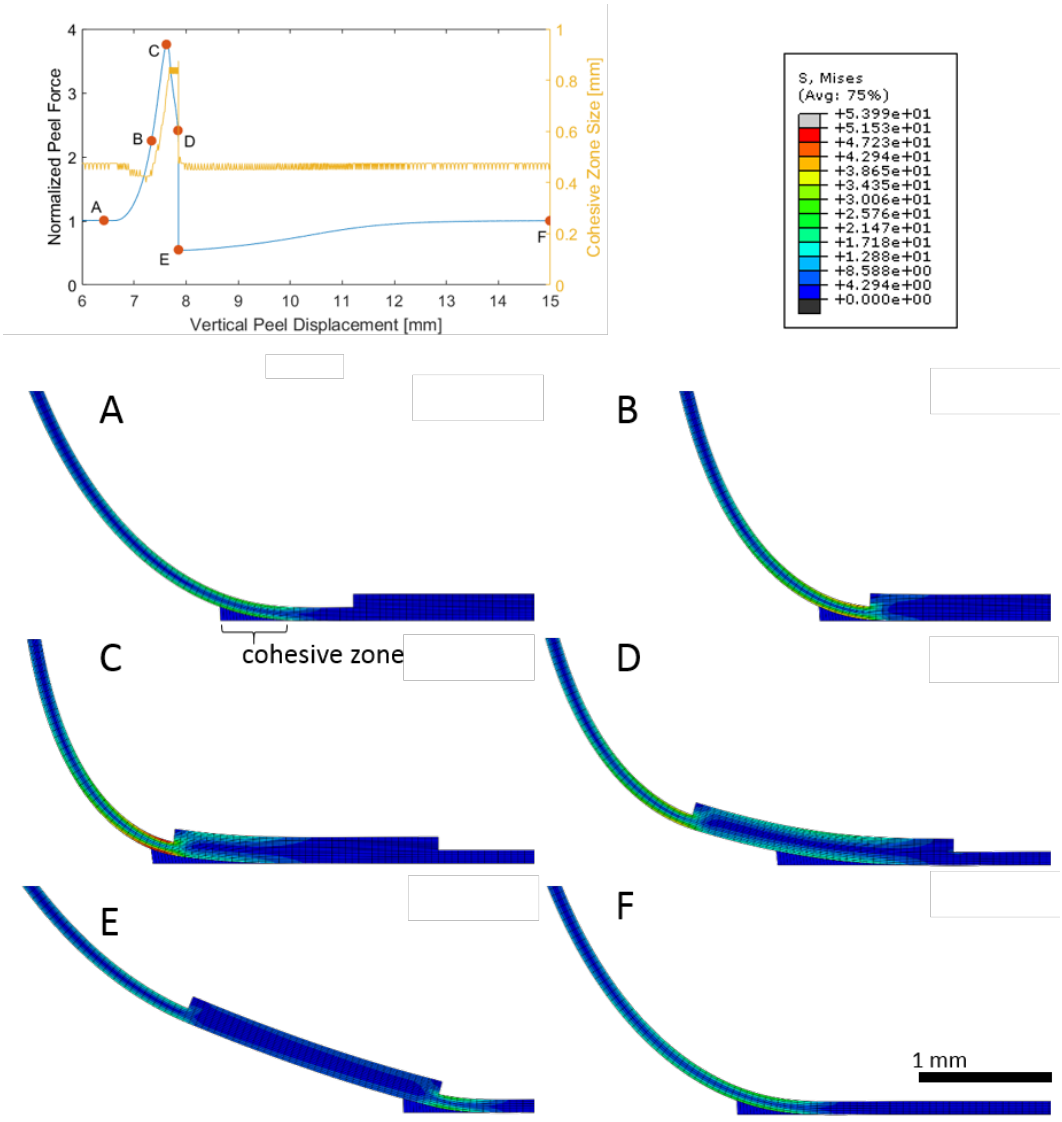

Figure 4.10: Normalized peel force and cohesive zone size are plotted as a function of time. Contour of plots of von Mises stress are plotted at various stages of the peeling process (A-F). Parametric values, G=25 N/m, δ_f = 0.1.

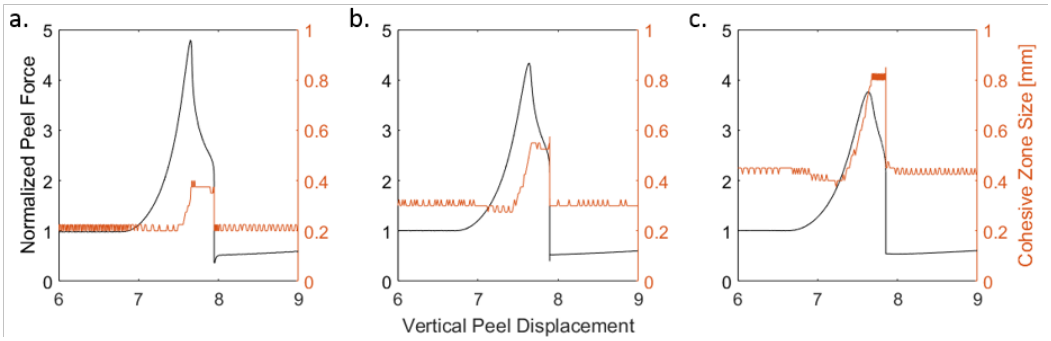

Figure 4.11: Normalized peel force and cohesive zone size are plotted as functions of time for G=25 N/m; a-c: δ_f = 0.025, 0.05, 0.10.

Figure 4.13 shows the normalized peak loads ($\frac{P_{peak}}{P_{hom}}$) versus normalized cohesive zone size and Fig. 4.14 shows the normalized valley loads ($\frac{P_{valley}}{P_{hom}}$) versus normalized cohesive zone size for all simulations. The cohesive zone size is normalized against λ calculated for the simulations according to Eq.4.1. Fig. 4.13 indicates that smaller normalized cohesive zone sizes are related to higher peak loads. Fig. 4.14 shows that smaller normalized cohesive zone size is related to lower normalized minimum (valley) loads.

4.4 Discussion

Experiments and simulations indicate that the cohesive zone works to smooth out the bending stiffness heterogeneity introduced by the step up in thickness, thereby smoothing out the toughening inducing discontinuity and reducing the toughening effect of the additional thickness in the heterogeneous region. The simulation results agreed with the experimental observation that the presence of a cohesive zone works to suppress the toughening effects of the elastic heterogeneity. Furthermore, the experimental (Figs. 4.2, 4.3) and simulation (Figs. 4.13 and 4.14) results agree in showing that the normalized peak load increases with decreasing adhesive energy G and that the normalized valley (minimum) force decreases with decreasing normalized cohesive zone size.

The peel front began to penetrate into the heterogeneous region prior to the peak load value being reached in both the experiments and the simulations. Studying the plots e and f in Fig. 4.12, later onset of penetration into the heterogeneous region is strongly correlated with smaller cohesive zone size and moderately correlated with higher normalized peak forces. However, from Fig. 4.12f, the strength of the adhesion, G, also affects the normalized peak force, with lower values of G

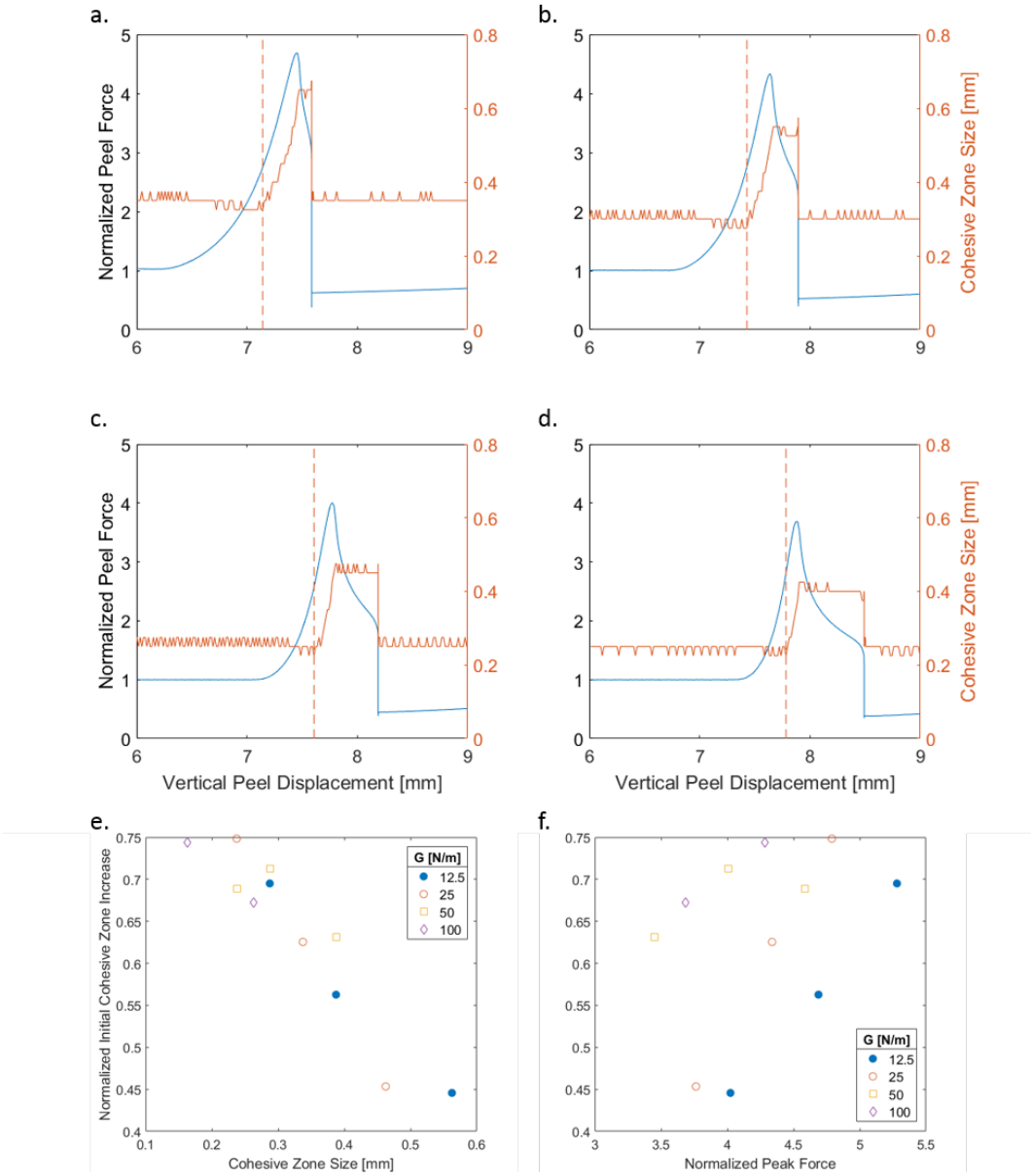

Figure 4.12: Normalized peel force and cohesive zone size are plotted as a function of time for δ_f = 0.05, a-d: G = 12.5, 25, 50, and 100 N/m. e. Initial cohesive zone increase (onset of penetration into the heterogeneous region) versus the lower cohesive zone size and f. versus normalized peak force.

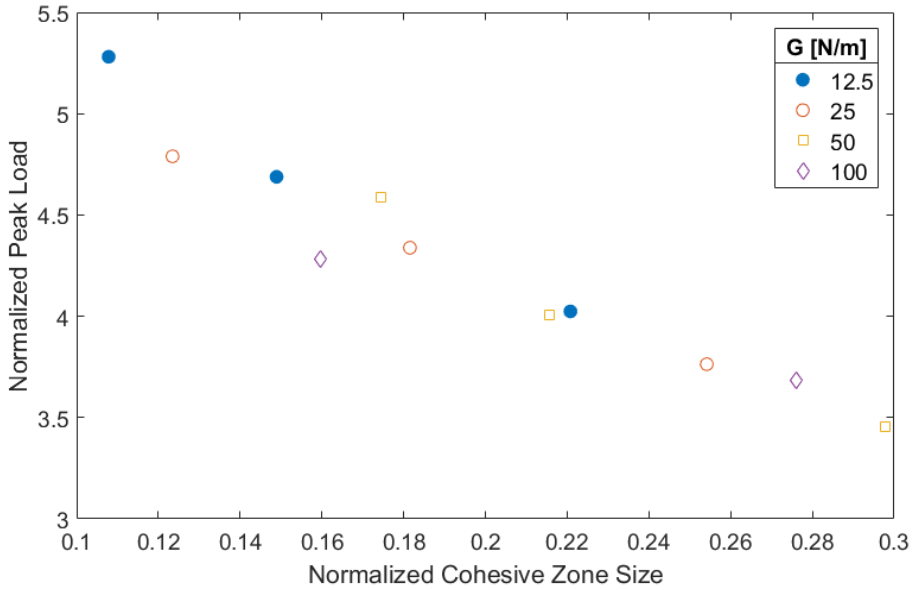

Figure 4.13: Normalized peak load versus normalized cohesive zone size.

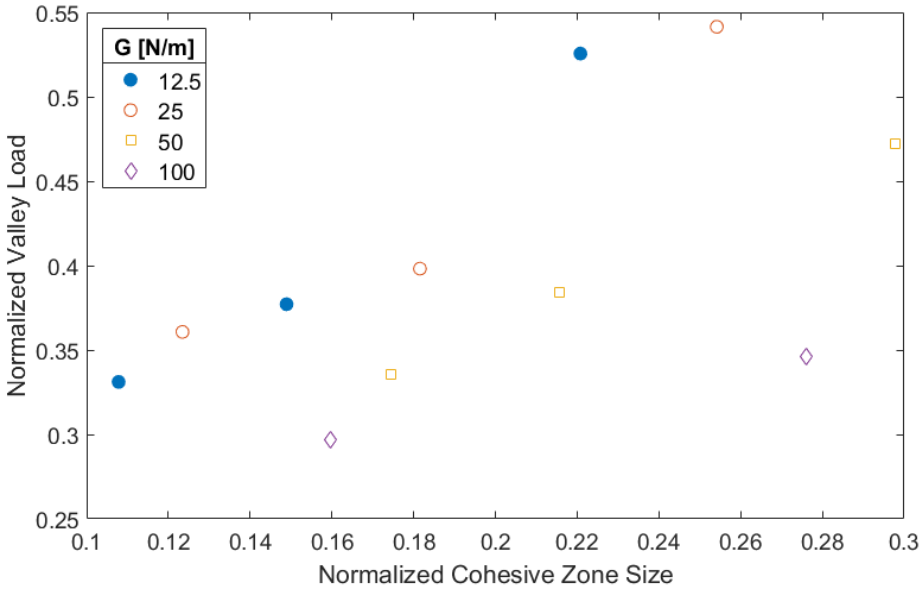

Figure 4.14: Normalized valley load versus normalized cohesive zone size.

corresponding the higher normalized peak forces.

The experiments and simulations show that in order to achieve the maximum peel force enhancement due to a stiffness heterogeneity, the cohesive zone of the adhesive must be much smaller than the characteristic length, $\lambda = \sqrt{\frac{D}{2G}}$, of the tape. Additionally, they show that the peel force enhancement at the step up in stiffness

is accompanied by a peel force reduction at the step down in stiffness. Peel front penetration into the heterogeneous region was observed in both the experiments and simulations, and later onset of penetration was generally related to higher peel force enhancement. Extrapolating this to the brittle case (cohesive zone size is zero), the highest normalized peak loads would occur with very little crack penetration into the heterogeneous region. The mechanism for toughening for heterogeneous laminate is additional energy input involved in changing the radius of curvature of the tape from one steady state value to another as the tape passes through the heterogeneous interface [8]. The influence of the peel front penetration (and subsequent involvement of more of the heterogeneity while changing the radius of curvature of the peeling tape), is a contributing factor to the smoothing process.

Chapter 5

SUMMARY AND FUTURE WORK

This thesis examined the mechanics of crack propagation through periodic heterogeneous media using experiments, finite element simulations, and theoretical analysis with the aim of developing a greater understanding of the role various mechanisms play in enhancing toughness. Chapter 2 presented the results from experiments investigating crack propagation in brick-like architectures. Renucleation in the brick-like architectures when the crack front passed from a region of no or low elastic modulus to a region of relatively high elastic modulus was identified as a toughening mechanism. Chapter 2 also presented theoretical considerations and experimental studies of a horizontally layered heterogeneous architecture. The trend observed in the experiments does not agree with the trend predicted by the theory, which needs additional study. Further analysis and experiments are needed to understand the role of layered architectures on fracture toughness.

Chapter 3 presents studies examining the relative contribution of elastic heterogeneity and renucleation to fracture toughness enhancement. Comparative experiments to isolate the additional enhancement due to renucleation are presented. Theoretical considerations that propose models for the fracture toughness due to elastic contrast and due to renucleation are discussed. The results of phase field numerical simulations and experiments are in good agreement with the proposed models. The effect of renucleation was observed to be more substantial than that of the elastic contrast alone. Additionally, the amount of enhancement was observed to depend on the width of the heterogeneous layers. The theoretical and computational analysis presented in this thesis assumed linear elasticity; however, there was limited inelasticity in the experiments. The simulations presented by Wang and Xia took cohesive zone size into account and showed that the amount of toughening depended on the size of the heterogeneity with respect to the size of the cohesive zone of the material [37]. Extension of the work presented in this thesis to elastic plastic materials would provide further insights in toughening behavior in heterogeneous materials and introduce crack-tip blunting as another mechanism of fracture toughening.

Chapter 4 investigates the effect of cohesive zone size and stiffness heterogeneity on adhesive strength (fracture toughness) in tape peeling experiments. Experimental

observations and finite element simulations are used to investigate the relationship between fracture toughness enhancement, cohesive zone size, and adhesive strength for crack propagation through periodic heterogeneous layered media. The experimental observations and simulations are in agreement that the enhancement in fracture toughness generally increases with decreasing cohesive zone size and adhesive strength. Additionally, experimental observations and simulations agree that the crack front penetrates into the stiffer heterogeneous region prior to the peak enhancement being reached. The experiments and simulations indicate that the cohesive zone works to smooth out the stiffness discontinuity and reduces its toughening effect. Further parametric studies of the effects of G, cohesive zone size, and penetration into the heterogeneous region on normalized peak force are necessary to develop a model relating these quantities. Additionally, experimental results showed that the amount of enhancement saturates at some thickness of the heterogeneity. Further studies investigating why this appears to be the case would be valuable in understanding the limits of using stiffness contrast to toughen composite tapes against peeling.

BIBLIOGRAPHY

[1] M. E. Launey and R. O. Ritchie. "On the Fracture Toughness of Advanced Materials". *Advanced Materials* 21.20 (2009), pp. 2103–2110. ISSN: 1521-4095. DOI: 10.1002/adma.200803322. URL: http://dx.doi.org/10.1002/adma.200803322.

[2] J. W. Hutchinson. "Mechanisms of Toughening in Ceramics". *Theoretical and applied mechanics* (1989), pp. 139–144.

[3] *ASTM Standard F2792-12a, Standard Terminology for Additive Manufacturing Technologies (Withdrawn 2015)*. 10.1520/F2792-12A. West Conshohocken, PA: ASTM International, 2012. URL: www.astm.org.

[4] "What Is Additive Manufacturing?" *Additive Manufacturing Research Group, Loughborough University* (2016). URL: http://www.lboro.ac.uk/research/amrg/about/the7categoriesofadditivemanufacturing/ (visited on 10/05/2016).

[5] R. Pearson. "Introduction to the Toughening of Polymers". *Toughening of Plastics*. ACS Symposium Series 759. American Chemical Society, 2000, pp. 1–12. ISBN: 0-8412-3657-7. DOI: 10.1021/bk-2000-0759.ch001. URL: http://dx.doi.org/10.1021/bk-2000-0759.ch001 (visited on 10/27/2016).

[6] B. Cotterell and J. Rice. "Slightly Curved or Kinked Cracks". *International Journal of Fracture* 16.2 (1980), pp. 155–169. ISSN: 1573-2673. DOI: 10.1007/bf00012619. URL: http://dx.doi.org/10.1007/BF00012619.

[7] R. Rivlin. "The Effective Work of Adhesion". *Collected Papers of R.S. Rivlin: Volume I and II*. Ed. by G. Barenblatt and D. Joseph. New York, NY: Springer New York, 1997, pp. 2611–2614. ISBN: 978-1-4612-2416-7. DOI: 10.1007/978-1-4612-2416-7_179. URL: http://dx.doi.org/10.1007/978-1-4612-2416-7_179.

[8] K. Kendall. "Control of Cracks by Interfaces in Composites". *Proceedings of the Royal Society of London. Series A, Mathematical and Physical Sciences* 341.1627 (1975), pp. 409–428. ISSN: 00804630.

[9] A. Ghatak. "Peeling off an Adhesive Layer with Spatially Varying Modulus". *Physical Review E* 81.2 (2010), p. 021603. URL: http://link.aps.org/doi/10.1103/PhysRevE.81.021603.

[10] M. Hossain, C.-J. Hsueh, B. Bourdin, and K. Bhattacharya. "Effective Toughness of Heterogeneous Media". *Journal of the Mechanics and Physics of Solids* 71 (2014), pp. 15–32.

[11] L. S. Dimas, G. H. Bratzel, I. Eylon, and M. J. Buehler. "Tough Composites Inspired by Mineralized Natural Materials: Computation, 3D Printing, and Testing". *Advanced Functional Materials* 23.36 (2013), pp. 4629–4638. ISSN: 1616-3028. DOI: 10.1002/adfm.201300215. URL: http://dx.doi.org/10.1002/adfm.201300215.

[12] L. S. Dimas and M. J. Buehler. "Modeling and Additive Manufacturing of Bio-Inspired Composites with Tunable Fracture Mechanical Properties". *Soft Matter* 10.25 (2014), pp. 4436–4442. ISSN: 1744-683X. DOI: 10.1039/C3SM52890A. URL: http://dx.doi.org/10.1039/C3SM52890A.

[13] L. S. Dimas, D. Veneziano, and M. J. Buehler. "Strength and Fracture Toughness of Heterogeneous Blocks with Joint Lognormal Modulus and Failure Strain". *Journal of the Mechanics and Physics of Solids* 92 (2016), pp. 72–86. ISSN: 0022-5096. DOI: 10.1016/j.jmps.2016.03.026. URL: http://www.sciencedirect.com/science/article/pii/S0022509615300764.

[14] *ASTM Standard D5045-99, Standard Test Methods for Plane-Strain Fracture Toughness and Strain Energy Release Rate of Plastic Materials*. 10.1520/D5045-99. West Conshohocken, PA: ASTM International, 1999. URL: www.astm.org.

[15] *ASTM Standard D6068-96, Standard Test Methods for Determining J-R Curves of Plastic Materials*. 10.1520/D6068-96. West Conshohocken, PA: ASTM International, 1996. URL: www,astm.org.

[16] D. Hull. *Fractography : Observing, Measuring, and Interpreting Fracture Surface Topography*. New York: Cambridge University Press, 1999. URL: https://search.library.wisc.edu/catalog/999883125702121.

[17] J. Mecholsky and S. Freiman. "Determination of Fracture Mechanics Parameters through Fractographic Analysis of Ceramics". *Fracture Mechanics Applied to Brittle Materials*. ASTM International, 1979.

[18] S. DiFrancesco. "Quantitative Fractography: A Comparative Study for Polymer Toughness Evaluation". University of Florida, 2006. 64 pp.

[19] J. Tracy, A. Waas, and S. Daly. "Experimental Assessment of Toughness in Ceramic Matrix Composites Using the J-Integral with Digital Image Correlation Part I: Methodology and Validation". *Journal of Materials Science* 50.13 (2015), pp. 4646–4658. ISSN: 1573-4803. DOI: 10.1007/s10853-015-9016-y. URL: http://dx.doi.org/10.1007/s10853-015-9016-y.

[20] J. Tracy, A. Waas, and S. Daly. "Experimental Assessment of Toughness in Ceramic Matrix Composites Using the J-Integral with Digital Image Correlation Part II: Application to Ceramic Matrix Composites". *Journal of Materials Science* 50.13 (2015), pp. 4659–4671. ISSN: 1573-4803. DOI: 10.1007/

s10853-015-9017-x. URL: http://dx.doi.org/10.1007/s10853-015-9017-x.

[21] A. A. Griffith. "VI. The Phenomena of Rupture and Flow in Solids". *Phil. Trans. R. Soc. Lond. A* 221.582-593 (1921), pp. 163–198. ISSN: 0264-3952.

[22] D. Broek. *Elementary Engineering Fracture Mechanics*. Springer Science & Business Media, 2012. ISBN: 94-009-4333-4.

[23] J. Rice. "A Path Independent Integral and the Approximate Analysis of Strain Concentration by Notches and Cracks". *Journal of Applied Mechanics* 35.2 (1968), pp. 379–386. ISSN: 0021-8936. DOI: 10.1115/1.3601206. URL: http://dx.doi.org/10.1115/1.3601206.

[24] A. F. Bower. *Applied Mechanics of Solids*. CRC press, 2009. ISBN: 1-4398-0248-3.

[25] C. E. Inglis. "Stresses in a Plate Due to the Presence of Cracks and Sharp Corners". *Transactions of the institute of naval architects* 55.219-241 (1913), pp. 193–198.

[26] M. Williams. "Stress Singularities Resulting from Various Boundary Conditions in Angular Corners of Plates in Extension". *Journal of applied mechanics* 19.4 (1952), pp. 526–528. ISSN: 0021-8936.

[27] M. Williams. "The Bending Stress Distribution at the Base of a Stationary Crack". *Journal of applied mechanics* 28.1 (1961), pp. 78–82. ISSN: 0021-8936.

[28] M. Ortiz. AE 102b Class Notes. California Insitute of Technology, 2015.

[29] C.-J. Hsueh, L. Avellar, B. Bourdin, G. Ravichandran, and K. Bhattacharya. "Stress Fluctuation, Crack Renucleation and Toughening in Layered Materials". *Journal of the Mechanics and Physics of Solids* (2018). DOI: 10.1016/j.jmps.2018.04.011.

[30] E. Tanné, T. Li, B. Bourdin, J.-J. Marigo, and C. Maurini. "Crack Nucleation in Variational Phase-Field Models of Brittle Fracture". *Journal of the Mechanics and Physics of Solids* 110 (2018), pp. 80–99. ISSN: 0022-5096. DOI: 10.1016/j.jmps.2017.09.006. URL: http://www.sciencedirect.com/science/article/pii/S0022509617306543.

[31] D. Dugdale. "Yielding of Steel Sheets Containing Slits". *Journal of the Mechanics and Physics of Solids* 8.2 (1960), pp. 100–104. ISSN: 0022-5096. DOI: 10.1016/0022-5096(60)90013-2. URL: http://www.sciencedirect.com/science/article/pii/0022509660900132.

[32] A. Zehnder. *Fracture Mechanics*. Lecture Notes in Applied and Computational Mechanics. Springer Netherlands, 2012. ISBN: 978-94-007-2594-2.

[33] G. Barenblatt. “The Mathematical Theory of Equilibrium Cracks in Brittle Fracture”. *Advances in Applied Mechanics*. Ed. by H. Dryden, T. von Kármán, G. Kuerti, F. van den Dungen, and L. Howarth. Vol. 7. Elsevier, 1962, pp. 55–129. ISBN: 0065-2156. DOI: 10.1016/S0065-2156(08)70121-2. URL: http://www.sciencedirect.com/science/article/pii/S0065215608701212.

[34] K. T. Faber and A. G. Evans. “Crack Deflection Processes—I. Theory”. *Acta Metallurgica* 31.4 (1983), pp. 565–576. ISSN: 0001-6160. DOI: 10.1016/0001-6160(83)90046-9. URL: http://www.sciencedirect.com/science/article/pii/0001616083900469.

[35] H. Ming-Yuan and J. Hutchinson. “Crack Deflection at an Interface between Dissimilar Elastic Materials”. *International Journal of Solids and Structures* 25.9 (1989), pp. 1053–1067. ISSN: 0020-7683. DOI: 10.1016/0020-7683(89)90021-8. URL: http://www.sciencedirect.com/science/article/pii/0020768389900218.

[36] A. Zak and M. Williams. “Crack Point Stress Singularities at a Bi-Material Interface”. *Journal of Applied Mechanics* 30.1 (1963), pp. 142–143. ISSN: 0021-8936. DOI: 10.1115/1.3630064. URL: http://dx.doi.org/10.1115/1.3630064.

[37] N. Wang and S. Xia. “Cohesive Fracture of Elastically Heterogeneous Materials: An Integrative Modeling and Experimental Study”. *Journal of the Mechanics and Physics of Solids* 98 (2017), pp. 87–105. ISSN: 0022-5096. DOI: 10.1016/j.jmps.2016.09.004. URL: http://www.sciencedirect.com/science/article/pii/S0022509616303313.

[38] K. Kendall. “Thin-Film Peeling-the Elastic Term”. *Journal of Physics D: Applied Physics* 8.13 (1975), p. 1449. ISSN: 0022-3727.

[39] S. Xia, L. Ponson, G. Ravichandran, and K. Bhattacharya. “Adhesion of Heterogeneous Thin Films—I: Elastic Heterogeneity”. *Journal of the Mechanics and Physics of Solids* 61.3 (2013), pp. 838–851. ISSN: 0022-5096. DOI: https://doi.org/10.1016/j.jmps.2012.10.014. URL: http://www.sciencedirect.com/science/article/pii/S0022509612002359.

[40] L. Bass, N. A. Meisel, and C. B. Williams. “Exploring Variability of Orientation and Aging Effects in Material Properties of Multi-Material Jetting Parts”. *Rapid Prototyping Journal* 22.5 (2016), pp. 826–834. ISSN: 1355-2546. DOI: 10.1108/RPJ-11-2015-0169. URL: https://doi.org/10.1108/RPJ-11-2015-0169 (visited on 04/29/2018).

[41] J. Mueller, K. Shea, and C. Daraio. “Mechanical Properties of Parts Fabricated with Inkjet 3D Printing through Efficient Experimental Design”. *Materials & Design* 86 (2015), pp. 902–912. ISSN: 0264-1275. DOI: 10.1016/j.matdes.2015.07.129. URL: http://www.sciencedirect.com/science/article/pii/S0264127515301994.

[42] G. Gu, I. Su, S. Sharma, J. Voros, Z. Qin, and M. Buehler. "Three-Dimensional-Printing of Bio-Inspired Composites". *Journal of Biomechanical Engineering* 138.2 (2016), ISSN: 0148-0731. DOI: 10.1115/1.4032423. URL: http://dx.doi.org/10.1115/1.4032423.

[43] G. X. Gu, F. Libonati, S. D. Wettermark, and M. J. Buehler. "Printing Nature: Unraveling the Role of Nacre's Mineral Bridges". *Structure-Property Relationships in Biological and Bioinspired Materials* 76 (2017), pp. 135–144. ISSN: 1751-6161. DOI: 10.1016/j.jmbbm.2017.05.007. URL: http://www.sciencedirect.com/science/article/pii/S1751616117301959.

[44] G. X. Gu, L. Dimas, Z. Qin, and M. J. Buehler. "Optimization of Composite Fracture Properties: Method, Validation, and Applications". *Journal of Applied Mechanics* 83.7 (2016), ISSN: 0021-8936. DOI: 10.1115/1.4033381. URL: http://dx.doi.org/10.1115/1.4033381.

[45] G. X. Gu, S. Wettermark, and M. J. Buehler. "Algorithm-Driven Design of Fracture Resistant Composite Materials Realized through Additive Manufacturing". *Additive Manufacturing* 17 (2017), pp. 47–54. ISSN: 2214-8604. DOI: 10.1016/j.addma.2017.07.002. URL: http://www.sciencedirect.com/science/article/pii/S2214860417300052.

[46] G. X. Gu, C.-T. Chen, and M. J. Buehler. "De Novo Composite Design Based on Machine Learning Algorithm". *Extreme Mechanics Letters* 18 (2018), pp. 19–28. ISSN: 2352-4316. DOI: 10.1016/j.eml.2017.10.001. URL: http://www.sciencedirect.com/science/article/pii/S2352431617301256.

[47] *Object350 and Object500 Connex3 System Specifications*. Stratasys, 2016. URL: http://global72.stratasys.com/~/media/Main/Files/Machine_Spec_Sheets/PSS_PJ_Connex3.ashx.

[48] N. Brodnik. "Stereolithography with Preceramic Polymers". Aug. 16, 2017.

[49] O. Chiantore, L. Trossarelli, and M. Lazzari. "Photooxidative Degradation of Acrylic and Methacrylic Polymers". *Polymer* 41.5 (2000), pp. 1657–1668. ISSN: 0032-3861.

[50] *ASTM D638-00, Standard Test Method for Tensile Properties of Plastics*. 10.1520/D0638-00. West Conshohocken, PA: ASTM International, 2002. URL: www.astm.org.

[51] M. Sutton, J. Orteu, and H. Schreier. *Image Correlation for Shape, Motion and Deformation Measurements: Basic Concepts, Theory and Applications*. Springer Science & Business Media, 2009. ISBN: 0-387-78747-X.

[52] E. Jones. "Improved Digital Image Correlation" (2013). URL: http://www.mathworks.com/matlabcentral/fileexchange/43073-improved-digital-image-correlation--dic-.

[53] J. Blaber, B. Adair, and A. Antoniou. "Ncorr: Open-Source 2D Digital Image Correlation Matlab Software". *Experimental Mechanics* 55.6 (2015), pp. 1105–1122. ISSN: 1741-2765. DOI: 10.1007/s11340-015-0009-1. URL: https://doi.org/10.1007/s11340-015-0009-1.

[54] "NEW Objet Materials: The Power behind Your 3D Printer" (2011). URL: https://www.prototech.com/wp-content/uploads/2012/06/Objet-Additional-Materials-Data-Sheet.pdf (visited on 03/21/2018).

[55] "Material Data Sheets: Digital Materials (General)" (). URL: www.growit3d.com/spec-sheets/ (visited on 03/30/2016).

[56] J. Hutchinson. *A Course on Nonlinear Fracture Mechanics*. Department of Solid Mechanics, Techn.University of Denmark, 1980. URL: https://books.google.com/books?id=UXG5nQEACAAJ.

[57] L. Zorzetto and D. Ruffoni. "Re-Entrant Inclusions in Cellular Solids: From Defects to Reinforcements". *Composite Structures* 176 (2017), pp. 195–204. DOI: 10.1016/j.compstruct.2017.05.039.

[58] C.-J. Hsueh and K. Bhattacharya. "Homogenization and Path Independence of the J-Integral in Heterogeneous Materials". *Journal of Applied Mechanics* 83.10 (2016), ISSN: 0021-8936. DOI: 10.1115/1.4034294. URL: http://dx.doi.org/10.1115/1.4034294.

[59] L. Zhang, W. Dong, D. Zhang, and G. Shi. "Two-Stage Image Denoising by Principal Component Analysis with Local Pixel Grouping". *Pattern Recognition* 43.4 (2010), pp. 1531–1549. ISSN: 0031-3203. DOI: 10.1016/j.patcog.2009.09.023. URL: http://www.sciencedirect.com/science/article/pii/S0031320309003677.

[60] S. N. Grama and S. J. Subramanian. "Computation of Full-Field Strains Using Principal Component Analysis". *Experimental Mechanics* 54.6 (2014), pp. 913–933. ISSN: 1741-2765. DOI: 10.1007/s11340-013-9800-z. URL: http://dx.doi.org/10.1007/s11340-013-9800-z.

[61] A. Bower and M. Ortiz. "A Three-Dimensional Analysis of Crack Trapping and Bridging by Tough Particles". *Journal of the Mechanics and Physics of Solids* 39.6 (Jan. 1, 1991), pp. 815–858. ISSN: 0022-5096. DOI: 10.1016/0022-5096(91)90026-K. URL: http://www.sciencedirect.com/science/article/pii/002250969190026K.

[62] A. Argon, R. Cohen, and T. Mower. "Mechanisms of Toughening Brittle Polymers". *Materials Science and Engineering: A* 176.1 (1994), pp. 79–90. ISSN: 0921-5093. DOI: 10.1016/0921-5093(94)90961-X. URL: http://www.sciencedirect.com/science/article/pii/092150939490961X.

[63] C.-J. Hsueh. "Effective Toughness of Heterogneous Materials". Pasadena: California Institute of Technology, 2017. 124 pp.

[64] G. X. Gu, M. Takaffoli, and M. J. Buehler. "Hierarchically Enhanced Impact Resistance of Bioinspired Composites". *Advanced Materials* 29.28 (2017), p. 1700060. ISSN: 0935-9648. DOI: 10.1002/adma.201700060. URL: https://doi.org/10.1002/adma.201700060 (visited on 04/27/2018).

[65] L. Plangsangmas, J. Mecholsky, and A. Brennan. "Determination of Fracture Toughness of Epoxy Using Fractography". *Journal of Applied Polymer Science* 72.2 (1999), pp. 257–268. ISSN: 0021-8995, 1097-4628. DOI: 10.1002/(SICI)1097-4628(19990411)72:2<257::AID-APP11>3.0.CO;2-M. URL: http://doi.wiley.com/10.1002/%28SICI%291097-4628%2819990411%2972%3A2%3C257%3A%3AAID-APP11%3E3.0.CO%3B2-M (visited on 02/28/2018).

[66] J. W. Johnson and D. G. Holloway. "On the Shape and Size of the Fracture Zones on Glass Fracture Surfaces". *The Philosophical Magazine: A Journal of Theoretical Experimental and Applied Physics* 14.130 (1966), pp. 731–743. DOI: 10.1080/14786436608211968. eprint: https://doi.org/10.1080/14786436608211968. URL: https://doi.org/10.1080/14786436608211968.

[67] G. R. Irwin. "Crack-Extension Force for a Part-Through Crack in a Plate". *Journal of Applied Mechanics* 29.4 (1962), pp. 651–654. ISSN: 0021-8936. DOI: 10.1115/1.3640649. URL: http://dx.doi.org/10.1115/1.3640649.

[68] W. F. Brown and J. E. Srawley. *Plane Strain Crack Toughness Testing of High-Strength Metallic Materials*. Vol. 410. 1967.

[69] G. Francfort and J.-J. Marigo. "Revisiting Brittle Fracture as an Energy Minimization Problem". *Journal of the Mechanics and Physics of Solids* 46.8 (1998), pp. 1319–1342. ISSN: 0022-5096. DOI: 10.1016/S0022-5096(98)00034-9. URL: http://www.sciencedirect.com/science/article/pii/S0022509698000349.

[70] B. Bourdin, G. Francfort, and J.-J. Marigo. "Numerical Experiments in Revisited Brittle Fracture". *Journal of the Mechanics and Physics of Solids* 48.4 (2000), pp. 797–826. ISSN: 0022-5096. DOI: 10.1016/S0022-5096(99)00028-9. URL: http://www.sciencedirect.com/science/article/pii/S0022509699000289.

[71] B. Bourdin. "Numerical Implementation of the Variational Formulation for Quasi-Static Brittle Fracture". *Interfaces and free boundaries* 9.3 (2007), pp. 411–430. ISSN: 1463-9963.

[72] B. Bourdin, G. A. Francfort, and J.-J. Marigo. "The Variational Approach to Fracture". *Journal of elasticity* 91.1-3 (2008), pp. 5–148. ISSN: 0374-3535.

[73] L. Ambrosio and V. M. Tortorelli. "Approximation of Functional Depending on Jumps by Elliptic Functional via T-convergence". *Communications on Pure and Applied Mathematics* 43.8 (2006), pp. 999–1036. ISSN: 0010-3640.

DOI: 10.1002/cpa.3160430805. URL: https://doi.org/10.1002/cpa.3160430805 (visited on 04/30/2018).

[74] B. Bourdin, J.-J. Marigo, C. Maurini, and P. Sicsic. "Morphogenesis and Propagation of Complex Cracks Induced by Thermal Shocks". *Physical review letters* 112.1 (2014), p. 014301.

[75] E. Tanné, T. Li, B. Bourdin, J.-J. Marigo, and C. Maurini. "Crack Nucleation in Variational Phase-Field Models of Brittle Fracture". *Journal of the Mechanics and Physics of Solids* 110 (2018), pp. 80–99. ISSN: 0022-5096. DOI: 10.1016/j.jmps.2017.09.006. URL: http://www.sciencedirect.com/science/article/pii/S0022509617306543.

[76] W. LaMorte. "Mann Whitney U Test (Wilcoxon Rank Sum Test)" (2017). URL: http://sphweb.bumc.bu.edu/otlt/mph-modules/bs/bs704_nonparametric/BS704_Nonparametric4.html (visited on 04/12/2017).

[77] D. Leguillon and E. Martin. *Crack Nucleation at Stress Concentration Points in Composite Materials - Application to the Crack Deflection by an Interface*. 2013. DOI: 10.1142/9781848167858_0010.

[78] S. Xia, L. Ponson, G. Ravichandran, and K. Bhattacharya. "Toughening and Asymmetry in Peeling of Heterogeneous Adhesives". *Physical Review Letters* 108.19 (2012). URL: http://link.aps.org/doi/10.1103/PhysRevLett.108.196101.

[79] C. Kovalchick. "Mechanics of Peeling: Cohesive Zone Law and Stability". California Institute of Technology, 2011. URL: http://resolver.caltech.edu/CaltechTHESIS:05262011-172059575.

[80] "3M 142 Shipping Tape with Dispenser" (). URL: https://www.uline.com/Product/Detail/S-10173/3M-Packaging-Tapes/3M-142-Shipping-Tape-with-Dispenser-2-x-222-yds-Clear?pricode=WB1868&gadtype=pla&id=S-10173&gclid=EAIaIQobChMIiPLX-Kuu2gIVDBBpCh1tJw19EAYYASABEgKHmPD_BwE&gclsrc=aw.ds (visited on 04/09/2018).

[81] "3M 810 Scotch Tape" (). URL: https://www.uline.com/Product/Detail/S-10223/3M-Strapping-Tape/3M-810-Scotch-Tape-1-2-x-36-yds (visited on 04/09/2018).

[82] T. Diehl. "Modeling Surface-Bonded Structures with ABAQUS Cohesive Elements: Beam-Type Solutions". ABAQUS User's Conference. 2005.

[83] T. Diehl. "Using ABAQUS Cohesive Elements to Model Peeling of an Epoxy-Bonded Aluminum Strip: A Benchmark Study for Inelastic Peel Arms". DuPont Engineering Technology, Abaqus Users Conference. 2006.